Universiteit
Leiden
The Netherlands

From adsorptation to dissipation: insights from computer simulations of solid H2O and CO

Ferrari, B.C.

Citation
Ferrari, B. C. (2026, June 10). *From adsorptation to dissipation: insights from computer simulations of solid H2O and CO*. Retrieved from https://hdl.handle.net/1887/4304940

Version:	Publisher's Version
License:	Licence agreement concerning inclusion of doctoral thesis in the Institutional Repository of the University of Leiden
Downloaded from:	https://hdl.handle.net/1887/4304940

Note: To cite this publication please use the final published version (if applicable).

From Adsorption to Dissipation: Insights from Computer Simulations of Solid H_2O and CO

Proefschrift

ter verkrijging van
de graad van doctor aan de Universiteit Leiden,
op gezag van rector magnificus prof.dr. S. de Rijcke,
volgens besluit van het college voor promoties
te verdedigen op woensdag 10 juni 2026
klokke 10:00 uur

door

Brian Carmona Ferrari

geboren te Orlando, Florida, Verenigde Staten
in 1996

Promotor: Dr. J. Meyer
Co-promotor: Prof. em. dr. M.C. van Hemert

Promotiecommissie

Prof. dr. M. Ubbink
Dr. F. Buda
Prof. dr. S. Viti
Prof. dr. H. Jónsson (University of Iceland)
Prof. dr. H.M. Cuppen (Radboud Universiteit)

Copyright © *2026 Brian Carmona Ferrari.*

Cover art: *Surfaces and Depths (top half).* Designed by Katie Slavicinska in Adobe Photoshop. Inspired by the collaborative artworks of Stephen Muldoon and Robert Wyland. See Katie Slavicinska's thesis for bottom half.

Cover description: Mountains and valleys symbolize energy peaks and troughs on solid surfaces. Figures climbing rock walls symbolize adsorbed surface species. Pebbles fall from the rock walls into the water below to create ripples, symbolizing energy dissipation. Water molecules are referenced via the sea in the cove; CO molecules are referenced via the *CO-conuts* in the palm tree.

Contents

1 Introduction **1**

1.1 Computer Simulations . . . 2
1.2 Adsorption . . . 4
1.3 Vibrational Energy Relaxation . . . 5
1.4 Aims and Scope . . . 7
1.5 Main Results . . . 8
1.6 Outlook . . . 9
1.A Bibliography . . . 10

2 Methods **19**

2.1 Force Fields . . . 19
2.1.1 General Considerations . . . 19
2.1.2 Force Fields for H_2O . . . 22
2.1.3 Force Fields for CO . . . 26
2.2 Geometry Optimization . . . 29
2.3 Vibrational Analysis . . . 30
2.3.1 Harmonic Approximation . . . 30
2.3.2 Velocity Autocorrelation Function . . . 33
2.4 Molecular Dynamics . . . 36
2.4.1 Microcanonical Ensemble . . . 38
2.4.2 Canonical Ensemble . . . 39
2.A Bibliography . . . 40

3 YetAnotherSimulationSuite.jl: An Atomic Simulation suite in Julia **45**

3.1 Features . . . 46
3.2 Installation . . . 46
3.3 Benchmarks . . . 47
3.3.1 Geometry Optimization . . . 47
3.3.2 Harmonic Frequencies . . . 47
3.3.3 Molecular Dynamics . . . 48
3.4 Memory Considerations . . . 48
3.4.1 Geometry Optimization . . . 49
3.4.2 Harmonic Frequency Calculation . . . 49

3.4.3 Molecular Dynamics Simulation 49
3.5 Examples 49
3.A Bibliography 51

4 Abundance of Exceptionally Strong Binding Sites for H_2O Adsorption on the Ice Ih(0001) Surface 53
4.1 Abstract 54
4.2 Introduction 54
4.3 Methods 56
4.4 Results and Discussion 58
4.5 Conclusion 63
4.A Appendix 64
4.A.1 Optimized Lattice Vectors and Cohesive Energy 64
4.A.2 Order Paremeter 2.0 Surfaces 64
4.A.3 Binding Energy Correlations 64
4.A.4 Bond Angle Analysis 65
4.B Bibliography 70

5 Floating in Space: How to Treat the Weak Interaction between CO Molecules in Interstellar Ices 75
5.1 Abstract 76
5.2 Introduction 76
5.3 Computational Details 78
5.3.1 Force Field 78
5.3.2 Density Functional Theory 80
5.4 Results and Discussion 82
5.4.1 DFT Benchmark 82
5.4.2 Amorphous CO 83
5.4.3 Crystalline CO 90
5.5 Astrophysical Implications 92
5.6 Conclusion 93
5.7 Data Availability Statement 94
5.A Appendix 94
5.A.1 Pair Interaction Validation 94
5.A.2 Geometry Optimization Threshold 94
5.A.3 Total Interaction Energy 96
5.A.4 DBSCAN 98

5.A.5 Dimer Geometries 98
5.B Bibliography 101

6 Vibrational Energy Relaxation in Solid Carbon Monoxide 109
6.1 Abstract 110
6.2 Introduction 110
6.3 Methods 113
6.4 Structural and Vibrational Properties 116
6.5 Analyzing Vibrational Energy Relaxation with Classical Dynamics . . 120
6.5.1 Trajectory Ensembles 120
6.5.2 Frequency Shift 122
6.5.3 Frequency-Gap Dependent Decay Rate 124
6.6 Results and Discussion 125
6.6.1 Amorphous Cluster 125
6.6.2 Crystalline Cluster 127
6.6.3 Analysis of Energy Redistribution 128
6.6.4 Non-Resonant Energy Transfer 130
6.6.5 Resonant Energy Transfer 132
6.7 Summary and Outlook 133
6.8 Data Availability Statement 135
6.A Appendix 135
6.A.1 Size Convergence Tests 135
6.A.2 Geometric and Vibrational Properties for the PIP–NN Potential 136
6.A.3 Decomposition of Phonon DOS 137
6.A.4 Trajectory Ensemble for Crystalline Clusters 138
6.A.5 Decomposition of Bi-Exponential Fits for Non-Resonant Energy Transfer 138
6.B Bibliography 145

Summary 151

Samenvatting 155

Publications 159

Curriculum vitae 161

Acknowledgments 163

Data Availability **165**

Chapter 1

Introduction

Scientific research often comes in two forms, experimental and theoretical, where the former consists of laboratory measurements and the latter comes from mathematical formulations. These two disciplines maintain a symbiotic relationship, where experimental work is often used to verify approximate theoretical models and theoretical works are able to fill in knowledge gaps due to technical limitations in experiments. The work in this thesis focuses primarily on computer simulations based on approximations for atomic-scale interactions, with an emphasis on properties or processes that experiments are unable to observe.

Atomic-scale interactions are described using either first-principles quantum chemistry techniques or empirical interatomic potentials. These atomic-scale interactions are important because they govern the macroscopic properties of materials. Understanding these atomic-scale interactions helps us understand large-scale phenomena such as catalysis, crystal growth, and phase transitions. In particular, the processes of adsorption and vibrational energy relaxation (VER) are intrinsically related to catalysis. Adsorption is the first step in a catalytic process, and VER is often important for determining the next elementary reaction step in a catalytic cycle. Thus, understanding the atomic-scale interactions that govern adsorption and VER at the atomic-scale is crucial to understanding catalysis. In this thesis I study adsorption and VER for two simple yet interesting molecules, carbon monoxide (CO) and water (H_2O).

Carbon Monoxide

CO is one of the most abundant molecules in the interstellar medium (ISM).[1–3] In the ISM CO is known to form in the gas phase, where it then condenses onto icy grains.[4] On these icy grains CO is thought to be the seed for the formation of various other molecules, such as CO_2[5], CH_3OH[6,7], and logically all other molecules formed by reactions with CO_2 or CH_3OH. Furthermore, due to the CO being an extremely volatile species, sublimating at 25 K, it is the perfect measure of the degree of thermal processing of icy grains. To physical chemists, CO is of high interest due to its vibrational energy pooling (VEP) properties, most notably when adsorbed on a sodium

chloride crystal.[8–10] CO is the perfect candidate for studying vibrational energy transfer. Given it only possesses a single molecular vibrational mode, which has a large energy gap from its lattice modes, CO can easily be used to study how vibrational energy is transferred. Isotopic studies can be used to quantify the effect of the energy gap on the efficiency of energy transfer.

Water

Water is one of the most extensively studied molecules in existence. It has earned this title not only by being vital to life but also due to its unique properties (high heat capacity, inverse thermal expansion, etc.). As a liquid water serves as a universal solvent for biochemical processes, whereas, in solid form it serves as a catalyst for reactions in the ISM. In nearly all domains of chemistry water is an essential and highly studied molecule. Despite this, to this day there still remains numerous unexplained phenomena revolving around water, one of which is investigated in Chapter 4.

1.1 Computer Simulations

Molecular simulations rely on statistical mechanics and numerical methods to simulate molecular systems at various length and time scales. The work presented in this thesis focuses on atomic simulations using interatomic potentials, as such, here only this form of computer simulation is briefly introduced. Furthermore, there is a focus on molecular dynamics simulations and atomic geometry optimizations, which are the primary techniques used in this thesis.

Software

To date there exist numerous software packages that can be used to carry out molecular dynamics simulations. Certain packages, for example LAMMPS[11] and GROMACS[12–15], prioritize speed and performance by enabling simulations to be highly parallelized. In order to achieve these goals they often sacrifice flexibility and ease-of-use, not to mention the often feared compilation difficulties associated with these particular packages. As a result, users are limited to constructing their potentials with the pre-defined potential functions and using pre-defined auxiliary tools (thermostats, integrators, etc.). For potential development, users can port their own potential codes but this comes with the loss of any speed or performance boosts afforded by the simlation suite. Alternatively, users can turn to JIT compiled packages, for example

JaxMD[16] and Molly.jl[17], where flexibility and ease-of-use are not sacrificed for speed and performance. Unfortunately, these JIT compiled packages are fairly new and often do not offer the user or users the full range of features offered by other packages.

As a result, users that want a more flexible atomic simulation suite tend to turn to ASE[18]. However, ASE does not prioritize speed and performance, however, it provides interfaces to nearly all other software packages. This gives users a simple and flexible interface to perfroamnce focused packages, which cemented it as the defacto package for interacting with atomistic simulations. Modern programming languages, like Julia[19], offer the ability to develop software packages that can be as performant as LAMMPS or GROMACS while also being as flexible and intuitive as ASE. Allowing users to only depedend on a single package for all atomic simulation needs. However, building all the features and functionality available in ASE takes time and an active community of open-source developers.

Potentials

The interatomic potential describes the potential energy surface of the system being simulated. Hence, the accuracy of the simulations is directly tied to the sophistication and completeness of the empirical potential being used. For decades theoretical chemists have strived to develop realistic and transferrable water potentials. A potential is realistic when the simulations it is used for reproduce physical observations, while a transferrable potential is one that can reproduce observations not used in the development of the potential. For example, a potential developed using ice observations would be realistic if it reproduced observations for ice and transferrable if it reproduced observations for water.

The majority of the work on developing interatomic potentials has focused on water. Initial models were simple point charge (SPC) models, like SPC[20], SPC/E[21], and SPC-F[22]. These potentials represented the atoms as point charges with a nuetral molecular charge. Molecular bonds were often represented as harmonic potentials and intermolecular forces were O−O van der Waals forces plus electrostatic interactions from the point charges. At the time these models offered an incredibly powerful way to study water at the atomic scale. Shortly after, more sophisticated models began to be constructed; *ie.* TIP4P[23], TIP4P/2005[24], TIP4P/Ice[25], and TIP4P/2005f[26]. In an attempt to more accurately represent the electrostatic distribution around a water molecule, they add a fourth dummy atom along the bisector of the HOH angle. The total charge previously held by hydrogen atoms is now placed on the dummy atom, and the hydrogens are neutral. Furthermore, molecular bonds began to be

represented by Morse potentials. This model was widely adopted by computational chemists and until this day is widely used in research studies due to its balance of accuracy and computational cost. However, these models lack transferrability and are often only able to accurately reproduce water under certain conditions. Attempting to overcome these limitations, models that accounted for many-body effects were constructed. Some examples of polarizable models are, TTMx-F[27–32], POLI2VS[33], AMOEBA[34–39], SCME/f[40–43], and MB-pol[44–47]. These water models have become the gold standard for atomistic simulations of water, in particular due to their high accuracy and transferrability.

1.2 Adsorption

Adsorption is the process by which molecules or atoms adhere to a surface, over time forming a thin film or layer. Figure 1.1 shows a simple schematic of the adsorption process, along with a schematic of the inverse process (desorption). Adsorption is a crucial step in many chemical and physical phenomena, including catalysis, atmospheric chemistry, and materials science. Adsorption can occur through various mechanisms, such as physisorption and chemisorption. The former is driven by weaker intermolecular forces, such as van der Waals or electrostatic interactions, while the latter involves the formation of chemical bonds between the adsorbate and the surface. Understanding the mechanisms and factors that influence adsorption is essential for controlling and optimizing various chemical and physical processes.

Astronomical modellers use reaction networks to model ice and gas molecular abundances in various interstellar environments and compare their results with observations.[48] These comparisons are used to validate the assumptions of chemical reactions that are occurring in the ISM. A vital part of these models is binding energies, the smallest amount of energy required to remove a molecule from a system of molecules (e.g., to desorb a molecule). The binding energies determine which type of molecules will be in the solid phase versus the gas phase in the ISM (where different possible reactions apply in each phase).[49] Experiments offer the most realistic value for the binding energy; however, they can only measure the statistical average binding energy. Recent models have shown this single value is insufficient, and binding energy distributions produce more realistic models.[50] Simulations can fill in the gaps by providing a complete distribution of the binding energies.[51,52]

Furthermore, in certain unique cases, binding energies cannot be measured experimentally due to physical limitations. For example, in the case of a molecule adsorbing

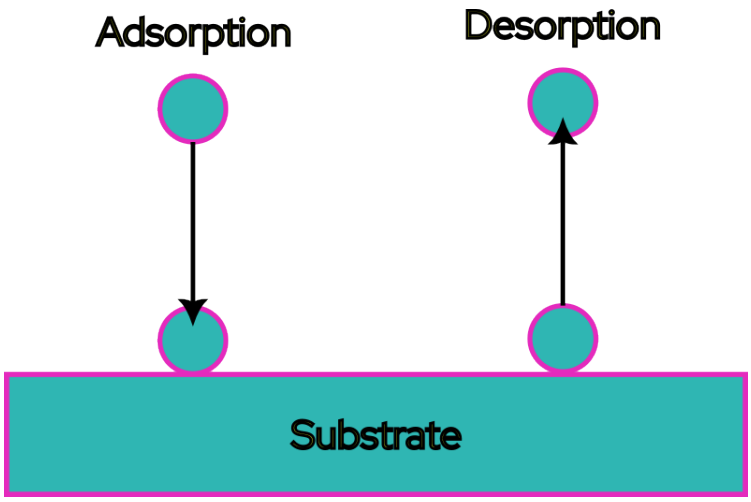

Figure 1.1: A simple representation of adsorption and desorption.

on a solid of the same species (e.g., H_2O on H_2O), any binding energy larger than the solid's cohesive energy will be impossible to measure because the temperature needed to desorb the admolecule (and thus measure the binding energy) is larger than the temperature needed to sublimate the surface to which the molecule is adsorbed. Again, here simulations are not limited by these constraints and can help shine light on the reality of the binding sites in question.

1.3 Vibrational Energy Relaxation

Figure 1.2 shows a simple schematic of the different types of normal modes for a gas-phase water molecule. Vibrational energy relaxation (VER) is the process by which a vibrationally excited molecule returns to its ground state by transferring its excess energy to its surroundings. This process is crucial in many chemical and physical phenomena, including energy transfer in biological systems[53], catalysis[54], and in the selectivity of chemical reactions[55]. VER can occur through various mechanisms, including vibrational-vibrational (V-V) energy transfer, vibrational-translational (V-T) energy transfer, vibrational-rotational (V-R) energy transfer, and vibrational-electronic (V-E) energy transfer. The efficiency of VER depends on several factors, including the nature of the molecule, the surrounding environment, and the energy gap between the excited and ground states. Understanding the mechanisms and factors that influence VER is essential for controlling and optimizing various chemical and physical

processes.

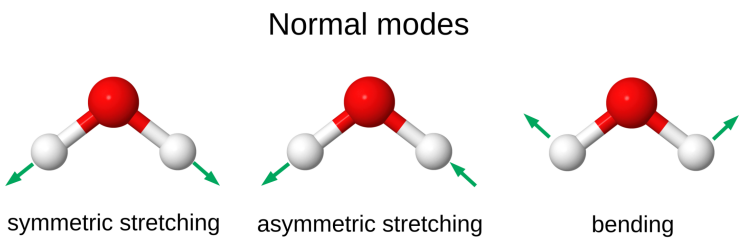

Figure 1.2: A simple explanation of the different types of normal modes for a water molecule.

In molecular simulations there is a number of ways to study VER. The most common way is to use non-equilibrium molecular dynamics (NEMD) simulations, where the molecule of interest is excited to a higher vibrational state, and the subsequent relaxation process is monitored over time. This approach can provide insights into the mechanisms, timescales, and relaxation pathways of the VER process. Frequently the results of these simulations are combined with experimental results, such as time-resolved pump-probe spectroscopy [56], to uncover the complex mechanisms involved in the VER process. However, NEMD studies are computationally challenging due to requirements on system size, integration time, and the need to average over an ensemble of simulation trajectories. In order to perform these studies, especially for long-lived vibrational modes, highly performant molecular dynamics software is necessary.

A general trend for VER lifetimes is that they decrease with increasing temperature, a result of an increased coupling between the excited molecule and the surrounding bath modes. This increased coupling is due to the fact that higher temperatures lead to higher occupancy of vibrational modes within the bath, effectively reducing the energy gap. However, for water the inverse trend was observed, where the VER lifetime increased with increasing temperature. [57] The same study also reported that for ice, solid water, the VER lifetime was independent of temperature. The authors credit this to the strong anharmonicity of the hydrogen-bond mode in ice, which produces a strong coupling between the OH-stretch and hydrogen-bond modes. This results in the VER lifetime being weakly dependent on the thermal occupation of the vibrational modes of the surrounding molecules. For water, they were unable to determine the exact mechanism for the anomalous temperature dependence of the VER lifetime.

Deàk *et al.* [58] performed NEMD simulations of the VER of HDO in D_2O, where they found that the OH-stretch decay generates substantial excitation of the bending

modes in D_2O. Following on these findings, Lock and Bakker [59] revealed that the anomalous temperature dependence in water was due to a decrease in the overlap between the OH-stretch mode and the overtone of the H-O-H bending mode.

1.4 Aims and Scope

The most important questions addressed by this thesis are:

1. How can atomistic simulations be improved so they are both easy to use and highly performant?
2. What are the most important physicochemical properties involved in the adsorption of H_2O on the ice Ih (0001) surface?
3. What are the most important physicochemical properties involved in the adsorption of CO on solid CO?
4. What processes are involved in the vibrational relaxation of a CO molecule in solid CO?

Chapter 2: This chapter summarizes the theory and methodology used for the research in this thesis. It starts by briefly covering the force fields used in the subsequent chapters. Then, it summarizes commonly used methods used to calculate vibrational modes and density of states of molecular systems.
Chapter 3: This chapter gives an overview of the features implemented in a Julia-based atomistic simulation suite developed during this PhD. An emphasis is placed on the flexibility and ease-of-use of the simulation suite, with examples given to highlight how simple usage is. At the same time, the resulting simulations achieve remarkable computational efficiency.
Chapter 4: The physicochemical properties that govern the adsorption of H_2O on the ice Ih (0001) surface are broken down and analyzed.
Chaper 5: The binding energy of CO on amorphous and crystalline CO is studied. The most important contributions to the binding energy are investigated, and the importance of long-range interactions is analyzed. Furthermore, a benchmark of DFT functionals is carried out, where the best performing functional is presented.
Chapter 6: Through NEMD simulations the VER process for CO in amorphous and crystalline CO is studied. A novel method of analyzing the MD trajectories is utilized, and the importance of the energy gap is scrutinized.

1.5 Main Results

Chapter 3: An atomic simulation suite was developed using the Julia programming language, with a test suite and online documentation. This software package is easy to install and quick to learn, making it incredibly attractive to the scientific community. When compared to the popular Python-based alternative (ASE), this new package provides up to a 6x speedup. This speedup enables users to perform previously infeasible simulations.

Chapter 4: A plethora of strong binding sites (sites with binding energy larger than the cohesive energy) is found on ice Ih (0001) surfaces across various degrees of proton ordering. This challenges the previously accepted idea that highly ordered surfaces would not produce strong binding sites. Furthermore, a comprehensive analysis focusing on understanding what physicochemical properties are most important for binding is done. This analysis allows for the creation of a site descriptor that can be used to predict which sites will have stronger binding energies. This novel descriptor builds off of previous global surface descriptors but addresses the issue of local influence on the binding.

Chapter 5: CO binding is dominated by dispersion, with negligible contributions from many-body effects in solid CO. The distribution of binding energies for CO on amorphous CO is broad (200 – 1600 K) and depends on the size of the cluster. The dependence on the size of the cluster reveals that long-range interactions are relevant to the adsorption of CO on amorphous CO. Zero point energy corrections within the harmonic approximation lowers the average binding energy by 20-30%. CO binding on crystalline α-CO has a more narrow distribution (650 – 800 K) and is orientation dependent. The median values of the binding energy distribution for amorphous and crystalline CO are very similar, corroborating previous studies which assumed them to be equal. Lastly, a benchmark revealed that the ωB97M-V functional performs the best when treating the CO–CO dimer interaction energy.

Chapter 6: A novel analysis technique for studying the frequency-gap dependence of the decay time constant was developed. Anharmonic coupling between an excited CO molecule and a different CO isotope results in vibrational energy relaxation that is faster when the excited molecule has a lower frequency than the accepting molecule. On the other hand, in crystalline clusters the frequency-gap dependence exhibited no significant trends other than being most efficient at gaps of 50 cm^{-1}. Vibrationally excited CO molecules in solid CO redistribute their energy primarily through vibrational–vibrational energy transfer. This is due to the large frequency-gap between

the vibrational mode of CO and the rotational and phonon modes of CO clusters. The CO VER exhibits a two-channel decay dependence on the frequency gap, analogous to the quantum mechanical prediction of CO VER switching from one-phonon to two-phonon assisted decay. The necessary physicochemical properties for VEP are well captured by the classical pair potentials used to simulate the VER of CO.

1.6 Outlook

The collection of works within this thesis not only present novel results, but also opportunities for furture works to continue advancing our understanding of the topics studied. In the works published much earlier, some of these new opportunities have already been taken and subsequent papers have been published by others. Here I briefly describe the works that have built off the works in each chapter (where available), and also outline other future prospects to come from each chapter.

The work presented in Chapter 5 has already been used in multiple subsequent works from other groups. Bariosco *et al.*[60] used the binding energy distributions calculated in Chapter 5 to solve the puzzling question of gaseous methonal detections in cold ISM conditions. They explained this strange observation by reasoning that methonal formed by multiple hydrogenations of CO could have a binding energy distributions as large as those seen for CO on CO. The low-end of this distribution would then be sufficiently weak to allow for desorption, hence explaining the observations. Enrique-Romero and Lamberts[61] used multiple CO cluster structures produced during the studies in Chapter 5 to investigate the formation of hydrogen cyanide and isocyanide in interstellar ices. The large amount of weakly bound sites reported in Chapter 5 has been used in several studies to explain experimental observations of CO desorption induced by low-energy photons.[62,63] These experimental observations are generally used to explain the observed gas-phase CO abundaces in cold ISM conditions, where CO is not expected to thermally desorb. Additional future works yet to be carried out are incorporating the binding energy distribution reported in an astrochemical model that utilizes distributions rather than single binding energy values. This work could potentially explain abundaces in gas-phase CO or other COMs, since diffusion and desorption would be increase by the low-end of the binding energy distribution.

The results described in Chapter 6 have also been used in multiple subsequent works from other groups. This work was partly inspired by the work of Santos *et al.*[64], where infrared-induced CO desorption was experimentally observed. The results in Chapter 6

show no significant transfer of vibrational energy to rotational or translational, in contradiction to the experimental work. Subsequent experimental studies based on the results from Chapter 6 found that the desorption did not originate from CO vibrations but rather thermalization of CO molecules or the vibrational motion of other molecules (*ie.* H_2O).[63,65] Additionally, Tsuge *et al.*[66] used the long VER timescales calculated in the work described in Chapter 6 to explain the formation of C_3O_2 in their experiments. The long VER timescales gave vibrationally excited CO molecules sufficient time to react with CCO, where the excitation energy was sufficient to surmount the reaction barrier. Finally, future studies that may still come from the work in Chapter 6 are those that apply the novel analysis technique for studying VER on other systems. This method could be quite useful for studying the VER of systems with more distinct energy gaps between different vibrational modes.

1.A Bibliography

[1] Louis J Allamandola, Max P Bernstein, Scott A Sandford, and Robert L Walker. Evolution of interstellar ices. *Space Science Reviews*, 90(1):219–232, 1999.

[2] EL Gibb, DCB Whittet, ACA Boogert, and AGGM Tielens. Interstellar ice: the infrared space observatory legacy. *The Astrophysical Journal Supplement Series*, 151(1):35, 2004.

[3] AC Adwin Boogert, Perry A Gerakines, and Douglas CB Whittet. Observations of the icy universe. *Annual Review of Astronomy and Astrophysics*, 53(1):541–581, 2015.

[4] Simon CO Glover, Christoph Federrath, M-M Mac Low, and Ralf S Klessen. Modelling CO formation in the turbulent interstellar medium. *Monthly Notices of the Royal Astronomical Society*, 404(1):2–29, 2010.

[5] Carina Arasa, Marc C van Hemert, Ewine F van Dishoeck, and Geert-Jan Kroes. Molecular dynamics simulations of CO_2 formation in interstellar ices. *The Journal of Physical Chemistry A*, 117(32):7064–7074, 2013.

[6] RL Hudson and MH Moore. Laboratory studies of the formation of methanol and other organic molecules by water+ carbon monoxide radiolysis: Relevance to comets, icy satellites, and interstellar ices. *Icarus*, 140(2):451–461, 1999.

[7] Robin T Garrod and Tyler Pauly. On the formation of CO_2 and other interstellar ices. *The Astrophysical Journal*, 735(1):15, 2011.

[8] SA Corcelli and JC Tully. Vibrational energy pooling in CO on NaCl (100): Methods. *The Journal of Chemical Physics*, 116(18):8079–8092, 2002.

[9] SA Corcelli and JC Tully. Vibrational energy pooling in CO on NaCl (100): Simulation and isotope effects. *The Journal of Physical Chemistry A*, 106(45): 10849–10860, 2002.

[10] Jascha A Lau, Li Chen, Arnab Choudhury, Dirk Schwarzer, Varun B Verma, and Alec M Wodtke. Transporting and concentrating vibrational energy to promote isomerization. *Nature*, 589(7842):391–395, 2021.

[11] Aidan P Thompson, H Metin Aktulga, Richard Berger, Dan S Bolintineanu, W Michael Brown, Paul S Crozier, Pieter J In't Veld, Axel Kohlmeyer, Stan G Moore, Trung Dac Nguyen, *et al.* LAMMPS - a flexible simulation tool for particle-based materials modeling at the atomic, meso, and continuum scales. *Computer Physics Communications*, 271:108171, 2022.

[12] David Van Der Spoel, Erik Lindahl, Berk Hess, Gerrit Groenhof, Alan E Mark, and Herman JC Berendsen. GROMACS: fast, flexible, and free. *Journal of Computational Chemistry*, 26(16):1701–1718, 2005.

[13] Erik Lindahl, Berk Hess, and David Van Der Spoel. GROMACS 3.0: a package for molecular simulation and trajectory analysis. *Molecular Modeling Annual*, 7 (8):306–317, 2001.

[14] Sander Pronk, Szilárd Páll, Roland Schulz, Per Larsson, Pär Bjelkmar, Rossen Apostolov, Michael R Shirts, Jeremy C Smith, Peter M Kasson, David Van Der Spoel, *et al.* GROMACS 4.5: a high-throughput and highly parallel open source molecular simulation toolkit. *Bioinformatics*, 29(7):845–854, 2013.

[15] Mark James Abraham, Teemu Murtola, Roland Schulz, Szilárd Páll, Jeremy C Smith, Berk Hess, and Erik Lindahl. GROMACS: High performance molecular simulations through multi-level parallelism from laptops to supercomputers. *SoftwareX*, 1:19–25, 2015.

[16] Samuel S. Schoenholz and Ekin D. Cubuk. JAX, M.D: A framework for differentiable physics, 2020.

1.A Bibliography

[17] Joe G Greener. Differentiable simulation to develop molecular dynamics force fields for disordered proteins. *Chemical Science*, 15:4897–4909, 2024.

[18] Ask Hjorth Larsen, Jens Jørgen Mortensen, Jakob Blomqvist, Ivano E Castelli, Rune Christensen, Marcin Dułak, Jesper Friis, Michael N Groves, Bjørk Hammer, Cory Hargus, *et al.* The atomic simulation environment—a Python library for working with atoms. *Journal of Physics: Condensed Matter*, 29(27):273002, 2017.

[19] Jeff Bezanson, Alan Edelman, Stefan Karpinski, and Viral B Shah. Julia: A fresh approach to numerical computing. *SIAM Review*, 59(1):65–98, 2017.

[20] Herman JC Berendsen, James PM Postma, Wilfred F van Gunsteren, and Jan Hermans. Interaction models for water in relation to protein hydration. In *Intermolecular forces: proceedings of the fourteenth Jerusalem symposium on quantum chemistry and biochemistry held in jerusalem, israel, april 13–16, 1981*, pages 331–342. Springer, 1981.

[21] Herman JC Berendsen, J-Raúl Grigera, and Tjerk P Straatsma. The missing term in effective pair potentials. *Journal of Physical Chemistry*, 91(24):6269–6271, 1987.

[22] Kahled Toukan and Aneesur Rahman. Molecular-dynamics study of atomic motions in water. *Physical Review B*, 31(5):2643, 1985.

[23] William L Jorgensen, Jayaraman Chandrasekhar, Jeffry D Madura, Roger W Impey, and Michael L Klein. Comparison of simple potential functions for simulating liquid water. *The Journal of Chemical Physics*, 79(2):926–935, 1983.

[24] Jose LF Abascal and Carlos Vega. A general purpose model for the condensed phases of water: TIP4P/2005. *The Journal of Chemical Physics*, 123(23), 2005.

[25] JLF Abascal, E Sanz, R García Fernández, and C Vega. A potential model for the study of ices and amorphous water: TIP4P/Ice. *The Journal of Chemical Physics*, 122(23), 2005.

[26] Miguel A González and José LF Abascal. A flexible model for water based on TIP4P/2005. *The Journal of Chemical Physics*, 135(22), 2011.

[27] Christian J Burnham and Sotiris S Xantheas. Development of transferable interaction models for water. III. Reparametrization of an all-atom polarizable rigid model (TTM2–R) from first principles. *The Journal of Chemical Physics*, 116(4):1500–1510, 2002.

[28] Sotiris S Xantheas, Christian J Burnham, and Robert J Harrison. Development of transferable interaction models for water. II. Accurate energetics of the first few water clusters from first principles. *The Journal of Chemical Physics*, 116(4): 1493–1499, 2002.

[29] Christian J Burnham and Sotiris S Xantheas. Development of transferable interaction models for water. IV. A flexible, all-atom polarizable potential (TTM2-F) based on geometry dependent charges derived from an ab initio monomer dipole moment surface. *The Journal of Chemical Physics*, 116(12):5115–5124, 2002.

[30] George S Fanourgakis and Sotiris S Xantheas. The flexible, polarizable, thole-type interaction potential for water (TTM2-F) revisited. *The Journal of Physical Chemistry A*, 110(11):4100–4106, 2006.

[31] George S Fanourgakis and Sotiris S Xantheas. Development of transferable interaction potentials for water. V. Extension of the flexible, polarizable, Thole-type model potential (TTM3-F, v. 3.0) to describe the vibrational spectra of water clusters and liquid water. *The Journal of Chemical Physics*, 128(7), 2008.

[32] CJ Burnham, DJ Anick, PK Mankoo, and GF Reiter. The vibrational proton potential in bulk liquid water and ice. *The Journal of Chemical Physics*, 128(15), 2008.

[33] Taisuke Hasegawa and Yoshitaka Tanimura. A polarizable water model for intramolecular and intermolecular vibrational spectroscopies. *The Journal of Physical Chemistry B*, 115(18):5545–5553, 2011.

[34] Pengyu Ren and Jay W Ponder. Polarizable atomic multipole water model for molecular mechanics simulation. *The Journal of Physical Chemistry B*, 107(24): 5933–5947, 2003.

[35] Pengyu Ren and Jay W Ponder. Temperature and pressure dependence of the AMOEBA water model. *The Journal of Physical Chemistry B*, 108(35):13427–13437, 2004.

[36] Jay W Ponder, Chuanjie Wu, Pengyu Ren, Vijay S Pande, John D Chodera, Michael J Schnieders, Imran Haque, David L Mobley, Daniel S Lambrecht, Robert A DiStasio Jr, *et al.* Current status of the AMOEBA polarizable force field. *The Journal of Physical Chemistry B*, 114(8):2549–2564, 2010.

1.A Bibliography

[37] Lee-Ping Wang, Teresa Head-Gordon, Jay W Ponder, Pengyu Ren, John D Chodera, Peter K Eastman, Todd J Martinez, and Vijay S Pande. Systematic improvement of a classical molecular model of water. *The Journal of Physical Chemistry B*, 117(34):9956–9972, 2013.

[38] Chengwen Liu, Jean-Philip Piquemal, and Pengyu Ren. AMOEBA+ classical potential for modeling molecular interactions. *Journal of Chemical Theory and Computation*, 15(7):4122–4139, 2019.

[39] Chengwen Liu, Jean-Philip Piquemal, and Pengyu Ren. Implementation of geometry-dependent charge flux into the polarizable AMOEBA+ potential. *The Journal of Physical Chemistry Letters*, 11(2):419–426, 2019.

[40] Enrique Ricardo Batista. *Development of a new water-water interaction potential and application to molecular processes in ice*. University of Washington, 1999.

[41] K. T. Wikfeldt, E. R. Batista, F. D. Vila, and H. Jónsson. A transferable H_2O interaction potential based on a single center multipole expansion: SCME. *Phys. Chem. Chem. Phys.*, 15:16542–16556, 2013.

[42] Elvar Orn Jonsson, Asmus Ougaard Dohn, and Hannes Jonsson. Polarizable embedding with a transferable H_2O potential function I: Formulation and tests on dimer. *Journal of Chemical Theory and Computation*, 15(12):6562–6577, 2019.

[43] Elvar Orn Jonsson, Soroush Rasti, Marta Galynska, Jorg Meyer, and Hannes Jónsson. Transferable potential function for flexible H_2O molecules based on the single-center multipole expansion. *Journal of Chemical Theory and Computation*, 18(12):7528–7543, 2022.

[44] Volodymyr Babin, Claude Leforestier, and Francesco Paesani. Development of a "first principles" water potential with flexible monomers: Dimer potential energy surface, VRT spectrum, and second virial coefficient. *Journal of Chemical Theory and Computation*, 9(12):5395–5403, 2013.

[45] Volodymyr Babin, Gregory R Medders, and Francesco Paesani. Development of a "first principles" water potential with flexible monomers. II: Trimer potential energy surface, third virial coefficient, and small clusters. *Journal of Chemical Theory and Computation*, 10(4):1599–1607, 2014.

[46] Gregory R Medders, Volodymyr Babin, and Francesco Paesani. Development of a "first-principles" water potential with flexible monomers. III. Liquid phase properties. *Journal of Chemical Theory and Computation*, 10(8):2906–2910, 2014.

[47] Francesco Paesani. Getting the right answers for the right reasons: Toward predictive molecular simulations of water with many-body potential energy functions. *Accounts of Chemical Research*, 49(9):1844–1851, 2016.

[48] Jes K Jørgensen, Arnaud Belloche, and Robin T Garrod. Astrochemistry during the formation of stars. *Annual Review of Astronomy and Astrophysics*, 58(1): 727–778, 2020.

[49] EM Penteado, C Walsh, and HM Cuppen. Sensitivity analysis of grain surface chemistry to binding energies of ice species. *The Astrophysical Journal*, 844(1): 71, 2017.

[50] Kenji Furuya. A framework for incorporating binding energy distribution in gas-ice astrochemical models. *The Astrophysical Journal*, 974(1):115, 2024.

[51] Valentine Wakelam, J-C Loison, R Mereau, and M Ruaud. Binding energies: New values and impact on the efficiency of chemical desorption. *Molecular Astrophysics*, 6:22–35, 2017.

[52] Stefano Ferrero, Lorenzo Zamirri, Cecilia Ceccarelli, Arezu Witzel, Albert Rimola, and Piero Ugliengo. Binding energies of interstellar molecules on crystalline and amorphous models of water ice by ab initio calculations. *The Astrophysical Journal*, 904(1):11, 2020.

[53] Hiroshi Fujisaki and John E Straub. Vibrational energy relaxation in proteins. *Proceedings of the National Academy of Sciences*, 102(19):6726–6731, 2005.

[54] VP Zhdanov and KI Zamaraev. Vibrational relaxation of adsorbed molecules. Mechanisms and manifestations in chemical reactions on solid surfaces. *Catalysis Reviews*, 24(3):373–413, 1982.

[55] José I Pascual, Nicolas Lorente, Zhen Song, Horst Conrad, and H-P Rust. Selectivity in vibrationally mediated single-molecule chemistry. *Nature*, 423(6939): 525–528, 2003.

[56] Sander Woutersen and Huib J Bakker. Resonant intermolecular transfer of vibrational energy in liquid water. *Nature*, 402(6761):507–509, 1999.

[57] Sander Woutersen, Uli Emmerichs, Han-Kwang Nienhuys, and Huib J Bakker. Anomalous temperature dependence of vibrational lifetimes in water and ice. *Physical Review Letters*, 81(5):1106, 1998.

[58] John C Deàk, Stuart T Rhea, Lawrence K Iwaki, and Dana D Dlott. Vibrational energy relaxation and spectral diffusion in water and deuterated water. *The Journal of Physical Chemistry A*, 104(21):4866–4875, 2000.

[59] AJ Lock and HJ Bakker. Temperature dependence of vibrational relaxation in liquid H_2O. *The Journal of Chemical Physics*, 117(4):1708–1713, 2002.

[60] Vittorio Bariosco, Lorenzo Tinacci, Stefano Pantaleone, Cecilia Ceccarelli, Albert Rimola, and Piero Ugliengo. Gaseous methanol in cold environments: is thermal desorption from low binding energy sites the explanation? *Monthly Notices of the Royal Astronomical Society*, 539(1):82–94, 2025.

[61] Joan Enrique-Romero and Thanja Lamberts. The complex (organic) puzzle of the formation of hydrogen cyanide and isocyanide on interstellar ice analogues. *The Journal of Physical Chemistry Letters*, 15(30):7799–7805, 2024.

[62] Antoine B Hacquard, Romain Basalgète, Samuel Del Fré, Jozef Rakovskỳ, Alenjandro Rivero Santamaria, Ferdinand Benoit, Xavier Michaut, Géraldine Féraud, Mathieu Bertin, Maurice Monnerville, *et al.* Photodesorption of CO ices: Rotational and translational energy distributions. *The Journal of Chemical Physics*, 161(18), 2024.

[63] Laura Slumstrup, John D Thrower, Johanna GM Schrauwen, Thanja Lamberts, Emily R Ingman, Domantas Laurinavicius, Jessalyn DeVine, Jeroen Terwisscha van Scheltinga, Julia C Santos, Jennifer A Noble, *et al.* IR-induced CO photodesorption from pure CO ice and CO on amorphous solid water. *ACS Earth and Space Chemistry*, 2025.

[64] JC Santos, K-J Chuang, JGM Schrauwen, A Traspas Muiña, J Zhang, HM Cuppen, B Redlich, H Linnartz, and S Ioppolo. Resonant infrared irradiation of CO and CH_3OH interstellar ices. *Astronomy & Astrophysics*, 672:A112, 2023.

[65] L Slumstrup, JD Thrower, AT Hopkinson, G Wenzel, R Jaganathan, JGM Schrauwen, B Redlich, S Ioppolo, and L Hornekær. CO desorption from interstellar icy grains induced by IR excitation of superhydrogenated PAHs. *arXiv preprint arXiv:2507.07896*, 2025.

[66] Masashi Tsuge, Germán Molpeceres, Ryota Ichimura, Hideko Nomura, Kenji Furuya, and Naoki Watanabe. Formation of unsaturated carbon chains through carbon chemisorption on solid CO. *arXiv preprint arXiv:2509.16978*, 2025.

1.7 Bibliography

Chapter 2

Methods

This section covers a brief explanation of generic methodology used in different chapters of this thesis, including force fields, vibrational frequencies and molecular dynamics.

2.1 Force Fields

A force field is a vector field of non-contact forces acting on a particle at a certain position in space. Within theorectical chemistry, the term is used to refer to a potential that describes the forces and energies acting on a system of atomic particles. Various force fields have been used in the research carried out in this thesis. Although they are referred to as force fields, within theorectical chemistry the description focuses on terms contributing to the potential energy, which are traditionally physically motivated. Forces are naturally calculated by taking the negative gradient of the potential,

$$\vec{F} = -\vec{\nabla}V \tag{2.1}$$

where $\vec{F}$ is the force and V is the potential energy. The force fields used for the research within this thesis are explained within this section, along with a few general considerations.

2.1.1 General Considerations

The evaluation of a force field can be done with a distance-based cutoff, since at large distances interactions are negligible and ignoring them saves computational time. Additionally, to replicate bulk systems, force fields can be evaluated under periodic boundary conditions. In practice both of these techniques require careful implementation to avoid introducing artifacts in the potential energy of the system.

Smoothing Functions

In order to take the gradient of the potential, the potential must be differentiable (*ie.* smooth and continuous). A distance based cutoff for interactions would result in a non-smooth or continuous potential. As such, a smoothing function (also called switching function) needs to be introduced.

A smoothing function smoothly truncates the interaction energy at a given cutoff value. There are many smoothing functions available, an example is,

$$S(r) = \begin{cases} 1 & r \leq r_s \\ 2(\frac{r-r_s}{r_c-r_s})^3 - 3(\frac{r-r_s}{r_c-r_s})^2 + 1 & r_s < r \leq r_c \\ 0 & r > r_c \end{cases} \tag{2.2}$$

where r is the interaction distance, r_s is the distance at which smoothing starts, and r_c is the interaction cutoff. This smoothing function is then multiplied with the interaction energy to give the smoothed interaction potential. An important caveat from smoothing the interaction energy is that upon calculating the gradient, this will also result in additional terms for the forces. In the simplest case of an interaction potential depending only on distances, this results in:

$$-\frac{\partial}{\partial r} S(r)V(r) = -\frac{\partial S(r)}{\partial r} V(r) - S(r)\frac{\partial V(r)}{\partial r} \tag{2.3}$$

Without properly including the addtionaly forces terms the energy and forces will be divergent, which prevents geometry optimizations from succeeding and causes the total energy to not be conserved in NVE molecular dynamics simulations (*vide infra*).

Smoothing functions can be applied at the atomic level, or at the molecular level. Although both methods are possible it is important to note that frequently force fields are pair potentials, meaning the interaction energy is fitted for a pair interaction. In these cases applying a smoothing function at the atomic level will introduce artifacts, notably due to imbalances of the pair potential interactions. For these cases the smoothing function must be applied to all pair interactions based on the same pair distance (either the center of mass or a particular atom).

Periodic Boundary Conditions

To approximate the structure of bulk systems it is common to apply periodic boundary conditions (PBCs) to all particles within a unit cell. In Figure 2.1 an example of a

small unit cell under PBCs is shown.

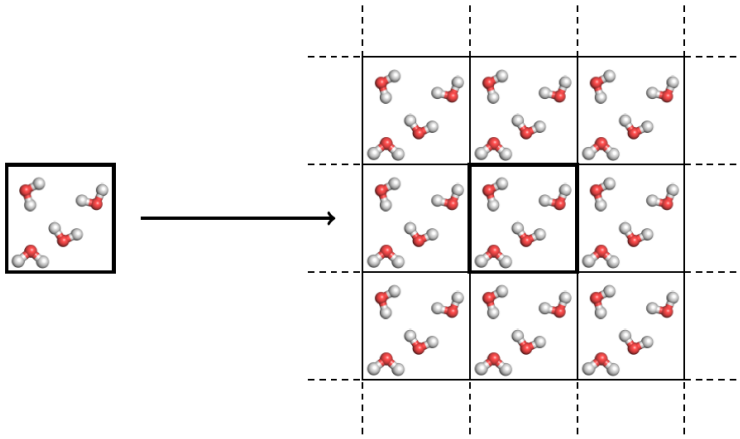

Figure 2.1: Illustration of how PBCs is used to approximate bulk structures. The prominent black box around 4 water molecules is the unit cell. Each cell surrounding the original unit cell contains images of the molecules within the unit cell.

An important consideration to avoid artifacts is that the total energy of the system should be consistent with the number of particles (or molecules) within the unit cell. As such, if all interactions between particles and images are counted, then interactions with images and particles can only add half their energy to the total energy of the system. Similarly, self-interactions (*ie.* a molecule interacting with its image) are forbidden, which arises from the extra total energy the system would have if these interactions are counted. A popular method for applying PBCs without violating these above stipulations is the minimum image convention (MIC).

Under the MIC only interactions between real particles and the closest representation (an image or real particle) of other particles is counted. In order to ensure that self-interactions are ignored under this convention, it is typically required that an interaction cutoff smaller than half the shortest cell length is used. To be clear, this means that two particles on opposite ends of a unit cell will only interact via the images that are closest to the other real particle.

2.1.2 Force Fields for H_2O

There exits a wide variety of force fields describing water, ranging from simple point charge models (SPC[1], SPC/E[2], SPC-F[3], and TIP4P[4]) to highly sophisticated many-body polarizable models (TTMx-F[5–10], POLI2VS[11], AMOEBA[12–17], SCME/f[18–21], and MB-pol[22–25]). The work in this thesis utilizes two of the highly sophisticated many-body polarizable models, MB-pol & SCME/f, which are briefly explained here.

MB–pol

MB-pol[22–25] is derived from the many-body expansion (MBE) of the interaction energy between water molecules. The MBE for a system of N molecules is given by,

$$V = \sum_{i=1}^{N} V_{1B}(i) + \sum_{i<j}^{N} V_{2B}(i,j) + \ldots + V_{NB}(1,\ldots,N) \tag{2.4}$$

where V_{1B} is the one-body potential, V_{2B} is the two-body potential, and V_{NB} is the N-body potential. The i and j indexes run over all atoms in each molecule for all pairs of molecules in the system. The MB-pol potential only extends to the three-body term in the MBE, and includes addtional dispersion and electrostatic terms. The total MB-pol energy is given by,

$$V = V_{1B} + V_{2B} + V_{3B} + V_{\text{Dispersion}} + V_{\text{Electrostatics}} \tag{2.5}$$

where $V_{\text{Dispersion}}$ is the dispersion interaction energy, and $V_{\text{Electrostatics}}$ is the electrostatic interaction energy.

The one-body term in MB-pol is taken from Partridge and Schwenke[26], which is the gold standard of one-body water potentials. The two-body potential is given by,

$$V_{2B} = \sum_{i<j}^{N} S(r_{O_i,O_j}) V_{2B-PIP}(X_i, X_j) \tag{2.6}$$

where N is the number of molecules, r_{O_i,O_j} is the distance between the ith and jth oxygen atom positions, X_i and X_j are the ith and jth molecule positions (all atoms plus two lone-pair sites), S is the switching function, and V_{2B-PIP} is the two-body PIP potential. Figure 2.2 shows the interaction sites of the MB-pol pair potential.

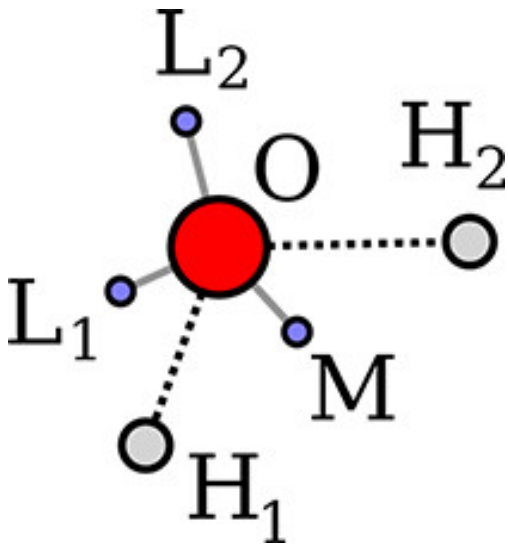

Figure 2.2: Interaction sites of MB-pol pair potential. Figure taken from Babin *et al.* [22].

The dispersion interaction is also a two-body interaction within MB-pol given by,

$$V_{\text{Dispersion}} = \sum_{i<j}^{N} f_6(r_{ij}) \frac{C_6^{(ij)}}{r_{ij}^6} + f_8(r_{ij}) \frac{C_8^{(ij)}}{r_{ij}^8} \tag{2.7}$$

where f_n are the Tang-Toennies damping functions [27], C_n are constants, and r_{ij} is the distance between the ith and jth atoms.

The electrostatic potential, within the MB-pol(2023) model, is composed of four terms; the charge–charge interactions (V_{qq}), charge–dipole interactions ($V_{q\mu}$), dipole–dipole interactions ($V_{\mu\mu}$), and the many-body polarization (V_{pol}).

$$V_{qq} = \sum_{b>a}^{n} q_a \hat{T}_{ab} q_b \tag{2.8}$$

$$V_{q\mu} = \sum_{b>a}^{n} (\mu_a^{\alpha} \hat{T}_{ab}^{\alpha} q_b - q_a \hat{T}_{ab}^{\alpha} \mu_b^{\alpha}) \tag{2.9}$$

$$V_{\mu\mu} = -\sum_{b>a}^{n} \mu_a^{\alpha} \hat{T}_{ab}^{\alpha\beta} \mu_b^{\beta} \tag{2.10}$$

$$V_{\text{pol}} = \frac{1}{2} \sum_{a=1}^{n} \mu_a \hat{\alpha}_a^{-1} \mu_a \tag{2.11}$$

In the above equations for the electrostatic terms n is the total number of electrostatic sites, q_a is the charge of site a, μ_a is the dipole of site a, $\hat{\alpha}_a$ is the polarizability of site a, Greek superscripts define Cartesian coordinates where Einstein notation is used for repeated superscripts, and $\hat{T}$ terms are the electrostatic tensors. The tensors are given by,

$$\hat{T}_{ab} = S_0(R_{ab}) \frac{1}{R_{ab}} \tag{2.12}$$

$$\hat{T}_{ab}^{\alpha} = \nabla_{\alpha} \hat{T}_{ab} = -S_1(R_{ab}) \frac{R_{ab}^{\alpha}}{R_{ab}^3} \tag{2.13}$$

$$\hat{T}_{ab}^{\alpha\beta} = \nabla_{\alpha} \hat{T}_{ab}^{\beta} = S_2(R_{ab}) \frac{3R_{ab}^{\alpha} R_{ab}^{\beta}}{R_{ab}^5} - S_1(R_{ab}) \frac{\delta_{ab}}{R_{ab}^3} \tag{2.14}$$

where R_{ab} is the distance between sites a and b, S_n are the screening functions, and δ is the Kronecker delta. The screening functions are given by,

$$S_0(R_{ab}) = 1 - \exp\left(-\omega(\frac{R_{ab}}{A})^4\right) + \frac{\omega^{\frac{1}{4}} R_{ab}}{A} \Gamma\left(\frac{3}{4}, \omega(\frac{R_{ab}}{A})^4\right) \tag{2.15}$$

$$S_1(R_{ab}) = 1 - \exp\left(-\omega(\frac{R_{ab}}{A})^4\right) \tag{2.16}$$

$$S_2(R_{ab}) = S_1(R_{ab}) - \frac{4\omega}{3} (\frac{R_{ab}}{A})^4 \exp\left(-\omega(\frac{R_{ab}}{A})^4\right) \tag{2.17}$$

where ω is the Thole damping factor, $A = (\alpha_a \alpha_b)^{\frac{1}{6}}$, and α is the polarizability.

SCME/f

The flexible single-center multipole expansion (SCME/f)[18–21] potential is another many-body water potential. The total interaction energy is given by,

$$V = V_{1B} + V_{2B} + V_{\text{Dispersion}} + V_{\text{Electrostatics}} \tag{2.18}$$

where V_{1B} is the one-body potential, V_{2B} is the two-body potential, $V_{\text{Dispersion}}$ is the dispersion interaction energy, and $V_{\text{Electrostatics}}$ is the electrostatic interaction energy. The one-body potential is identical to the one used in MB-pol (described above).

The two-body potential employs a Born-Mayer potential,

$$V_{2B} = \sum_{i<j} A r_{ij}^{-k} e^{-h r_{ij}} \tag{2.19}$$

where r_{ij} is the distance between the ith and jth oxygen atoms, and A, k, & h are constants which can be found in Jónsson *et al.*[21].

The dispersion energy is similar to that of MB-pol but with an additional term.

$$V_{\text{Dispersion}} = \sum_{i<j}^{N} f_6(r_{ij}) \frac{C_6^{(ij)}}{r_{ij}^6} + f_8(r_{ij}) \frac{C_8^{(ij)}}{r_{ij}^8} + f_{10}(r_{ij}) \frac{C_{10}^{(ij)}}{r_{ij}^{10}} \tag{2.20}$$

Again, here f_n are the Tang-Toennies damping functions[27], C_n are constants, and r_{ij} is the distance between the ith and jth atoms. The i and j indicies run over all atoms in each molecule for all pairs of molecules in the system. The electrostatic energy is given by,

$$V_{\text{electrostatic}} = V_{\text{in+pol}} + V_{\text{self}} \tag{2.21}$$

where $V_{\text{in+pol}}$ is the combination of the electrostatic interaction between intrinsic molecular moments and the field-induced polarization energy, and V_{self} is the self-energy. The self-energy is the energy required to polarize a molecule and is given by,

$$V_{\text{self}} = -\frac{1}{2} \sum_{i}^{N} (\Delta\mu_\alpha^i V_\alpha^i + \frac{1}{3} \Delta\theta_{\alpha\beta}^i) V_{\alpha\beta} \tag{2.22}$$

where Einstein notation is used for the Greek indicies, $\Delta\mu$ is the change in the dipole moment due to the field-induced polarization, and $\Delta\theta$ is the change in the quadrupole

moment due to the field-induced polarization. The other term is given by,

$$V_{\text{in+pol}} = \frac{1}{2}\sum_{i}^{N}[(\mu_\alpha^i(r^{ia}) + \Delta\mu_\alpha^i)V_\alpha^i + \frac{1}{3}(\theta_{\alpha\beta}^i(r^{ia}) + \Delta\theta_{\alpha\beta}^i)V_{\alpha\beta} + \frac{1}{15}\Omega_{\alpha\beta\gamma}^i V_{\alpha\beta\gamma}^i + \frac{1}{105}\Phi_{\alpha\beta\gamma\delta}^i V_{\alpha\beta\gamma\delta}^i] \quad (2.23)$$

where Ω is the octupole, and Φ is the hexadecapole.

2.1.3 Force Fields for CO

Compared to water there are significantly fewer force fields developed for studying carbon monoxide. The generic COMPASS force field was parameterized for 14 inorganic molecules, one of them being CO.[28] Beyond generic potentials being fitted to CO, there are two potentials focusing specifically on CO. The first is a site-site pair potential[29], and the other a neural network potential based on permutation-invariant polynomials (PIP–NN)[30].

Site-Site Pair Potential

This potential was originally developed by van Hemert *et al.*[29], where it models CO interactions as a site-site pair potential that was parameterized using CCSD(T) calculations for the CO dimer with the aug-cc-pVQZ basis set in combination with the Boys-Bernardi counterpoise correction. The values for all parameters in the force field are summarized in Table 2.1.

	$V_{\textbf{Morse}}$		
	r_e (Å)	D_e (eV)	γ (Å^{-1})
	1.1282	11.23	2.3281
	$V_{\textbf{exch}} + V_{\textbf{disp}}$		
i,j	A_{ij} (eV)	B_{ij} (Å^{-1})	C_{ij} (eVÅ^6)
C,C	361.36	2.836	33.37
O,O	6370.10	4.253	10.52
C,O	1516.74	3.544	15.16
	$V_{\textbf{el}}$		
i	Q_i^0 (e)	σ_i (Å^{-1})	
C	-0.47	3.845	
O	-0.615	2.132	

Table 2.1: CO-CO Potential Parameters

The interaction potential is composed of an intramolecular Morse potential (V_{Morse}), and intermolecular contributions that are intended to capture exchange (V_{exch}), dispersion (V_{disp}), and electrostatic (V_{el}) interactions between pairs of CO molecules:

$$V = V_{\text{Morse}} + V_{\text{exch}} + V_{\text{disp}} + V_{\text{el}} \tag{2.24}$$

The Morse potential is given by

$$V_{\text{Morse}} = \sum_{i=1}^{N} D_{\text{e}}(1 - e^{-\gamma(r_i - r_{\text{e}})})^2, \tag{2.25}$$

where D_{e} is the dissociation energy, r_i is the CO bond length of the ith molecule, r_{e} is the equilibrium CO bond length, N is the number of molecules in the system, and γ a constant given in Table 2.1. All of the Morse potential parameters were obtained from fitting to experimental data. A Buckingham potential is used for the exchange and dispersion contributions.

$$V_{\text{exch}} + V_{\text{disp}} = \sum_{ij \mid i<j} A_{ij} e^{-B_{ij} r_{ij}} - \frac{C_{ij}}{r_{ij}^6} \tag{2.26}$$

Here, r_{ij} is the distance between the ith and jth atoms, and all other terms (A_{ij}, B_{ij}, C_{ij}) are constants, given in Table 2.1. Note, i and j are atoms of different molecules. Finally, the electrostatic contribution is given by

$$V_{\text{el}} = \sum_{ij \mid i<j} \frac{1}{4\pi\epsilon_0} \frac{Q_i Q_j}{r_{ij}}, \tag{2.27}$$

where ϵ_0 is the vaccum dielectric constant, and the point charges Q_i and Q_j are each located on a different molecule at a distance r_{ij} with respect to each other. The C and the O atom form negative charge centers. A compensating total positive charge, $Q = -(Q_C + Q_O)$, is placed on the center of mass of each molecule, resulting in 9 Coulomb interactions between each pair of CO molecules. The charges mimic the *ab-initio* derived dipole and quadrupole moments. The moments were originally calculated using MCSCF/CCI calculations with the aug-cc-pVQZ basis set [29] and the coordinate-dependence of the charges is given by,

$$Q_i = Q_i^0 e^{\sigma_i(r_i - r_e)} \tag{2.28}$$

where r_i is the intramolecular CO distance, Q_i^0 is the charge distribution at the equilibrium bond length and σ_i is a constant, given in Table 2.1.

PIP–NN

This potential was originally developed by Chen *et al.*[30], and unlike potentials described by physically based interaction equations, PIP–NN potentials do not have parameters that can be directly linked to physical or chemical properties.

The total energy V is represented by the sum of the intramolecular V_{intra} and intermolecular V_{inter} potential energies.

$$V = V_{\text{intra}} + V_{\text{inter}} \tag{2.29}$$

The intramolecular energy is given by,

$$V_{\text{intra}} = b_2 + \vec{w}_2 \cdot \tanh(\vec{b}_1 + \vec{w}_1 x) \tag{2.30}$$

where b_2 & $\vec{b}_1$ are biases, $\vec{w}_1$ & $\vec{w}_2$ are weights and x is the bond length.[1] The intermolecular potential is a 2-layer PIP–NN given by,

$$V_{\text{inter}} = b_5 + \vec{w}_3 \cdot \tanh(\vec{b}_4 + W_2 \tanh(\vec{b}_3 + W_1 \vec{G})) \tag{2.31}$$

where $\vec{b}_3$, $\vec{b}_4$ & b_5 are biases, $\vec{w}_3$ is a weight, W_1 & W_2 are also weights but capitalized to denote matrices, and $\vec{G}$ is the symmetry functions. The symmetry functions are permutation invariant polynomials related to the distances between pairs of CO molecules.

$$\begin{aligned}
G_1 &= p_{O1,C1} + p_{O2,C2} \\
G_2 &= p_{O1,C2} + p_{O2,C1} \\
G_3^2 &= p_{O1,C1}^2 + p_{O2,C2}^2 \\
G_4^2 &= p_{O1,C2}^2 + p_{O2,C1}^2 \\
G_5^2 &= p_{O1,C1} p_{O1,C2} + p_{O2,C2} p_{O2,C1} \\
G_6 &= p_{O1,O2} \\
G_7 &= p_{C1,C2}
\end{aligned}$$

The above 7 functions are all the symmetry functions for this potential, with p_{ij} given

[1] tanh applied on a vector is done by applying tanh element-wise.

by,

$$p_{ij} = \exp(-\lambda r_{ij}) \tag{2.32}$$

where $\lambda = 0.3$[30] is an empirical parameter, and r_{ij} is the distance between atoms i and j.

An implementation of this potential in Julia can be found in YASS, which was developed during this PhD.

2.2 Geometry Optimization

Computing the optimized geometry, i.e., the atomic structure that minimizes the energy, of a system is often the first step in molecular simulations. For vibrational analysis this step ensures that the "imaginary modes", i.e., modes that represent motion toward a minimum on the systems potential energy surface, are not calculated. For molecular dynamics simulations, this step provides a stable starting point for simulations, which avoids unwanted simulation results.

Geometry optimization is done by using mathematical optimization techniques on the energy of the system as function of the $3N$ atomic coordinates of the system ($E(r_1, \ldots, r_{3N})$). The solution is one where the derivative of the energy with respect to all coordinates is zero ($\frac{\partial E}{\partial r_i} = 0$), and the Hessian matrix ($\frac{\partial^2 E}{\partial r_i \partial r_j}$) is positive semi-definite, i.e. all of its eigenvalues are non-negative. In computer simulations finding the solution is done iteratively, where several algorithms exist but the general concepts are consistent. Here I cover the gradient descent optimizer, also known as steepest descent, which serves as a simple model for explaining the concepts of geometry optimization.

Gradient descent assumes the objective function, the function being minimized, is defined and differentiable which is always the case for the energy of a system. It then follows that the object function decreases the fastest when traversing in the negative gradient of the function. In simulations this is done iteratively by traveling in steps along the negative gradient, typically via

$$R_{n+1} = R_n - \eta \nabla E(R) \tag{2.33}$$

where η is the step size, R is the $3N$ atomic coordinates and $E(R)$ the energy (or objective function). This is repeated until either reaching the maximum number of iterations or a convergence threshold on either the energy, gradient of the energy or the change in coordinates. Other more sophisticated optimization algorithms are typically used, however, the core concept of iteratively minimizing the energy until convergence

is consistent.

An important consideration here is that the optimization algorithm finds the nearest local minima, not the global minima. This means the optimized geometry found is dependent on the initial geometry supplied to the optimization routine. Algorithms that seek to find the global minia also exist but are more computationally demanding.

2.3 Vibrational Analysis

Vibrational frequency calculations are of great interest since vibrational properties of solids are accessible through different experimental techniques. Here I briefly describe two commonly used computational methods to calculate vibrational density of states (VDOS) that can be used with the force fields presented in the previous section.

2.3.1 Harmonic Approximation

To better understand the harmonic approximation it is beneficial to first briefly cover the physics of a much simpler system. Consider a frictionless system where a mass is attached to a massless spring attached to a wall (see Figure 2.3).

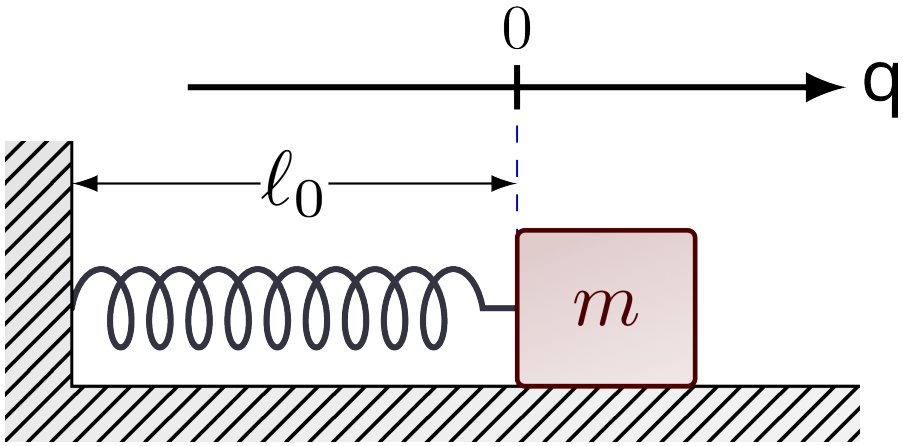

Figure 2.3: An illustration of a mass attached to a massless spring attached to a wall.

In order to simplify the problem we take the coordinate system where q is defined as the displacement of the mass (m) from its equilibrium position. The kinetic energy is then given by,

$$T = \frac{1}{2} m \dot{q}^2 \tag{2.34}$$

where T is kinetic energy, m is the mass, and $\dot{q}$ is the time derivative of the coordinate q. Assuming a spring constant of k, then the potential energy is as follows.

$$V = \frac{1}{2}kq^2 \tag{2.35}$$

The equations of motion for this system are then given by,

$$\frac{d}{dt}\frac{\partial T}{\partial \dot{q}} + \frac{\partial V}{\partial q} = 0 \tag{2.36}$$

$$m\ddot{q} = -kq \tag{2.37}$$

where $\ddot{q}$ is the second time derivative of q. Solving this differential equation gives a description of the motion,

$$q(t) = A\sin(2\pi\sqrt{\frac{k}{m}}t + \phi) \tag{2.38}$$

where A is a constant describing the amplitude of the oscillations, ϕ is a constant descibing the phase of the oscillations, and the frequency of the oscillations is given by $\sqrt{\frac{k}{m}}$. This simple system is commonly referred to as a harmonic oscillator, and the solution to the differential equation is the normal mode of the system.

This same process can be applied to more complex systems to calculate the normal modes of the system. Consider a 3-dimensional system with N atoms at equilibrium. The problem can be simplified by changing the coordinates to mass weighted displacements of the atoms from equilibrium, ie., defining the coordinates $q_1 = \sqrt{m_1}\Delta x_1$, $q_2 = \sqrt{m_1}\Delta y_1$, ..., $q_{3N} = \sqrt{m_N}\Delta z_N$. The kinetic energy of the system is given by the following expression.

$$T = \sum_{i}^{3N} \dot{q}_i^2 \tag{2.39}$$

A generalized potential energy for the system, which is valid for any interaction potentials, is less straightforward. In order to achieve it, a Taylor series expansion of the potential is taken about the equilibrium position.

$$V = V_0 + \sum_{i}^{3N} \frac{\partial V}{\partial q_i}\bigg|_0 q_i + \sum_{i,j}^{3N} \frac{\partial^2 V}{\partial q_i \partial q_j}\bigg|_0 q_i q_j + \dots \tag{2.40}$$

The approximation in the term "harmonic approximation" comes in at this stage, where the vibrations are assumed to be small and so the potential energy is truncated

at the third term in the Taylor series expansion. The remaining expression is further simplified by defining that the potential energy at equilibrium is zero ($V_0 = 0$). Similarly, the gradient of the potential at equilibrium is zero ($\frac{\partial V}{\partial q_i}\Big|_0 = 0$), as defined by the optimization of the system (*ie.* the equilibrium point of a system is where the gradient of potential energy is zero). Resulting in the following potential energy for the system.

$$V = \sum_{i,j}^{3N} \frac{\partial V}{\partial q_i \partial q_j}\bigg|_0 q_i q_j = \sum_{i,j}^{3N} f_{ij} q_i q_j \tag{2.41}$$

Newton's equations of motion (one equation for each $j = 1, ..., 3N$ coordinate) for this system are given by the following expressions.

$$\frac{d}{dt}\frac{\partial T}{\partial \dot{q}_j} + \frac{\partial V}{\partial q_j} = 0 \tag{2.42}$$

$$\ddot{q}_j = -\sum_{i}^{3N} f_{ij} q_i \tag{2.43}$$

This gives $3N$ coupled differential equations, each of which bears a remarkable similarity to Equation (2.37). Analogous to the one-dimensional harmonic oscillator above, we make the following ansatz:

$$q_j(t) = A_j \sin(2\pi\sqrt{\lambda}t + \epsilon) \tag{2.44}$$

Here, A_j is the amplitude of the jth coordinate, λ is the frequency, and ϵ is the phase. To solve for the frequencies the ansatz is substituted into Equation (2.43).

$$-A_j\lambda \sin(\sqrt{\lambda}t + \epsilon) = -\sum_{i}^{3N} f_{ij} A_i \sin(\sqrt{\lambda}t + \epsilon) \tag{2.45}$$

$$-A_j\lambda = -\sum_{i}^{3N} f_{ij} A_i \tag{2.46}$$

$$\sum_{i}^{3N} f_{ij} A_i - A_j\lambda = 0 \tag{2.47}$$

$$\sum_{i}^{3N} (f_{ij} - \delta_{ij}\lambda) A_i = 0 \tag{2.48}$$

In Equation (2.48) δ_{ij} is the Kronecker delta. Only for certain values of λ does

Equation (2.48) have a non-trivial (*ie.* $A_i \neq 0$) solution. These particular values can be determined by solving the characteristic equation.

$$\begin{bmatrix} f_{11}-\lambda & f_{12} & \dots & f_{1,3N} \\ f_{21} & f_{22}-\lambda & \dots & f_{2,3N} \\ \dots & \dots & \dots & \dots \\ f_{3N,1} & \dots & \dots & f_{3N,3N}-\lambda \end{bmatrix} = 0 \tag{2.49}$$

In total there should be $3N$ values of λ that satisfy the non-trivial solution criteria. Some of these values may be identical to another value, these are called degenerate values. When V describes an internal interaction potential, $3N-6$ λ values correspond to the vibrational frequencies under the harmonic approximation, which are commonly referred to as normal mode frequencies. The exact solutions for the other 6 λ values is 0, and these solutions correspond to centre-of-mass translation and rotations of the entire system.

Figure 2.4 shows an example of the normal modes frequencies calculated for a bulk ice Ih cell with 768 molecules using the TIP4P/2005f potential. The histogram shows the OH stretching mode (3000 – 3400 cm^{-1}), the water bending mode ($\approx$ 1800 cm^{-1}), the water librational mode (500 – 1000 cm^{-1}), and the lattice modes ($<$ 500 cm^{-1}) of the hexagonal phase of ice (ice Ih).

Normal mode analysis results in $3N-6$ number of modes, where N is the number of atoms. When a large system is used and the modes are plotted as a histogram, the density of states becomes clear. For small systems the number of modes will not be large enough to produce a statistically converged sampling of the density of states of real systems. In computational practice, this method requires highly optimized systems, to avoid imaginary modes, which results in the frequencies being devoid of temperature information. In order to artificially smear the frequencies to model temperature effects the frequencies can be broadened with a Gaussian or Lorentzian lineshape. However, these artificial line broadening techniques do not capture the reallity of the thermal occupancy of the system, so care must be taken when using this technique.

2.3.2 Velocity Autocorrelation Function

Autocorrelation is the measure of correlation between a signal and a time-delayed copy of itself. This is used to identify periodic trends, even those obscured by noise, within timeseries. In atomistic simulations the VACF is a method for identifying

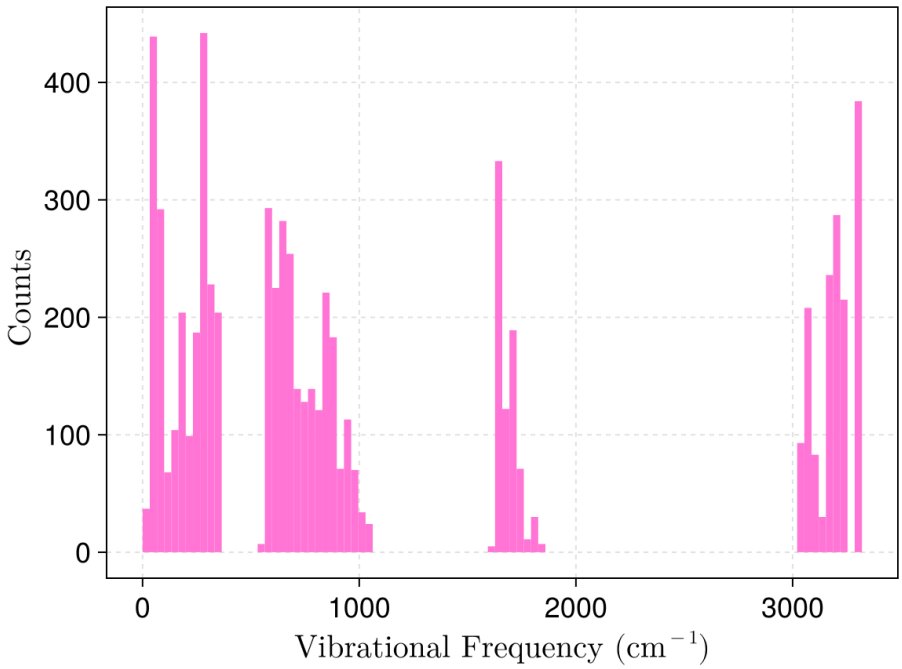

Figure 2.4: A histogram of the frequencies calculated from a normal mode analysis under the harmonic approximation. These frequencies are calculated for a bulk ice Ih cell using the TIP4P/2005f potential.

periodic motion of atoms (*ie.* vibrational modes). Taking the Fourier transform of the VACF gives the vibrational density of states (VDOS) of the system. For the sake of computational efficiency, the fast Fourier transform (FFT) is typically used. The VACF is given by,

$$< v(t) \cdot v(t - \Delta t) >= \frac{1}{M} \sum_{i}^{M} \frac{1}{N} \sum_{j}^{N} v_j(t_i) \cdot v_j(t_i - \Delta t) \tag{2.50}$$

where v is the velocity of an atom, M is the total number of timesteps, N is the total number of atoms, t is the time, and Δt is the timestep. In practice this expression is not used to calculate the VACF since it is slow, instead an FFT of the velocity timeseries is taken then multiplied by its conjugate and run through an inverse FFT. This is a significantly faster way of calculating the VACF, as long as the FFT algorithm is sufficiently fast. The majority of codes that calculate the VACF employ this technique.

The result of this is typically normalized by the total number of timesteps, resulting in a VDOS where the scale is proportional to the strength of the oscillation at a particular frequency.

Additional consideration also needs to be taken to avoid spectral leakage, a phenomenon in signal processing where the energy of a single frequency is spread across several frequency bins. Spectral leakage is caused by signals that are non-periodic within the time window. This will always be true when performing VACF analysis, but can be reduced by using a window function that smooths the signal edges. Some commonly used window functions are the Hann and Welch window functions.

The frequency resolution is determined via,

$$\Delta\omega = \frac{f_s}{cn} \tag{2.51}$$

where $\Delta\omega$ is the frequency resolution in wavenumber (cm^{-1}), f_s is the sampling frequency, c is the speed of light, and n is the number of timesteps in the trajectory. The maximum frequency is then given by,

$$\omega_{\max} = \Delta\omega\frac{n}{2} = \frac{f_s}{2c} \tag{2.52}$$

where the half factor comes from slicing the frequencies to be only those that are positive. From these equations it is clear that the frequency resolution and the largest frequency are determined by the MD timestep size and the length of the MD trajectory.

The velocitity data used in the VACF is taken from MD simulations, where the total number of timesteps determines the largest observable frequency and the size of the timestep the resolution of the VDOS. Additionally, the signal-to-noise of the VDOS can be improved by taking a long MD simulation (*ie.* 200 ps) slicing it into several timeseries of smaller duration (keeping in mind the length determines the highest frequency in the VDOS), then computing the VDOS of each timeseries and averaging them all.

Besides decreasing the size of the timestep in the MD simulation there are a few other tricks that can artificially increase the resolution of the calculated VDOS. One can mirror their VACF signal, pad the ends of the signal with zeros, or do both (note that zero padding must be done before mirroring to maintain symmetry). These tricks artificially increase the resolution of the VDOS, which means that small features might be blurred out despite the resolution improving.

Figure 2.5 shows the VDOS of a bulk Ih cell with 768 molecules calculated through

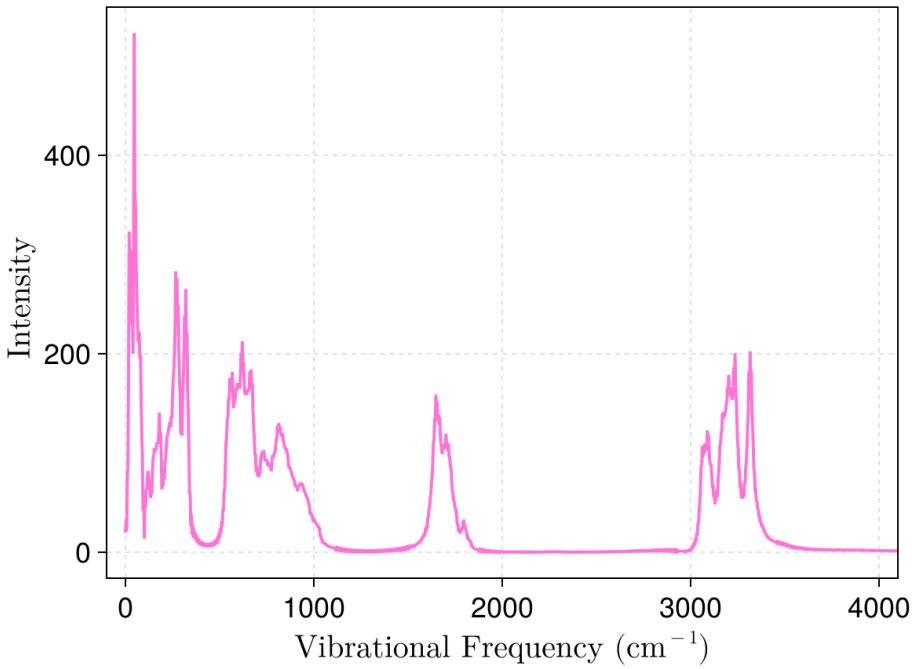

Figure 2.5: The VDOS of a bulk Ih cell with 768 molecules calculated through the VACF method using TIP4P/2005f. A 15 ps long MD simulation at 120 K (*vide infra*) was sliced into 3 5 ps long trajectories, where the VACF was calculated for each slice. A Welch window and mirroring was used on the autocorrelation signal, however, no zero-padding was used. The VDOS from the slices were averaged to produce this plot.

the VACF method. All of the same modes seen in Figure 2.4 can be seen here as well, however, here anharmonicity and temperature effects are included.

2.4 Molecular Dynamics

Molecular dynamics (MD) is a computational method for simulating the dynamics of atomic (or molecular) systems in a particular statistical ensemble. The statistical ensemble of the system, Figure 2.6 illustrates the possible ensembles, represents which thermodynamic properties of the system are held constant and which are free to vary with time. Within this thesis only the microcanonical and canonical ensembles are used, as such, only those two will be explained here. The dynamical motion of the system is calculated by solving Newton's equations of motion for a given system,

where the forces on the atoms are used to calculate the accelerations of the atoms. MD simulations provide insights into a wide range of dynamic properties, and are used across various fields of research such as physics, chemistry, materials science and biology.

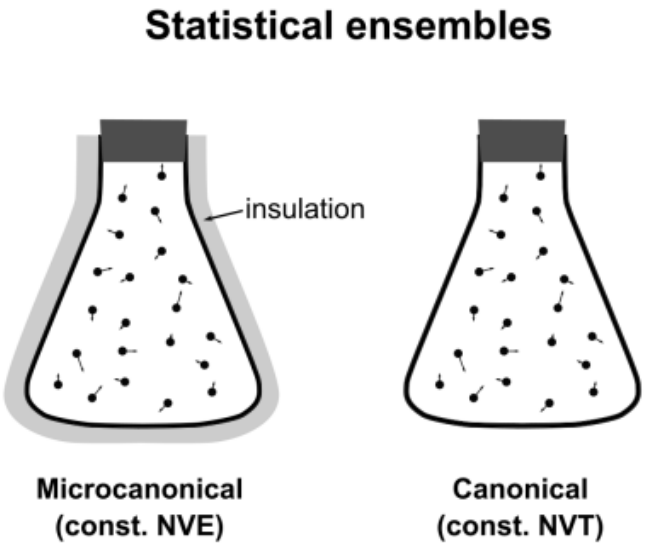

Figure 2.6: Illustration of the different statistical ensembles for thermodynamic systems. This illustration was taken from Wikimedia Commons and is free to use and share under the Creative Commons license.

A simple MD simulation only requires an integrator and a force field. As the name implies, the former integrates the equations of motion to update positions and velocities for the particles in the system. The most commonly employed MD integrator is the Velocity-Verlet integration scheme, which calculates both the velocity and position of a particle at a moment in time.

$$x(t + \Delta t) = x(t) + v(t)\Delta t + \frac{1}{2}a(t)\Delta t^2 \tag{2.53}$$

$$v(t + \Delta t) = v(t) + \frac{a(t) + a(t + \Delta t)}{2}\Delta t \tag{2.54}$$

Naturally, the accuracy of this numerical integration method depends on the choice of timestep (Δt), where smaller timesteps improve accuracy. The basic sequence of steps an MD simulation are shown in Figure 2.7, where the loop exits at the desired final simulation time.

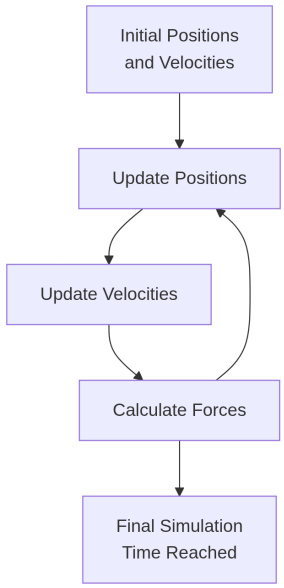

Figure 2.7: Typical sequence for MD simulations.

Prior to the extraction of observables from an MD trajectory, the system is typically equilibrated to make the kinetic and potential energy reach desired target values. However, certain phenomena require analysis of simulations that are not equilibrated, this is referred to as non-equilibrium molecular dynamics (NEMD). Frequently the topic of interest is how the system relaxes from the non-equilibrium state to an equilibrated state (*ie.* in VER studies), which is also done here in this thesis (see Chapter 6).

2.4.1 Microcanonical Ensemble

The microcanonical ensemble (NVE) describes a system that has constant number of particles (N), volume (V), and total energy (E). This ensemble is often used to study intrinsic properties of a system without external interactions. For instance, Figure 2.5 was produced from the analysis of an NVE simulation.

Within the NVE ensemble the total energy is conserved, the largest deviations in the total energy are correlated to the timestep of the simulation. Smaller timesteps allow for better energy conservation, because the numerical MD integrator produces more accurate trajectories. This relation is often also used to test newly developed or implemented potentials, by checking that the energy drift is reduced when the timestep is reduced. If the energy and forces in the potential are divergent, the energy drift will

not abide by this relation. In those cases the implementation of the potential needs to be debugged.

2.4.2 Canonical Ensemble

The canonical ensemble (NVT) describes a system that has constant number of particles (N), volume (V), and temperature (T). This ensemble is often used to study thermodynamic properties of a system at a specific temperature.

In order to maintain a constant temperature in an NVT simulations a "thermostat" is required. Thermostats are algorithms that regulate the temperature of the system, typically through scaling the velocities of the particles in the system. Careful consideration needs to be taken with the thermostat selection to avoid the so-called "flying ice cube" problem.[31,32] This issue is an atrifact of the velocity rescaling where high-frequency motions are drained into low-frequency, typically zero-frequency, motions like the translations and rotations of the whole system.

The Berendsen thermostat is one of the simplest thermostats, however, it is plagued by the flying ice cube problem. Regardless, the simplicity of the thermostat makes it perfect for explaining how thermostat algorithms work. The thermostat attempts to couple the temperature of the system to a heat bath,

$$\frac{dT}{dt} = \frac{1}{\tau}(T_0 - T(t)) \tag{2.55}$$

where T_0 is the bath temperature (the desired simulation temperature), $T(t)$ is the simulation temperature at time t, $\frac{dT}{dt}$ is the rate of change of the simulation temperature, and τ is a coupling parameter that describes the equilibration time according to which the Berendsen thermostat modifies the velocities. The temperature of the system is calculated by setting the total instantaneous kinetic energy of the system equal to the thermodynamic energy of the system and solving for temperature. This gives,

$$T = \frac{\sum_i^N m_i v_i^2}{3Nk_B} \tag{2.56}$$

where m_i is the mass of the ith particle, v_i the velocity of the ith particle, N the number of particles, and k_B the Boltzmann constant. The thermostat then rescales the velocities by the factor,

$$\lambda = \sqrt{1 + \frac{\Delta t}{\tau}(\frac{T_0}{T(t)} - 1)} \tag{2.57}$$

where Δt is the timestep. Although the Berendsen thermostat should not be used for studies, the concepts carry over to other more exact thermostats. Within the works in this thesis, the canonical velocity rescaling thermostat by Bussi *et al.*[33] is used instead.

2.A Bibliography

[1] Herman JC Berendsen, James PM Postma, Wilfred F van Gunsteren, and Jan Hermans. Interaction models for water in relation to protein hydration. In *Intermolecular forces: proceedings of the fourteenth Jerusalem symposium on quantum chemistry and biochemistry held in jerusalem, Israel, april 13–16, 1981*, pages 331–342. Springer, 1981.

[2] Herman JC Berendsen, J-Raúl Grigera, and Tjerk P Straatsma. The missing term in effective pair potentials. *Journal of Physical Chemistry*, 91(24):6269–6271, 1987.

[3] Kahled Toukan and Aneesur Rahman. Molecular-dynamics study of atomic motions in water. *Physical Review B*, 31(5):2643, 1985.

[4] William L Jorgensen, Jayaraman Chandrasekhar, Jeffry D Madura, Roger W Impey, and Michael L Klein. Comparison of simple potential functions for simulating liquid water. *The Journal of Chemical Physics*, 79(2):926–935, 1983.

[5] Christian J Burnham and Sotiris S Xantheas. Development of transferable interaction models for water. III. reparametrization of an all-atom polarizable rigid model (TTM2–R) from first principles. *The Journal of Chemical Physics*, 116(4): 1500–1510, 2002.

[6] Sotiris S Xantheas, Christian J Burnham, and Robert J Harrison. Development of transferable interaction models for water. II. accurate energetics of the first few water clusters from first principles. *The Journal of Chemical Physics*, 116(4): 1493–1499, 2002.

[7] Christian J Burnham and Sotiris S Xantheas. Development of transferable interaction models for water. IV. a flexible, all-atom polarizable potential (TTM2-F) based on geometry dependent charges derived from an ab initio monomer dipole moment surface. *The Journal of Chemical Physics*, 116(12):5115–5124, 2002.

[8] George S Fanourgakis and Sotiris S Xantheas. The flexible, polarizable, Thole-type interaction potential for water (TTM2-F) revisited. *The Journal of Physical Chemistry A*, 110(11):4100–4106, 2006.

[9] George S Fanourgakis and Sotiris S Xantheas. Development of transferable interaction potentials for water. V. extension of the flexible, polarizable, Thole-type model potential (TTM3-F, v. 3.0) to describe the vibrational spectra of water clusters and liquid water. *The Journal of Chemical Physics*, 128(7), 2008.

[10] CJ Burnham, DJ Anick, PK Mankoo, and GF Reiter. The vibrational proton potential in bulk liquid water and ice. *The Journal of Chemical Physics*, 128(15), 2008.

[11] Taisuke Hasegawa and Yoshitaka Tanimura. A polarizable water model for intramolecular and intermolecular vibrational spectroscopies. *The Journal of Physical Chemistry B*, 115(18):5545–5553, 2011.

[12] Pengyu Ren and Jay W Ponder. Polarizable atomic multipole water model for molecular mechanics simulation. *The Journal of Physical Chemistry B*, 107(24): 5933–5947, 2003.

[13] Pengyu Ren and Jay W Ponder. Temperature and pressure dependence of the AMOEBA water model. *The Journal of Physical Chemistry B*, 108(35):13427–13437, 2004.

[14] Jay W Ponder, Chuanjie Wu, Pengyu Ren, Vijay S Pande, John D Chodera, Michael J Schnieders, Imran Haque, David L Mobley, Daniel S Lambrecht, Robert A DiStasio Jr, *et al.* Current status of the AMOEBA polarizable force field. *The Journal of Physical Chemistry B*, 114(8):2549–2564, 2010.

[15] Lee-Ping Wang, Teresa Head-Gordon, Jay W Ponder, Pengyu Ren, John D Chodera, Peter K Eastman, Todd J Martinez, and Vijay S Pande. Systematic improvement of a classical molecular model of water. *The Journal of Physical Chemistry B*, 117(34):9956–9972, 2013.

[16] Chengwen Liu, Jean-Philip Piquemal, and Pengyu Ren. AMOEBA+ classical potential for modeling molecular interactions. *Journal of Chemical Theory and Computation*, 15(7):4122–4139, 2019.

[17] Chengwen Liu, Jean-Philip Piquemal, and Pengyu Ren. Implementation of geometry-dependent charge flux into the polarizable AMOEBA+ potential. *The Journal of Physical Chemistry Letters*, 11(2):419–426, 2019.

[18] Enrique Ricardo Batista. *Development of a new water-water interaction potential and application to molecular processes in ice*. University of Washington, 1999.

[19] K. T. Wikfeldt, E. R. Batista, F. D. Vila, and H. Jónsson. A transferable H_2O interaction potential based on a single center multipole expansion: SCME. *Phys. Chem. Chem. Phys.*, 15:16542–16556, 2013.

[20] Elvar Orn Jónsson, Asmus Ougaard Dohn, and Hannes Jonsson. Polarizable embedding with a transferable H_2O potential function I: formulation and tests on dimer. *Journal of Chemical Theory and Computation*, 15(12):6562–6577, 2019.

[21] Elvar Orn Jónsson, Soroush Rasti, Marta Galynska, Jorg Meyer, and Hannes Jónsson. Transferable potential function for flexible H_2O molecules based on the single-center multipole expansion. *Journal of Chemical Theory and Computation*, 18(12):7528–7543, 2022.

[22] Volodymyr Babin, Claude Leforestier, and Francesco Paesani. Development of a "first principles" water potential with flexible monomers: dimer potential energy surface, VRT spectrum, and second virial coefficient. *Journal of Chemical Theory and Computation*, 9(12):5395–5403, 2013.

[23] Volodymyr Babin, Gregory R Medders, and Francesco Paesani. Development of a "first principles" water potential with flexible monomers. II: trimer potential energy surface, third virial coefficient, and small clusters. *Journal of Chemical Theory and Computation*, 10(4):1599–1607, 2014.

[24] Gregory R Medders, Volodymyr Babin, and Francesco Paesani. Development of a "first-principles" water potential with flexible monomers. III. liquid phase properties. *Journal of Chemical Theory and Computation*, 10(8):2906–2910, 2014.

[25] Francesco Paesani. Getting the right answers for the right reasons: toward predictive molecular simulations of water with many-body potential energy functions. *Accounts of Chemical Research*, 49(9):1844–1851, 2016.

[26] Harry Partridge and David W Schwenke. The determination of an accurate isotope dependent potential energy surface for water from extensive ab initio cal-

culations and experimental data. *The Journal of Chemical Physics*, 106(11): 4618–4639, 1997.

[27] KT Tang and J Peter Toennies. An improved simple model for the van der waals potential based on universal damping functions for the dispersion coefficients. *The Journal of Chemical Physics*, 80(8):3726–3741, 1984.

[28] Jie Yang, Yi Ren, An-min Tian, and Huai Sun. COMPASS force field for 14 inorganic molecules, He, Ne, Ar, Kr, Xe, H_2, O_2, N_2, NO, CO, CO_2, NO_2, CS_2, and SO_2, in liquid phases. *The Journal of Physical Chemistry B*, 104(20):4951–4957, 2000.

[29] Marc C van Hemert, Junko Takahashi, and Ewine F van Dishoeck. Molecular dynamics study of the photodesorption of CO ice. *The Journal of Physical Chemistry A*, 119(24):6354–6369, 2015.

[30] Jun Chen, Jun Li, Joel M Bowman, and Hua Guo. Energy transfer between vibrationally excited carbon monoxide based on a highly accurate six-dimensional potential energy surface. *The Journal of Chemical Physics*, 153(5):054310, 2020.

[31] Stephen C Harvey, Robert K-Z Tan, and Thomas E Cheatham III. The flying ice cube: velocity rescaling in molecular dynamics leads to violation of energy equipartition. *Journal of computational chemistry*, 19(7):726–740, 1998.

[32] Efrem Braun, Seyed Mohamad Moosavi, and Berend Smit. Anomalous effects of velocity rescaling algorithms: the flying ice cube effect revisited. *Journal of chemical theory and computation*, 14(10):5262–5272, 2018.

[33] Giovanni Bussi, Davide Donadio, and Michele Parrinello. Canonical sampling through velocity rescaling. *The Journal of Chemical Physics*, 126(1):014101, 2007.

Chapter 3

YetAnotherSimulationSuite.jl: An Atomic Simulation suite in Julia

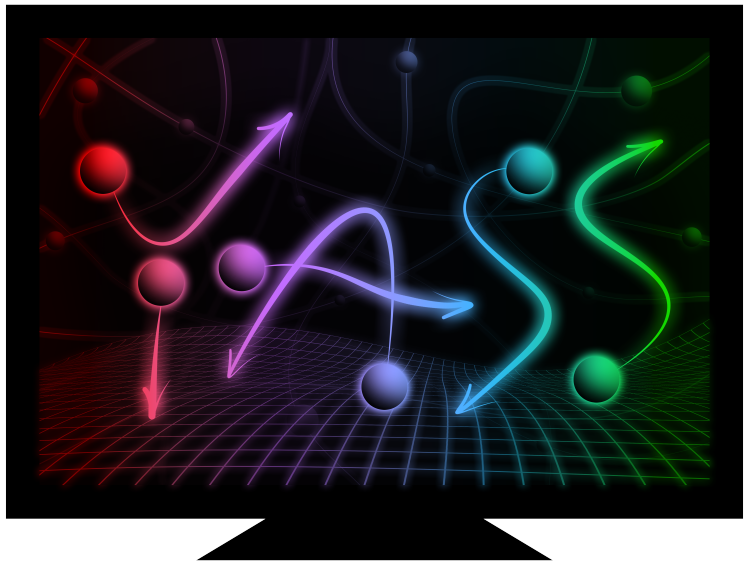

This chapter is based on:

Ferrari, B. C., "YetAnotherSimulationSuite.jl: An Atomic Simulation Suite in Julia." Journal of Open Source Software 10.116 (2025): 9480.

Open-Source Repository Software Documentation

Throughout the PhD I have continuously developed a simulation suite in the Julia [1] programming language. The initial development of this package began with the need to speed-up molecular dynamics (MD) simulations to make incredibly long timescale simulations accesible. Although a wide variety of simulation suites (hence the name) existed, including those focused on achieving the fastest speeds (*ie.* LAMMPS [2]), the perfect combination of speed, memory efficiency, flexibility and ease-of-use did not exist.

3.1 Features

In its current state, *YetAnotherSimulationSuite.jl* (YASS) offers a comprehensive set of capabilities for molecular simulations. It can perform geometry and cell optimizations, allowing users to find the most stable structures and lattice parameters for their systems. The suite supports molecular dynamics simulations in both the NVE (constant number of particles, volume, and energy) and NVT (constant number of particles, volume, and temperature) ensembles, enabling the study of system behavior under different thermodynamic conditions. YASS also provides tools for vibrational mode analysis using the harmonic approximation, which helps in understanding the vibrational properties of molecules. Additionally, it includes functionality for velocity autocorrelation function analysis, which is useful for extracting dynamic information such as the vibrational density of states beyond the harmonic approximation. The suite can compute radial and angular distribution functions, offering insights into the structural organization of particles within a system. Furthermore, YASS comes with several built-in potentials, including TIP4P/2005f [3], SPC-F [4], and two different CO–CO potentials from the literature, specifically those developed by van Hemert *et al.* [5] and Chen *et al.* [6]. These features make YASS a flexible and extensible tool for a wide range of molecular simulation tasks.

YASS was also developed with a focus on flexibility and extensibility, making it incredibly easy to add or customize anything within the package. Every part of the simulation suite, even down to the units used in the simulations, are left flexible and extensible to allow users to customize.

3.2 Installation

YASS can be installed using the Julia package manager via:

```
pkg> add YetAnotherSimulationSuite
```

If you are more adventerous, you can consider installing YASS from GitHub. This will get updates more frequently, which gives users more features but also comes with increased chances of bugs.

```
pkg> add https://github.com/Cavenfish/YetAnotherSimulationSuite.jl
```

The Julia package manager will handle all dependencies and YASS should work straight out of the box.

3.3 Benchmarks

Julia often delivers substantial performance gains over Python for numerical and scientific code because it is JIT-compiled, type-stable, and generates native LLVM code, so well-written Julia can approach C/Fortran speeds. However, that speed comes with trade-offs: just-in-time compilation (and package precompilation) introduces startup latency, and Julia's compilation artifacts and runtime can consume more memory than lightweight Python interpreters. In practice, Julia is most advantageous for long-running, compute-intensive workflows; for short scripts or very memory-constrained environments you should weigh the startup and memory overheads or use precompilation strategies to mitigate them. In the following, gold (Au) clusters are used throughout with a Leonard-Jones potential.

3.3.1 Geometry Optimization

Geometry optimizations using the LBFGS algorithm were performed on gold clusters containing 100, 500, 1000, and 5000 atoms. The results are shown in Table 3.1.

Table 3.1: Geometry optimization benchmark results for gold clusters.

Au Atoms	Iterations	YASS Time (s)	ASE Time (s)	YASS Speedup
100	1500	11.8	8.4	0.71x
500	1500	29.6	64.0	2.16x
1000	1500	108.7	218.8	2.01x

3.3.2 Harmonic Frequencies

Harmonic frequency calculations were performed on gold clusters containing 100, 500, and 1000 atoms. The results are shown in Table 3.2.

Table 3.2: Harmonic frequency calculation benchmark results for gold clusters.

Au Atoms	YASS Time (s)	ASE Time (s)	YASS Speedup
100	11.2	3.3	0.29x
500	22.7	89.8	3.95x
1000	87.1	490.8	5.63x

3.3.3 Molecular Dynamics

Molecular dynamics simulations were performed on gold clusters containing 100, 500, and 1000 atoms for 1000, 2000 and 5000 time steps. The results are shown in Table 3.3.

Table 3.3: Molecular dynamics simulation benchmark results for gold clusters.

Au Atoms	Time Steps	YASS Time (s)	ASE Time (s)	YASS Speedup
100	1000	15.8	4.8	0.30x
100	2000	16.1	9.3	0.58x
100	5000	16.6	22.4	1.35x
500	1000	21.9	32.3	1.47x
500	2000	27.7	65.9	2.38x
500	5000	44.2	160.7	3.63x
1000	1000	35.6	79.4	2.23x
1000	2000	55.9	165.3	2.95x
1000	5000	112.5	406.1	3.61x
1000	15000	315.3	1332.8	4.22x

3.4 Memory Considerations

Currently, YASS has a roughly 1 GB memory overhead due to dependencies, buffer allocations, and compilation artifacts. This overhead is typical for Julia packages with similar functionality, but may be significant for users with limited memory resources. This overhead is static and does not scale with system size, so larger simulations will see a smaller relative impact. Future optimizations may reduce this overhead.

3.4.1 Geometry Optimization

Table 3.4: Memory usage for geometry optimization benchmarks.

Au Atoms	Iterations	Memory Usage (GB)
100	1500	1.06
500	1500	1.06
1000	1500	1.06

3.4.2 Harmonic Frequency Calculation

Table 3.5: Memory usage for harmonic frequency calculation benchmarks.

Au Atoms	Memory Usage (GB)
100	1.07
500	1.16
1000	1.41

3.4.3 Molecular Dynamics Simulation

Table 3.6: Memory usage for molecular dynamics simulation benchmarks.

Au Atoms	Time Steps	Memory Usage (GB)
100	1000	1.12
500	1000	1.15
1000	1000	1.19
5000	1000	1.55

3.5 Examples

A basic example of optimizing the geometry of a molecule in YASS:

```
using Optim
using YetAnotherSimulationSuite

# Read initial structure
water = readSystem("water.xyz")

# Run geometry optimization
optimized = opt(TIP4Pf(), LBFGS(), water)
```

```
# Save optimized structure
write("optimized.xyz", optimized)
```

Additional optional optimization criteria can be passed to the *opt* function (more on that in the YASS documentation). After optimizing the geometry its easy to calculate the harmonic normal modes of the molecule in YASS.

```
# Calculate frequencies and normal modes
freqs, modes = getHarmonicFreqs(TIP4Pf(), optimized)
```

If anharmonicity is desired, YASS can also be used to calculate the vibrational density of states (VDOS) through the velocity autocorrelation function (VACF). This method captures anharmonicity in the vibrational modes.

```
using YetAnotherSimulationSuite

# Read initial structure
water = readSystem("water.xyz")

# Run 5 picosecond simulation with 0.1 fs timestep
traj = run(TIP4Pf(), water, 5u"ps", 0.1u"fs", NVE())

# You can also specify the start time
traj = run(TIP4Pf(), water, (5u"ps", 10u"ps"), 0.1u"fs", NVE())

# Extract velocities and masses
vel, mas = getVelMas(traj)

# Configure VACF calculation
inp = vacfInps(
  vel,        # Velocity trajectories
  mas,        # Atomic masses
  1e15u"Hz", # Sampling frequency (1/fs = 1e15 Hz)
  true,       # Normalize VACF
  Hann,       # Window function
  4,          # FFT padding factor
  true        # Mirror the data
)

# Calculate VDOS
out = VDOS(inp)
```

3.A Bibliography

[1] Jeff Bezanson, Alan Edelman, Stefan Karpinski, and Viral B Shah. Julia: A fresh approach to numerical computing. *SIAM Review*, 59(1):65–98, 2017.

[2] Aidan P Thompson, H Metin Aktulga, Richard Berger, Dan S Bolintineanu, W Michael Brown, Paul S Crozier, Pieter J In't Veld, Axel Kohlmeyer, Stan G Moore, Trung Dac Nguyen, *et al.* Lammps-a flexible simulation tool for particle-based materials modeling at the atomic, meso, and continuum scales. *Computer Physics Communications*, 271:108171, 2022.

[3] Miguel A González and José LF Abascal. A flexible model for water based on TIP4P/2005. *The Journal of Chemical Physics*, 135(22), 2011.

[4] Kahled Toukan and Aneesur Rahman. Molecular-dynamics study of atomic motions in water. *Physical Review B*, 31(5):2643, 1985.

[5] Marc C van Hemert, Junko Takahashi, and Ewine F van Dishoeck. Molecular dynamics study of the photodesorption of CO ice. *The Journal of Physical Chemistry A*, 119(24):6354–6369, 2015.

[6] Jun Chen, Jun Li, Joel M Bowman, and Hua Guo. Energy transfer between vibrationally excited carbon monoxide based on a highly accurate six-dimensional potential energy surface. *The Journal of Chemical Physics*, 153(5):054310, 2020.

Chapter 4

Abundance of Exceptionally Strong Binding Sites for H_2O Adsorption on the Ice Ih(0001) Surface

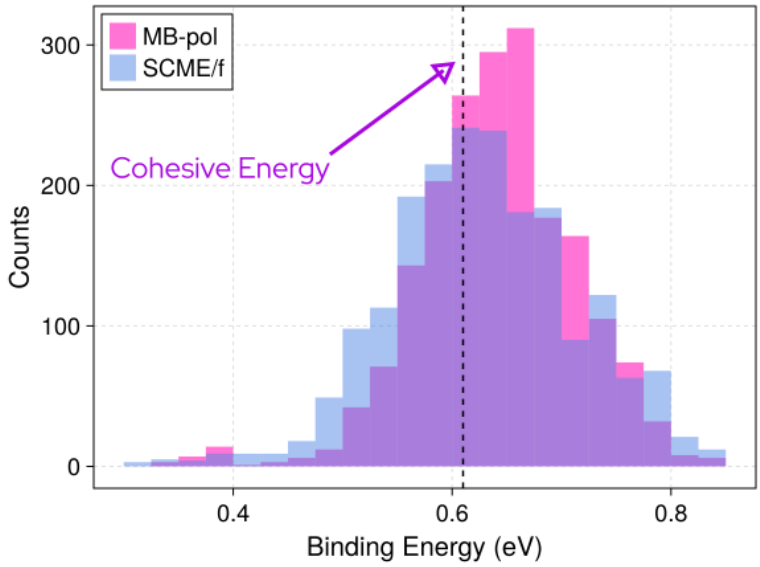

This chapter is based on:

Ferrari, B. C., Sallermann, M., Jónsson, E. O., Jónsson, H., & Meyer, J. (2026). Abundance of Exceptionally Strong Binding Sites for H_2O Adsorption on the Ice Ih(0001) Surface, *in prep.*

4.1 Abstract

The adsorption of water molecules on ice surfaces is of significant importance in many respects, in particular for gaining a deeper understanding of ice crystal growth. Due to the proton disorder on the ice Ih(0001) surface there is a wide distribution for the binding energy of admolecules. Previous calculations using simple point-charge force fields have indicated that it can even exceed the cohesive energy of the crystal at certain sites. While the accuracy of those calculations has been contested by some subsequent density functional theory calculations and direct measurement of these binding energy remains elusive, the possibility of such strong binding sites has been associated with various experimental observations and would significantly influence the growth mode of the crystal. Here, we study the adsorption of a water molecule on the ice Ih(0001) surface using recently developed polarizable many-body interaction potential functions, and find remarkably abundant sites with binding energy larger than the cohesive energy, dominated by electrostatics. Furthermore, we show how the local environment at the binding site affects the binding energy and propose a descriptor that serves as a predictor for the binding energy at a given site.

4.2 Introduction

Ice is one of the most widely studied substances, yet a plethora of its physicochemical properties remain poorly understood. One such property is the adsorption of water molecules on an ice surface. Deciphering the mechanisms behind this process is paramount to understanding ice growth, which plays a critical role in global climate [1,2], as well as other atmospheric phenomena [3]. Under ambient conditions ice is found in its hexagonal (Ih) phase, which is well known to have a proton disordered bulk structure. [4] The degree of proton ordering in the surface is still debated, namely due to technical limitations for experimental observations of the ice surface. The lowest energy surface is the Fletcher striped phase, where the dangling OHs are arranged in lines across the surface. [5] This surface structure was initially predicted by theoretical calculations, and later helium diffraction experiments [6] were interpreted [7] as indicating proton ordering on the surface. This interpretation was eventually brought into question [8]; however, recent novel experimental studies [9] have claimed to verify this proton ordered surface. Although this is the lowest energy surface and claims of its experimental verification have been made, it is still not widely accepted. As such, the true nature of the ice Ih surface is still in question, leaving the possibility of either ordered or disordered

surfaces. The surface structure, specifically the local environment at the binding site, will naturally play a major role in the adsorption of water molecules on the surface.

Batista and Jónsson [10] calculated binding energies of water molecules on the basal plane surface of an ice Ih crystal using the TIP4P potential. They found that 4% of the binding sites had binding energies stronger than the cohesive energy of the crystal. They further studied island formation and diffusion untangling the implications of these strong binding sites on the crystal growth. A later study reproduced their results for a proton disordered ice Ih surface, and went further by calculating the binding energy distribution for a proton ordered surface. [11] On average they found the proton ordered surface to produce smaller binding energies, however, there was still a small percentage above the cohesive energy. Thierfelder *et al.* [12] performed a follow-up study on the binding energy of water molecules on the basal surface of ice Ih using the PW91 [13] densityfunctional. Contrary to the previous findings, they did not find any binding sites with binding energies larger than the cohesive energy. Shortly after, Sun *et al.* [14] showed that the binding energy of water on the ice Ih basal surface depended on the so-called "order parameter". This order parameter is defined as,

$$C_{OH} = \frac{1}{N_{OH}} \sum_{i=1}^{N_{OH}} c_i \tag{4.1}$$

where N_{OH} is the total number of dangling OH bonds on the surface, and c_i is the number of nearest neighbor dangling OH bonds around the ith dangling OH bond. This global order parameter is a measure of the degree of ordering of the dangling OH groups on the surface of the ice. They revealed that surfaces with larger order parameters (more proton disorder) produced larger binding energies. Moreover, for surfaces with order parameters less than 2.5 no binding sites were stronger than the cohesive energy. Bringing forth the notion that the two previous studies found contradictory results simply because they used surfaces with different degrees of proton ordering. Despite these studies, the possibility of a water molecule having a binding energy larger than the cohesive energy is still contested.

Although contested, these strong binding sites have been speculated to be the cause of multiple abnormalities observed in experiments. Nordlund *et al.* [15] studied the surface of thin ice Ih films grown on Pt(111) with x-ray absorption spectroscopy, where they found an abundance of isotropically distributed dangling OHs. In particular, they found more dangling OHs than is expected for a bilayer terminated proton disordered ice Ih surface, implying a non-bilayer termination. They speculated this could be due

to water admolecules bound on these strong binding sites where annealing would not remove them from the surface. Similarly, Mehlhorn and Morgenstern [16] found that ice Ih grown on Cu(111) had no indication of a terminating bilayer at any annealing temperatures. They concluded this after observing bright spots in the STM that could not be removed by annealing, which they speculated were water admolecules at strong binding sites on the ice surface. More recently, Bockstedte *et al.* [17] used a combination of theory and experiment to show that for thin ice films grown on Cu(111) the basal surface of ice Ih was terminated by admolecule clusters. After experimentally observing a lack of a terminating bilayer, they performed DFT calculations. They found no strong binding sites for admolecules, leading them to conclude the surface must be terminated by clusters of admolecules. To better understand these experiments it is imperative that we have a comprehensive understanding of water binding on the basal surface of ice Ih.

Beyond reconciling the unexplained experimental observations, the existence of these strong binding sites would mean that ice Ih does not follow the standard growth model. A natural consequence of this is that a pristine ice surface is not possible, since annealing an admolecule at a strong binding site would result in surface melting. In order to better understand the validity of these strong binding sites, we have performed an exhaustive investigation into the binding energy of the water monomer on the basal surface of ice Ih. We employed two highly sophisticated many-body potentials, the flexible Single-Center Multipole Expansion (SCME/f) [18–21] and MB-pol [22–25], to study the adsorption of water monomers on the basal surface of ice Ih. We show that for all surfaces studied herein a site is found with binding energy larger than the cohesive energy. Furthermore, we decompose the binding energy to show the importance of dispersion in the adsorption. We also expand out the multipole contributions to the binding energy and show how quadrupole moments are significant. Finally, we show how the local environment influences the binding energy. Taking inspiration from this analysis we propose a more local "order parameter", which is more strongly correlated with the binding energy.

4.3 Methods

Orthogonal bulk cells of ice Ih containing 432 H_2O molecules with lattice parameters optimized for each potential (see Appendix) have been the starting points for constructing surface slab models. Using the ice Ih generation algorithm in the GenIce [26] program, 26 differently proton disordered 3x3x3 supercells have been created. Adding

60 Å of vacuum along the (0001) direction has then resulted in 26 pristine ice Ih(0001) surface slab models. The geometries of these slab models were optimized while keeping the atoms in the bottom half fixed at the bulk geometry positions.

For each slab, 75 random sites were selected on the surface and an H_2O admolecule was placed there and the geometry of the full system was optimized, again maintaining the bottom half of the slab fixed. The binding energies have been calculated using Equation (4.2). Consistent with previous works, the calculated binding energies have not been corrected for zero-point energies.

$$E_{BE} = E_{\text{slab}} - E_{\text{system}} \tag{4.2}$$

Contour lines for distances from dangling OHs were made by using a kernel density estimation, where Gaussians with 1.5 Å width in both dimensions were applied to each dangling OH site.

All geometry optimizations were done by first running 50 iterations of the OACCEL[27] optimizer, followed by running the conjugate gradient (CG)[28,29] method until convergence. The convergence criteria for CG geometry optimizations was always (unless stated otherwise) set to 1×10^{-5} eV/Å on the gradient norm. Lattice optimizations were done by cycling between cell optimizations with fixed scaled positions, and geometry optimizations with fixed cell vectors. Cell optimizations were run using only the CG optimizer with a convergence criteria of 1×10^{-8} eV/Å on the gradient norm. Full convergence was determined when the average change of the lattice vectors was less than 1×10^{-3} Å.

All calculations, data analysis and plotting were done using the Julia (version 1.11.6) programming language[30]. *YetAnotherSimulationSuite.jl* (YASS)[31] was used for all calculations, and it is backed by a variety of Julia packages; *Optim.jl*[32] (version 1.12.0) is used for geometry and cell optimizations, Chemfiles[33] (the *Chemfiles.jl* Julia wrapper) is used for reading and writing xyz files, and *JLD2.jl*[34] is used for storing data structures in HDF5 compliant format. Additionally, *DataFrames.jl*[35] was used during data analysis, and *Makie.jl*[36] (subpackage *CairoMakie.jl* version 0.15.4) was used for plotting. A Julia wrapper of the MBX[37] software was used to calculate MB-pol[22–25] forces and energies. Similarly, the C++ SCME/f[18–21] potential was wrapped and integrated into the Julia workflow. Proton disordered ice structures were generated using the GenIce[26] software.

4.4 Results and Discussion

We calculated the binding energy for 75 randomly selected sites across 26 surfaces with different degrees of dangling OH ordering, with C_{OH} ranging from 2 to ≈ 3.5. Figure 4.1 shows two example surfaces, one proton disordered (leftmost) and the other proton ordered (rightmost). The influence of the local environment on the binding energy can be seen within the figure. The leftmost panels show examples of a proton disordered surface, whereas the rightmost panels show a proton ordered (Fletcher-striped) surface. These plots show that although 75 sites are sampled, the results are not 75 different binding sites. This is a result of the attractive force of the dangling OHs, as can be seen by most binding sites being near dangling OHs. Sampled sites far from dangling OHs resulted in the admolecule moving to another location during the geometry optimization.

Figure 4.2 shows the binding energy distributions for each potential plotted versus the order parameter of the surface. For both potentials the distributions become broader as the order parameter increases, as expected with the increased variation in sites on the surface. In agreement with previous studies, as the order parameter increases the average binding energy for each potential also increases. Contrary to previous DFT-based studies, we find that for all surfaces studied at least one site has a binding energy larger than the cohesive energy. Across all surfaces SCME/f finds roughly 50% of sites to be one of these strong binding sites, and MB-pol finds roughly 63%.

On 25 different surfaces with order parameter of 2.0, both potentials produce at least one strong binding site (see Appendix). Moreover, for these surfaces both potentials produce an abundance of strong binding sites: for SCME/f roughly 40% of sites bind stronger than the cohesive energy and for MB-pol roughly 65%. These percentages are nearly identical to those we found for surfaces with varied order parameters, indicating a strong tendency for strong binding. Further supporting the notion that even highly ordered surfaces can produce these strong binding sites.

Additional analysis (found in the Appendix) revealed that the binding energy was strongly correlated with the induced dipole moment of the admolecule, in agreement with previous work[14]. We also find that the binding energy is closely correlated to the shortest hydrogen bond length formed between the admolecule and the surface. It is well known that DFT struggles to produce accurate descriptions of hydrogen bonds[38,39], which at first glance may seem to explain the discrepancy between our results and previous DFT-based results. However, PBE is reported to overbind hydro-

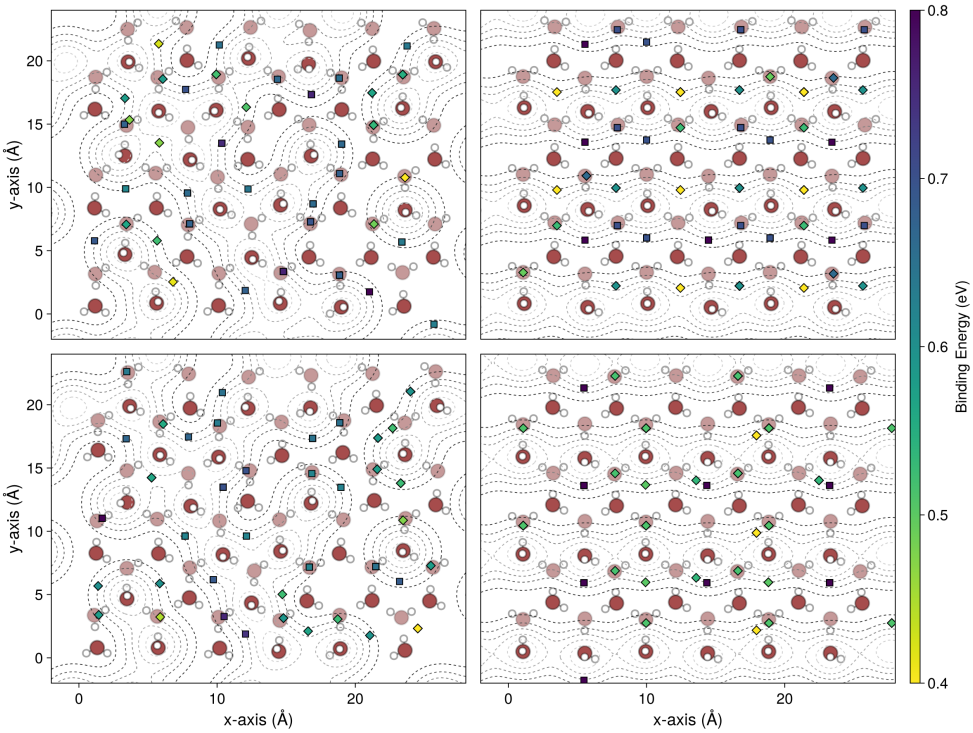

Figure 4.1: A visualization of the influence of the local environment on the binding energy. The surface bilayer is shown in reduced opacity, where red is oxygen atoms, white are hydrogen atoms. The lower layer of the bilayer is less opaque than the upper layer. The contour lines represent distance from a dangling OH, where lighter dashed lines are closer and darker dashed lines farther away from dangling OHs. The scatter points are binding sites, where the color corresponds to the binding energy for that site (as shown by the colorscale) and the marker denotes if the binding energy is above (rectangle) or below (diamond) the cohesive energy of ice Ih for the respective potential. The top panels are calculated with MB-pol and the lower panels with SCME/f. The leftmost panels are disordered surfaces, and the rightmost panels are Fletcher-striped surfaces.

gen bonds when compared to CCSD(T)[40], which both potentials are fitted to. This raises the question of what could be causing this discrepancy.

To analyze the adsorption energies in more detail we decomposed the binding energy into its constituent components within each potential. The top panels of Figure 4.3 shows the binding energies from both potentials decomposed into their constituent energy contributions. Both potentials exhibit similar decomposed contributions, namely, the electrostatic and dispersion terms have averages in very close agreement. As expected, the electrostatic contribution is the largest contribution to

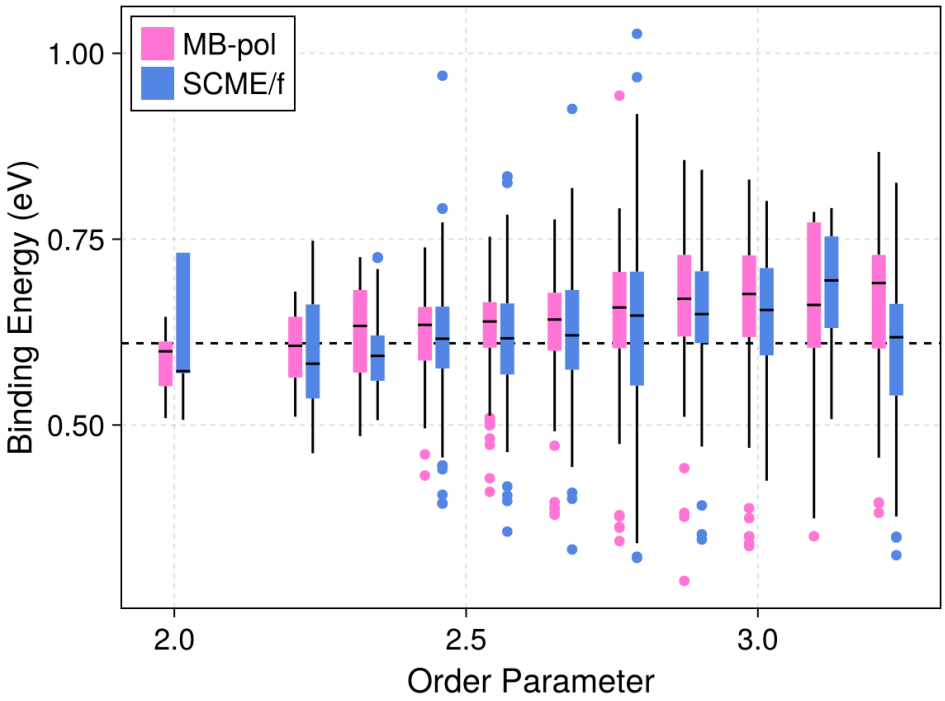

Figure 4.2: Binding energy plotted as a function of the order parameter (C_{OH}) defined in Equation (4.1). For visual clarity, MB-pol and SCME/f have artificial offsets in the x-axis. All 1950 binding sites for each potential are included. The black dashed line is the experimental cohesive energy (0.609 eV), which is close to the cohesive energy produced by MB-pol (0.608 eV) and SCME/f (0.611 eV).

the binding energy. The second largest positive contribution in both potentials is dispersion, with a contribution nearly half as large as the electrostatic contribution.

The electrostatics in both potentials can be further decomposed into multipole contributions, of which there is notably more terms included within SCME/f than in MB-pol. As such, we have decomposed the multi-pole contributions to the binding energy for SCME/f only. The bottom panel of Figure 4.3 shows the contribution of dipole, quadrupole, octupole and hexadecapole terms to the electrostatic component of the binding energy for SCME/f. As expected, the dipole term is the largest and higher order terms contribute less as the order increases. Interestingly, the quadrupole term has an average energy contribution close to that of the dipole term. This shows that for adsorption both dipole and quadrupole moments play a significant role in the energetics.

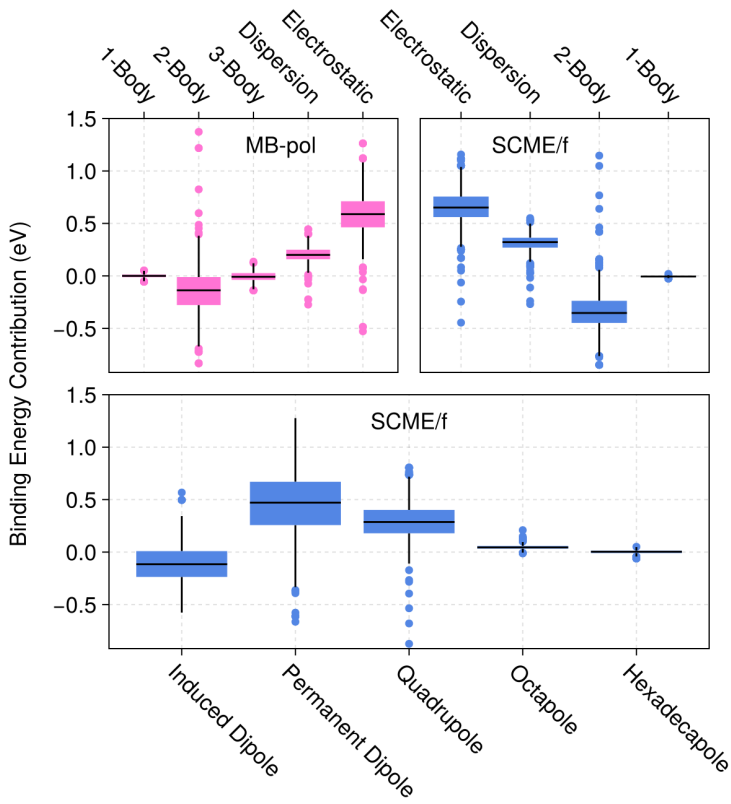

Figure 4.3: Top panels: decomposed binding energy contributions for each potential. All 1950 binding sites for each potential are included. Bottom panel: decomposed electrostatic energy contributions to the binding energy using SCME/f. All 1950 binding sites for each potential are included.

A key feature of the binding highlighted by Figure 4.1 is the importance of the alignment of the dangling OH with the oxygen atom of the admolecule. In particular, the strongest binding sites are those where the H-bond formed by the dangling OH and the admolecule is closest to being linear. This is corroborated by the trend observed between the shortest H-bond and binding energy, namely because a linear H-bond will be a shorter H-bond. For instance, looking at A-type sites in the top right panel of Figure 4.1 the energies alternate between 0.63 eV and 0.61 eV. The key difference between these sites is the direction of the in-surface H-bond formed by the molecule with the dangling OH near the binding site. The direction of this H-bond dictates how well the water molecule can align its dangling OH with the oxygen atom of the

admolecule. Rotations around the H-bond axis allow the dangling OH to pivot toward the admolecule, as such, the weakest A-type sites are those where the H-bond points away from the binding site. These sites prevent rotations that align the dangling OH, in order to compensate for this these sites result in larger H−O−H bond angles for the molecule with the dangling OH. However, limitations on the bond angle prevent the dangling OH from making an ideal alignment, resulting in smaller binding energies. This effect is more pronounced in MB-pol, where the H−O−H bond angle flexibility due to environment is larger (see Appendix). Moreover, the change in the H−O−H bond angle for molecules with dangling OHs near a binding site before and after binding is larger for MB-pol than SCME/f (see Appendix). This bond angle flexibility in MB-pol causes the binding energy distributions to be narrower than those calculated with SCME/f.

Although the binding energy is correlated in some ways to the order parameter, there is still a large variation in binding sites per order parameter (see Figure 4.2). This is due to the order parameter being insensitive to the local environment at the adsorption site, which plays the dominant role in the binding energy (see Figure 4.1). Drawing inspiration from the analysis we have done, we have constructed a "local environment parameter",

$$C = \sum_{i}^{NN} \frac{\pi - (0.5\pi - \theta_i)^3}{r_i^3} + \sum_{i}^{N} \frac{1}{r_i^3} \tag{4.3}$$

where NN is the number of dangling OHs within 4 Å from the adsorption site, N is the number of dangling OHs further than 4 Å from the adsorption site, r is the distance from the dangling OH, and θ is the angle formed between the site, dangling OH, and the additional hydrogen atom on the surface molecule with the dangling OH. The angle is used to account for how rotations around the H-bond axis allow for the dangling OH to better align with the admolecule.

Figure 4.4 shows the binding energies as a function of the local environment parameter using both potentials, separately for both A-type and B-type adsorption sites. A clear trend is observed where increasing the local environment parameter increases the binding energy. This gives a more robust predictor of how what the binding energy for a site on a surface will be.

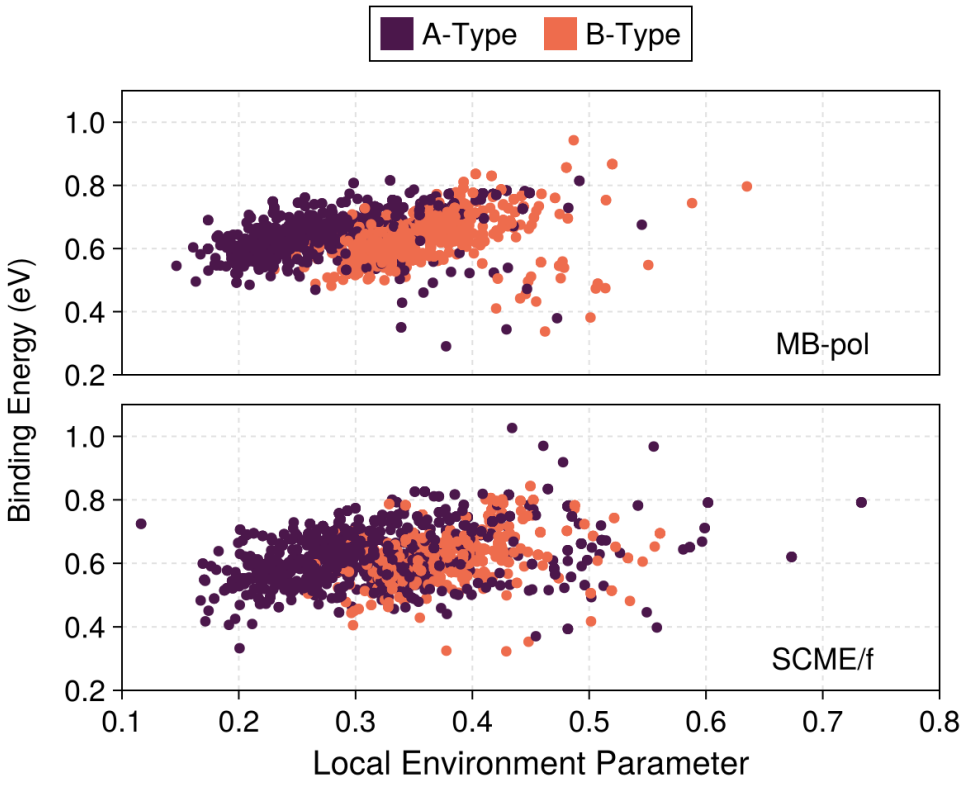

Figure 4.4: Binding energy as a function of the local environment parameter.

4.5 Conclusion

We have done an exhaustive analysis of the physicochemical properties involved in the adsorption of water monomers on the basal surface of ice Ih. Utilizing highly sophisticated potentials we have shown that binding sites with energies larger than the cohesive energy can be found on surfaces with any degree of proton ordering. We have also revealed that the dominant term in the binding is the electrostatic term, where the dipole and quadrupole terms are significant contributors to the binding energy. Additionally, we show that dispersive interactions also contribute significantly to the adsorption process. Furthermore, we show that the local environment is crucial to the binding, and cannot be simply reduced down to distances from dangling OHs or degree of surface ordering. Finally, we have constructed a local environment parameter

which serves as an improved descriptor for how slab structure will influence binding energies.

Our results have significant implications for ice surface growth, meaning that a pristine ice Ih surface is not possible. This has implications for various atmospheric phenomena, which are vital to global climate studies. Furthermore, the confirmation of the existence of these strong binding sites helps shine light on many unexplained experimental observations, specifically those that observed a non-bilayer-terminated ice surface.

4.A Appendix

4.A.1 Optimized Lattice Vectors and Cohesive Energy

Table 4.A.1 compiles the optimized lattice vectors and cohesive energies of the bulk phase ice Ih structures calculated by each potential.

Table 4.A.1: Lattice parameters a and c (Å) and cohesive energies (meV) of bulk ice Ih, calculated for each potential.

Potential	a	c	E_{coh}
Expt [41,42]	8.98	7.33	-609
MB-pol	8.935	7.284	-607.5
SCME/f	8.889	7.239	-611.4

4.A.2 Order Paremeter 2.0 Surfaces

Figure 4.A.5 shows the binding energy distributions with both potentials for 25 surfaces with order parameter 2. This set of 25 surfaces contains Fletcher striped surfaces and glide surfaces, both of which have order parameter 2.

4.A.3 Binding Energy Correlations

Figure 4.A.6 shows the correlation between the induced dipole moment of the admolecule and the binding energy. This contains all data from all binding sites across all surfaces studied herein.

Figure 4.A.7 shows the correlation between the shortest hydrogen bond formed between the admolecule and the surface and the binding energy. This also contains all data from all binding sites across all surfaces studied herein.

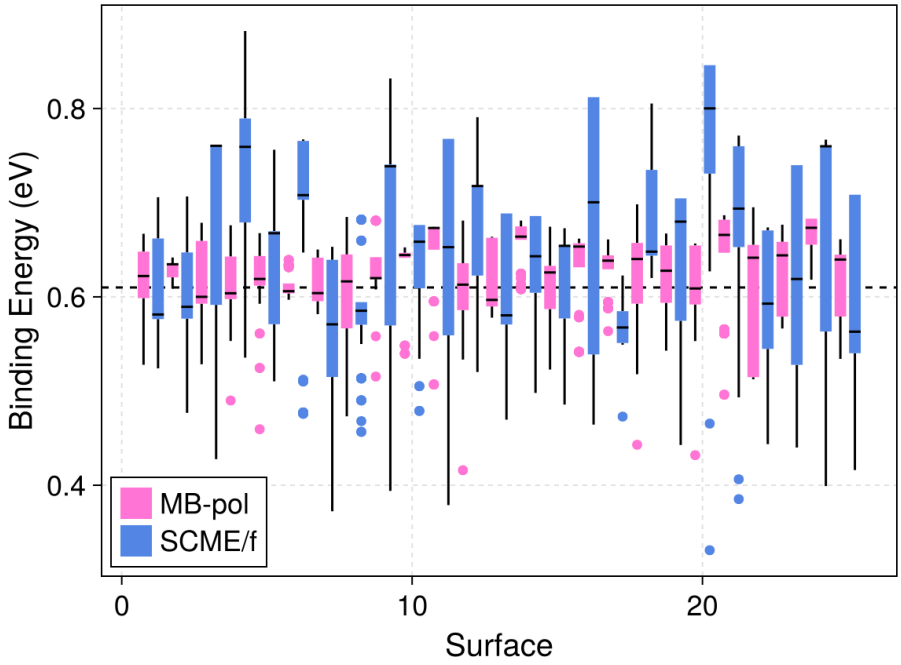

Figure 4.A.5: Binding energy distributions for surfaces with order parameter 2.

4.A.4 Bond Angle Analysis

Figure 4.A.8 shows the distribution of water bond angles for molecules within the bulk and surface bilayer using both potentials. This contains data from all slabs used herein.

Figure 4.A.9 shows the distribution of the difference between the water bond angle of a molecule with a dangling OH before and after binding. This contains data from all slabs used herein.

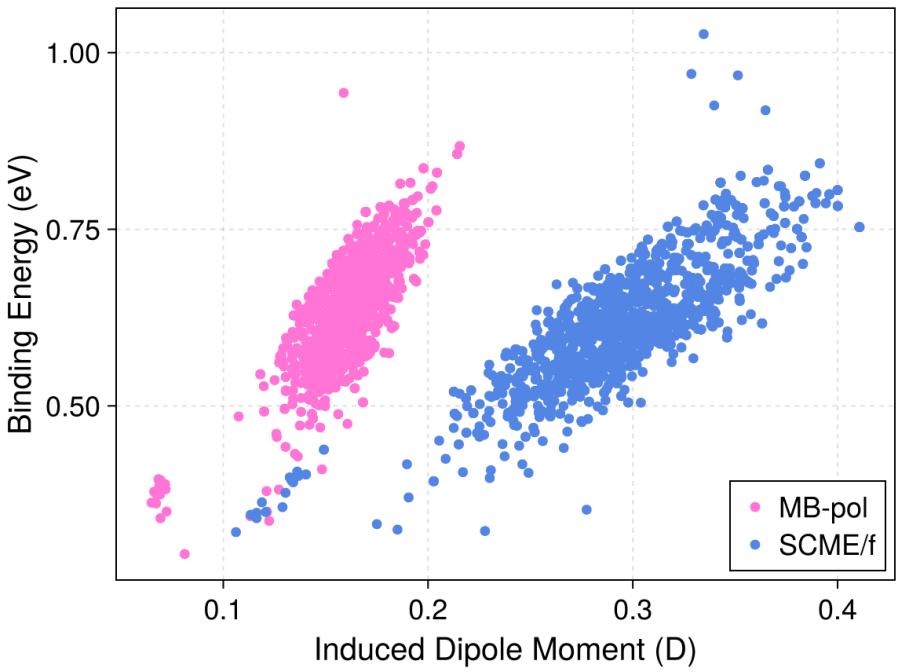

Figure 4.A.6: Binding energy versus the induced dipole moment of the admolecule.

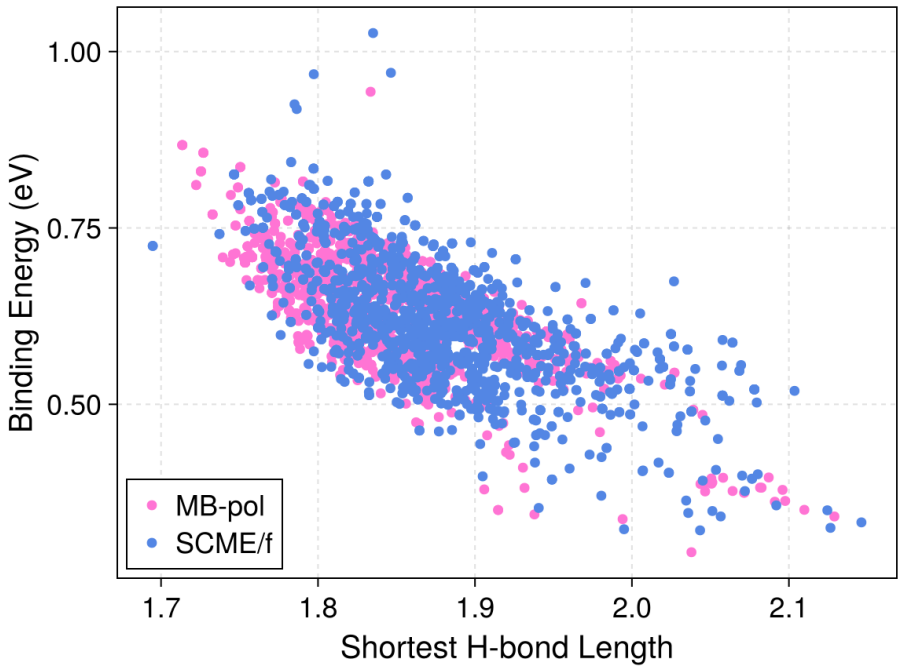

Figure 4.A.7: Binding energy versus shortest hydrogen bond formed between the adsorbate molecule and the surface.

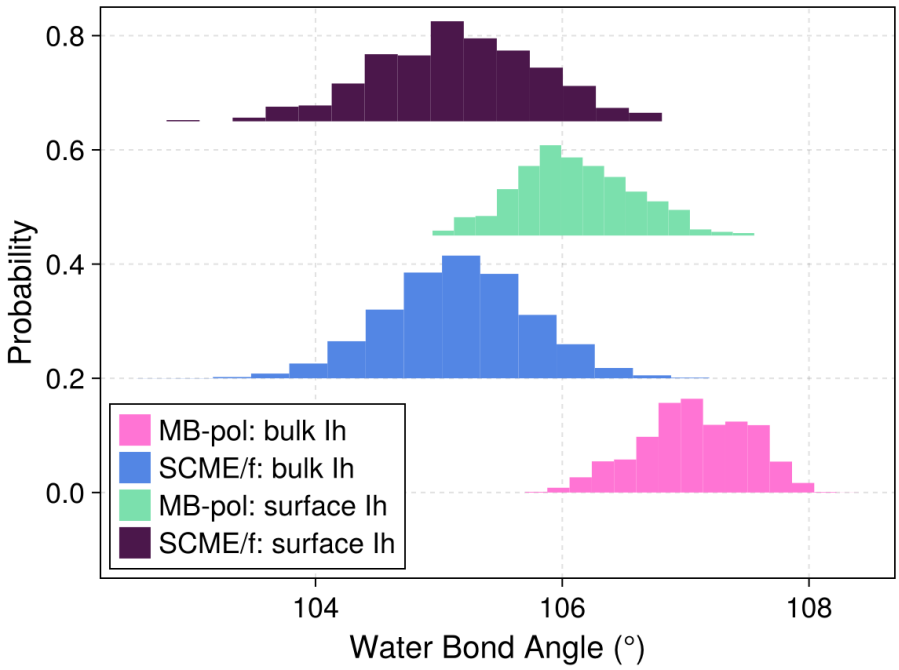

Figure 4.A.8: The distribution of water bond angles for bulk phase structures, and surface bilayer molecules in slab structures with MB-pol and SCME/f.

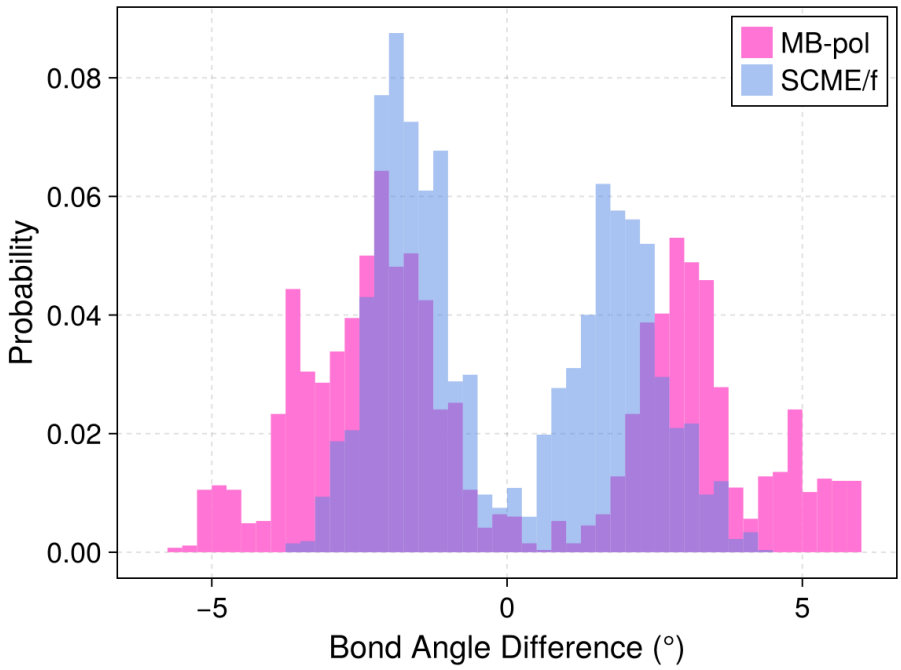

Figure 4.A.9: The difference in the H−O−H bond anlge of the water molecules with dangling OHs near binding sites before and after binding.

4.B Bibliography

[1] Petr G Sennikov, Stanislav K Ignatov, and Otto Schrems. Complexes and clusters of water relevant to atmospheric chemistry: H2o complexes with oxidants. *ChemPhysChem*, 6(3):392–412, 2005.

[2] Trude Storelvmo. Aerosol effects on climate via mixed-phase and ice clouds. *Annual Review of Earth and Planetary Sciences*, 45(1):199–222, 2017.

[3] Jonathan PD Abbatt. Interactions of atmospheric trace gases with ice surfaces: Adsorption and reaction. *Chemical Reviews*, 103(12):4783–4800, 2003.

[4] Victor F Petrenko and Robert W Whitworth. *Physics of ice*. OUP Oxford, 1999.

[5] Neville H Fletcher. Reconstruction of ice crystal surfaces at low temperatures. *Philosophical Magazine B*, 66(1):109–115, 1992.

[6] A Glebov, AP Graham, A Menzel, JP Toennies, and P Senet. A helium atom scattering study of the structure and phonon dynamics of the ice surface. *The Journal of Chemical Physics*, 112(24):11011–11022, 2000.

[7] V Buch, H Groenzin, I Li, MJ Shultz, and E Tosatti. Proton order in the ice crystal surface. *Proceedings of the National Academy of Sciences*, 105(16):5969–5974, 2008.

[8] N Avidor and W Allison. Helium diffraction as a probe of structure and proton order on model ice surfaces. *The Journal of Physical Chemistry Letters*, 7(22): 4520–4523, 2016.

[9] Yuki Nojima, Yudai Suzuki, Misato Takahashi, and Shoichi Yamaguchi. Proton order toward the surface of ice ih revealed by heterodyne-detected sum frequency generation spectroscopy. *The Journal of Physical Chemistry Letters*, 8(20):5031–5034, 2017.

[10] Enrique R Batista and Hannes Jónsson. Diffusion and island formation on the ice ih basal plane surface. *Computational Materials Science*, 20(3-4):325–336, 2001.

[11] Andreas Pedersen, Leendertjan Karssemeijer, Herma M Cuppen, and Hannes Jónsson. Long-time-scale simulations of h2o admolecule diffusion on ice ih (0001) surfaces. *The Journal of Physical Chemistry C*, 119(29):16528–16536, 2015.

[12] C Thierfelder, A Hermann, P Schwerdtfeger, and WG Schmidt. Strongly bonded water monomers on the ice ih basal plane: Density-functional calculations. *Physical Review B—Condensed Matter and Materials Physics*, 74(4):045422, 2006.

[13] John P Perdew and Yue Wang. Accurate and simple analytic representation of the electron-gas correlation energy. *Physical Review B*, 45(23):13244, 1992.

[14] Zhaoru Sun, Ding Pan, Limei Xu, and Enge Wang. Role of proton ordering in adsorption preference of polar molecule on ice surface. *Proceedings of the National Academy of Sciences*, 109(33):13177–13181, 2012.

[15] D Nordlund, H Ogasawara, Ph Wernet, M Nyberg, M Odelius, LGM Pettersson, and A Nilsson. Surface structure of thin ice films. *Chemical Physics Letters*, 395 (1-3):161–165, 2004.

[16] Michael Mehlhorn and Karina Morgenstern. Faceting during the transformation of amorphous to crystalline ice. *Physical Review Letters*, 99(24):246101, 2007.

[17] Michel Bockstedte, Anja Michl, Manuel Kolb, Michael Mehlhorn, and Karina Morgenstern. Incomplete bilayer termination of the ice (0001) surface. *The Journal of Physical Chemistry C*, 120(2):1097–1109, 2016.

[18] Enrique Ricardo Batista. *Development of a new water-water interaction potential and application to molecular processes in ice*. University of Washington, 1999.

[19] Kjartan Thor Wikfeldt, ER Batista, FD Vila, and H Jónsson. A transferable h 2 o interaction potential based on a single center multipole expansion: Scme. *Physical Chemistry Chemical Physics*, 15(39):16542–16556, 2013.

[20] Elvar Orn Jonsson, Asmus Ougaard Dohn, and Hannes Jonsson. Polarizable embedding with a transferable h2o potential function i: Formulation and tests on dimer. *Journal of Chemical Theory and Computation*, 15(12):6562–6577, 2019.

[21] Elvar Orn Jonsson, Soroush Rasti, Marta Galynska, Jorg Meyer, and Hannes Jónsson. Transferable potential function for flexible h2o molecules based on the single-center multipole expansion. *Journal of Chemical Theory and Computation*, 18(12):7528–7543, 2022.

[22] Volodymyr Babin, Claude Leforestier, and Francesco Paesani. Development of a "first principles" water potential with flexible monomers: Dimer potential energy surface, vrt spectrum, and second virial coefficient. *Journal of Chemical Theory and Computation*, 9(12):5395–5403, 2013.

[23] Volodymyr Babin, Gregory R Medders, and Francesco Paesani. Development of a "first principles" water potential with flexible monomers. ii: Trimer potential energy surface, third virial coefficient, and small clusters. *Journal of Chemical Theory and Computation*, 10(4):1599–1607, 2014.

[24] Gregory R Medders, Volodymyr Babin, and Francesco Paesani. Development of a "first-principles" water potential with flexible monomers. iii. liquid phase properties. *Journal of Chemical Theory and Computation*, 10(8):2906–2910, 2014.

[25] Francesco Paesani. Getting the right answers for the right reasons: Toward predictive molecular simulations of water with many-body potential energy functions. *Accounts of Chemical Research*, 49(9):1844–1851, 2016.

[26] Masakazu Matsumoto, Takuma Yagasaki, and Hideki Tanaka. Genice: hydrogen-disordered ice generator, 2018.

[27] Asbjørn Nilsen Riseth. Objective acceleration for unconstrained optimization. *Numerical Linear Algebra with Applications*, 26(1):e2216, 2019.

[28] William W Hager and Hongchao Zhang. Algorithm 851: Cg_descent, a conjugate gradient method with guaranteed descent. *ACM Transactions on Mathematical Software (TOMS)*, 32(1):113–137, 2006.

[29] William W Hager and Hongchao Zhang. The limited memory conjugate gradient method. *SIAM Journal on Optimization*, 23(4):2150–2168, 2013.

[30] Jeff Bezanson, Alan Edelman, Stefan Karpinski, and Viral B Shah. Julia: A fresh approach to numerical computing. *SIAM Review*, 59(1):65–98, 2017.

[31] Brian C Ferrari. YetAnotherSimulationSuite.jl: An atomic simulation suite in julia. *Journal of Open Source Software*, 10(116):9480, 2025.

[32] P Mogensen and A Riseth. Optim: A mathematical optimization package for julia. *Journal of Open Source Software*, 3(24):615, 2018.

[33] Guillaume Fraux, Jonathan Fine, ezavod, German P. Barletta, Laura Scalfi, and Mykola Dimura. chemfiles/chemfiles: Version 0.9.3, February 2020. URL `https://doi.org/10.5281/zenodo.3653157`.

[34] Jonas Isensee. Jld2.jl. `https://github.com/JuliaIO/JLD2.jl`, 2025.

[35] Milan Bouchet-Valat and Bogumił Kamiński. Dataframes. jl: Flexible and fast tabular data in julia. *Journal of Statistical Software*, 107:1–32, 2023.

[36] Simon Danisch and Julius Krumbiegel. Makie.jl: Flexible high-performance data visualization for julia. *Journal of Open Source Software*, 6(65):3349, 2021.

[37] Marc Riera, Christopher Knight, Ethan F Bull-Vulpe, Xuanyu Zhu, Henry Agnew, Daniel GA Smith, Andrew C Simmonett, and Francesco Paesani. Mbx: A many-body energy and force calculator for data-driven many-body simulations. *The Journal of Chemical Physics*, 159(5), 2023.

[38] Joel Ireta, Jörg Neugebauer, and Matthias Scheffler. On the accuracy of dft for describing hydrogen bonds: dependence on the bond directionality. *The Journal of Physical Chemistry A*, 108(26):5692–5698, 2004.

[39] A Daniel Boese. Density functional theory and hydrogen bonds: are we there yet? *ChemPhysChem*, 16(5):978–985, 2015.

[40] Michael J Gillan, Dario Alfe, and Angelos Michaelides. Perspective: How good is dft for water? *The Journal of Chemical Physics*, 144(13), 2016.

[41] Edward Whalley. Energies of the phases of ice at zero temperature and pressure. *Journal of Chemical Physics*, 81(9):4087–4092, 1984.

[42] K Röttger, A Endriss, Jörg Ihringer, S Doyle, and WF Kuhs. Lattice constants and thermal expansion of h2o and d2o ice ih between 10 and 265 k. *Acta Crystallographica*, 50(6):644–648, 1994.

4.7 Bibliography

Chapter 5

Floating in Space: How to Treat the Weak Interaction between CO Molecules in Interstellar Ices

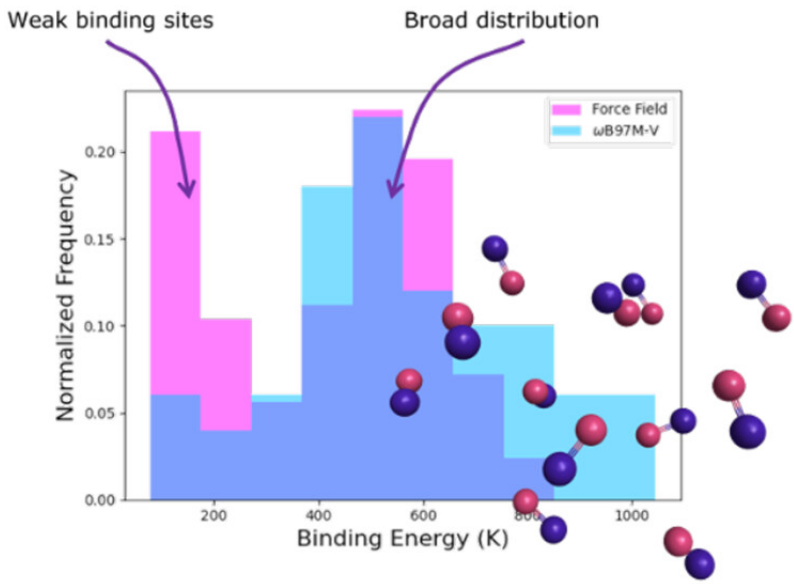

This chapter is based on:

Ferrari, B. C., Molpeceres, G., Kästner, J., Aikawa, Y., van Hemert, M., Meyer, J., & Lamberts, T. (2023). Floating in Space: How to Treat the Weak Interaction between CO Molecules in Interstellar Ices. ACS Earth and Space Chemistry, 7(7), 1423-1432.

5.1 Abstract

In the interstellar medium, six molecules have been conclusively detected in the solid state in interstellar ices, and a few dozen have been hypothesized and modeled to be present in the solid state as well. The icy mantles covering micron-sized dust grains are, in fact, thought to be at the core of complex molecule formation as a consequence of the local high density of molecules that are simultaneously adsorbed. From a structural perspective, the icy mantle is considered to be layered, with an amorphous water-rich inner layer surrounding the dust grain, covered by an amorphous CO-rich outer layer. Moreover, recent studies have suggested that the CO-rich layer might be crystalline and possibly even segregated as a single crystal atop the ice mantle. If so, there are far-reaching consequences for the formation of more complex organic molecules, such as methanol and sugars, that use CO as a backbone. Validation of these claims requires further investigation, in particular on acquiring atomistic insight into surface processes, such as adsorption, diffusion, and reactivity on CO ices.
Here, we present the first detailed computational study towards treating the weak interaction of (pure) CO ices. We provide a benchmark of the performance of various density functional theory methods in treating the binding of pure CO ices. Furthermore, we perform an atomistic and in-depth study of the binding energy of CO on amorphous and crystalline CO ices using a pair-potential-based force field. We find that CO adsorption is represented by a large distribution of binding energies (200 – 1600 K) on amorphous CO, including a significant amount of weak binding sites ($<$ 350 K). Both increasing the cluster size and the number of neighbors increases the mean of the observed binding energy distribution. Finally, we find that CO binding energies are dominated by dispersion, and, as such, exchange-correlation functionals need to include a treatment of dispersion to accurately simulate surface processes on CO ices. In particular, we find the ωB97M-V functional to be a strong candidate for such simulations.

5.2 Introduction

Carbon monoxide (CO) is ubiquitous throughout the interstellar medium (ISM), and within molecular clouds it is one of the most abundant molecules. It was first detected in the gas phase in 1970[1] and in the solid phase in 1979[2]. Solid CO ice is typically identified by its features at 4.67 and 4.681 μm, that have been shown to correspond to CO embedded in an apolar and polar environment, respectively[3]. This aligns with the

general idea that interstellar ices are layered, with first a polar, mixed, but water-rich inner layer then an apolar, mixed, but CO-rich outer layer[4,5]. This is supported by the novel James Webb Space Telescope (JWST) observation of NIR38, which found that fitted CO ice profiles are dominated by a pure component with two weaker mixed components.[6]

Recent studies claim that the CO-rich ice is formed as a single crystal atop an amorphous water-rich ice[7]. Kouchi *et al.* showed that amorphous CO (am-CO) deposited on amorphous solid water (ASW) was highly susceptible to Ostwald ripening during crystallisation, resulting in only a few crystal islands growing with others feeding into the larger ones[7,8]. They also showed that both UV and electron irradiation of crystalline α-CO do not destroy the crystal structure. Complimentary to this work, He *et al.* have found that pure CO ice under interstellar conditions and timescales is likely to be crystalline[9].

During deposition, Kouchi *et al.*[7] found that CO only partially wets the ASW surface whereas Noble *et al.*[10] found complete wetting. In the latter study, wetting was determined via temperature programmed desorption (TPD), whereas, the former directly imaged the surface during deposition with transmission electron microscopy (TEM). In TEM imaging, the thickness of the sample is determined by the darkness of the image. Identifying the growth of a single monolayer through this method is quite challenging. To reconcile the differences in observed wetting, Kouchi *et al.*[7] evaluated inequalities based on binding energies to suggest that CO first completely wets the ASW surface, then partially wets the CO surface coating the ASW. One crucial assumption was that the binding energy for CO on α-CO is identical to the binding energy for CO on am-CO. It is important to emphasise that this particular assumption (*vide infra*) has not been verified by any experiments so far.

While the majority of studies on the binding energy of CO are experimental, they yield a wide range of values, due to the different empirically motivated pre-exponential factors used to fit the data from TPD curves[11–14]. TPD studies have difficulties distinguishing the different binding on amorphous versus crystalline CO, because of (a) the narrow desorption temperature range and (b) the dependence on the experimental heating rate. Temperature interval desorption (TID) experiments can circumvent the dependence on the heating rate[14], but are susceptible to deviations arising from restructuring. Thus, computational studies with an appropriate level of accuracy are pivotal to understand the binding energy of pure CO at an atomistic level.

Computational studies on CO binding energies have been sparse, because finding an appropriate balance between accuracy and computational cost is very challenging for

this weakly bound system.[15,16] High(er) levels of (*ab initio*) theory cannot describe systems large enough to mimic amorphous systems. Thus, to allow larger system sizes, other techniques, such as; force field based classical molecular dynamics[17,18], continuous time random-walk Monte Carlo simulations[19], and kinetic Monte Carlo simulations[20,21] have been applied in recent years.

Here, we report a benchmark of a previously parametrized[17] classical force field (FF) against coupled cluster theory and a variety of exchange-correlation functionals rooted in density functional theory (DFT) with the aim of determining a reliable and cost-effective way to treat surface processes on CO ices. To this end, we compare binding energies for CO on am-CO which is modeled by small CO clusters. We further report FF-based results for the effect of cluster size on the binding energy distributions, as well as, binding energies of CO on α-CO. Our results are placed in the astrochemical context, and aim to lay the groundwork to provide recommendations for future selections of techniques and cluster sizes for studies of adsorption or dynamics on interstellar CO ices.

5.3 Computational Details

5.3.1 Force Field

The force field uses a site-site pair potential that was parameterized by van Hemert *et al.*[17] based on CCSD(T) calculations for the CO dimer using the aug-cc-pVQZ basis set in combination with the Boys-Bernardi counterpoise correction. An explanation of the potential is given in Chapter 2. The force field has been reimplemented in Python in the form of an Atomic Simulation Environment (ASE) calculator[22,23]. Our implementation of the force field used for the calculations in this work does not employ any cutoffs for energy and force evaluations. The values for all parameters are summarized in Table 2.1. We estimate the (intermolecular) many-body effects beyond pair interactions to amount to less than 2% of the total interaction energy (see Section 1 of S.I. for details).

Simulation Procedures

We generated the amorphous clusters through an in-house "hit-and-stick" script. A randomly oriented CO molecule was spawned 8 Å away from the surface of the CO cluster in a random direction with $\sim$ 50 K of translational energy in the direction of the center of mass of the CO cluster, followed by a 5 ps microcanonical (NVE)

ensemble simulation using the ASE (version 3.22.1) implementation of the velocity Verlet algorithm[24,25]. Subsequently, a geometry optimization was run with the ASE implementation of the Broyden–Fletcher–Goldfarb–Shanno (BFGS) optimizer[26] using a convergence criterion of 1×10^{-6} eV/Å as a maximum force per atom. This procedure was repeated until the cluster reached a specified number of molecules which was passed to it as an input. Using this technique, 220 clusters were generated with sizes ranging from 8 to 350 CO molecules.

Binding sites for amorphous clusters were sampled by first constructing an α-shape[27], the "shape" of a set of finite points in space, around the atoms.[1] The α parameter was optimized such that the α-shape would fully enclose all atoms while minimizing the volume enclosed. The vertices of the α-shape were then uniformly sampled and a new randomly orientated CO molecule was placed $3-5$ Å away from the norm of the sampled vertex, with the restriction that no atom in the new molecule was closer than 3 Å from any cluster atom. This ensured binding sites selected were equally spaced both from each other and the nearest CO molecule. The cluster and admolecule complex was then optimized to a maximum force per atom of 1×10^{-3} eV/Å. The convergence criteria here and for the "hit-and-stick" procedure were carefully selected based on a study of their effects on the binding energy distributions (see Section 2 of S.I. for details). After geometry optimization, the number of nearest neighbors was determined by counting all molecules with at least one atom within 3.6 Å distance of either C or O of the adsorbing CO molecule.

An α-CO crystal was created by using symmetry operators from the $P2_13$ space group with lattice parameters $a = b = c = 5.9638$ Å, $\alpha = \beta = \gamma = 90°$. We first cut out a cubic $(\alpha\text{-CO})_{864}$ finite cluster from this crystal, which was terminated by {100} faces, and optimized it with a tight (1×10^{-6} eV/Å) convergence criterion. To avoid edge effects except for where adsorption of additional CO molecules is being studied (i.e., at the "sides and at the bottom"), a $(\alpha\text{-CO})_{256}$ cluster is cut out from the center of one of the (100) faces of the $(\alpha\text{-CO})_{864}$ cluster. By freezing out the subsurface molecules they retain their crystalline character, and only the surface edges lose their crystalline character.

CO molecules were placed initially at distances of 3 Å above the crystal face. A total of 500 randomly sampled sites with a randomly orientated CO molecule were used to calculate the binding energies. Only the top layer and admolecule were free to move during optimization, the complex (CO + $\alpha\text{-CO}_{256}$) was optimized with the

[1] An α-shape is a set of lines that encloses a finite set of points. In this particular case, the α-shape is the surface of the amorphous clusters, with the atoms on the cluster surface being the vertices.

BFGS optimizer and a moderate (1×10^{-3} eV/Å) convergence criterion. A buffer region between the plane and crystal edge was left to ensure edge-sites would not be included in the binding energy distributions. The above procedure aims for a realistic simulation of adsorption on a α-CO crystal considering periodic boundary conditions were not applied.

Binding energies for both am-CO and α-CO are calculated via

$$E_{\mathrm{BE}} = (E_{\mathrm{clu}} + E_{\mathrm{mol}}) - E_{\mathrm{clu\,+\,mol}} \tag{5.1}$$

where E_{clu} is the energy of the optimized cluster, E_{mol} is the energy of a single optimized CO molecule, and $E_{\mathrm{clu\,+\,mol}}$ is the energy of the optimized complex (cluster with adsorbed CO). Vibrational zero-point energies (ZPE) were calculated within the harmonic approximation for am-CO, and their contribution to the binding energy is given via $\Delta\mathrm{ZPE} = (\mathrm{ZPE}_{\mathrm{clu}} + \mathrm{ZPE}_{\mathrm{mol}}) - \mathrm{ZPE}_{\mathrm{clu\,+\,mol}}$. Vibrational frequency calculations were carried out with the ASE (version 3.22.1) vibrations package, using finite displacements of $\pm 1 \times 10^{-4}$ Å. All systems studied in this work yielded a total of 4 or less imaginary modes, which are not related to the adsorbate motion. The sum of their absolute values corresponds to a ZPE of 0.2 meV or less, which was omitted when calculating the ZPE corrections.

5.3.2 Density Functional Theory

We compare the interaction energy ($\Delta E_{\mathrm{int}} = E_{\mathrm{dimer}} - 2 \cdot E_{\mathrm{CO}}$) of four randomly oriented CO–CO dimers optimized at the CCSD(T)/ma-def2-TZVP level of theory, with the ORCA program (version 5.0.3)[28,29], against a series of exchange and correlation density functionals. Given the importance of the dispersion interaction for weakly interacting systems[30], we treat dispersion in two ways: (A) *via* Grimme's dispersion correction, either the fourth generation D4[31], or D3[32] including three-body contributions, and (B) including a fraction of non-local (NL) correlation energy in the exchange and correlation energy. Under the latter formalism, the total exchange and correlation energy becomes

$$E_{\mathrm{XC}}^{\mathrm{NL}} = E_{\mathrm{X}} + E_{\mathrm{C}} + E_{\mathrm{C\text{-}NL}}, \tag{5.2}$$

where E_{X} and E_{C} denote exchange and correlation energies according to a particular functional, and $E_{\mathrm{C\text{-}NL}}$ accounts for non-local correlation following the formalism of Vydrov and Van Voorhis.[33] All DFT calculations used the ma-def2-TZVP[34,35] basis set, including a minimal set of diffuse functions to capture long-range interactions and

have been carried out with the ORCA program (version 5.0.3).[28,29] Due to a bug in ORCA version 5.0.3 associated with the D4 method, calculations using this method were corrected with ORCA version 5.0.4. All-but-one corrections were smaller than 10 K. To minimize numerical errors, a large integration grid (`defgrid3`) was used throughout the calculations. This is most important for meta-GGA functionals prone to bigger integration errors, however, to ensure consistency between calculations all functionals are integrated with the same numerical grid. For all functionals, except ωB97M-V, the calculations made use of the RIJK technique, e.g, resolution of the identity for the Coulomb and Exchange integrals. For the ωB97M-V functional, a *chain of spheres* evaluation of exchange (RIJCOSX in ORCA) was employed.

Furthermore, we compare DFT based binding energy distributions with FF based distributions. For the DFT based distributions, CO clusters with sizes of 8, 10, and 12 molecules have been generated as described previously in Molpeceres and Kästner.[36] This procedure differs from the "hit-and-stick" procedure mentioned in Section 5.3.1, because such an individual sticking procedure carried out at the DFT level would be too computationally expensive for the cluster sizes under consideration. Instead, initial structures were randomly generated using Packmol[37]. Subsequently, the structures are pre-conditioned using the generic GFN-FF method within the extended tight-binding (xTB) theoretical framework in the following way.[38,39] A long molecular dynamics (MD) simulation is run at 100 K for 100 ps for each structural model, to generate different starting configurations, applying a spherical wall potential to confine the CO molecules within the cluster and prevent evaporation of the ice. From this, we extracted an MD snapshot every 20 ps, which was quenched to 10 K for an additional 10 ps. These five initial structures per cluster size (15 in total) were subsequently optimized at the ωB97M-V/ma-def2-TZVP level of theory under strict convergence criteria: Max(E_{diff})= 1.0×10^{-7} E_h, Max(Step)= 3.0×10^{-4} Bohr, RMS(Step)= 2.0×10^{-4} Bohr, Max(F)= 7.5×10^{-5} E_h/Bohr, and RMS(F)= 5.0×10^{-5} E_h/Bohr.

Binding energy calculations were performed by placing additional CO molecules around the cluster, spanning a distorted Fibonacci lattice, with the centre of mass of each additional CO molecule at a (minimum) distance of 3 Å plus the maximum value of the Cartesian (x, y, and z) coordinate of any of the CO molecules in the cluster. More details for the sampling procedure can be found in[36]. To avoid surface restructuring, these initial configurations are relaxed with slightly less strict convergence criteria; Max(E_{diff})= 2.2×10^{-7} E_h, Max(Step)= 4.0×10^{-4} Bohr, RMS(Step)= 2.6×10^{-4} Bohr, Max(F)= 1.0×10^{-4} E_h/Bohr, and RMS(F)= 6.6×10^{-5} E_h/Bohr. For the $(CO)_{12}$ cluster, we fixed all the molecules present at a distance higher than 6.5 Å from

the admolecule's centre-of-mass, to ease the convergence of the geometry optimization procedure. Binding energies are calculated using Eqn. 5.1. We note that the aforementioned geometry optimization thresholds are less strict than those used for the FF calculations, owing to the fact that the energy and force calculations at the DFT level increase the computational time by about 5-6 orders of magnitude. Nevertheless, according to our detailed analysis in the S.I. (see Section 2), we do not expect this to have a significant effect on the calculated binding energies.

5.4 Results and Discussion

5.4.1 DFT Benchmark

The following functionals were tested: PBE-D3[40], B3LYP (without dispersion)[41], B3LYP-D4[31,41], B3LYP-NL[33,41], REVPBE0-D4[31,42], REVPBE0-NL[33,42], BHLYP-D4[31,43], M06-2X-D3[32,44], PW6B95-D4[31,45], PW6B95-NL[33,45] and ωB97M-V[46], which has the NL treatment in its original implementation. For each of these functionals, the dimer structure was re-optimized starting from the CCSD(T)/ma-def2-TZVP optimized geometries. The structures of the four dimer configurations are depicted in Fig. 5.1 (see Section 5 of S.I. for coordinates) and the calculated interaction energies are summarized in Table 5.1.

Overall, the degree of agreement between all DFT methods including dispersion and CCSD(T) is satisfactory, confirming previous calculations.[18,47,48] We observe that B3LYP without dispersion correction, yields results that are far from the reference value, while both D4 and NL corrections bring the values much closer to the reference. In general, NL-corrected functionals perform only slightly better compared to those with a D4 correction. Furthermore, PBE-D3, a commonly used method in computational solid state chemistry, clearly does not capture the interaction well, while the ωB97M-V functional outperforms all others. We further scrutinized the performance of the ωB97M-V functional by expressing the dimer potential explicitly in terms of radial and angular variables, similar to the method for the force field construction (see S.I. for details). We found good agreement between the ωB97M-V/ma-def2-TZVP potential and the CCSD(T)/aug-cc-pVQZ potential. Finally, note that a direct comparison to the energetics for these dimers predicted by the force field is not straightforward as a result of the use of different basis sets for the CCSD(T) calculations and the FF parametrisation.

The ωB97M-V/ma-def2-TZVP level of theory will be used for all future DFT

calculations discussed here and the applicability of this method to general adsorbates and reactions on ice clusters will be the subject of future work.

Table 5.1: Dimer interaction energy, E_{int}, for the reference method CCSD(T)/ma-def2-TZVP and the difference $\Delta E_{\text{int}} = E_{\text{int,CCSD(T)}} - E_{\text{int,DFT}}$ for different exchange and correlation functionals in Kelvin.

		Dimer 1	Dimer 2	Dimer 3	Dimer 4
CCSD(T)	E_{int}	*-158.4*	*-163.4*	*-149.3*	*-112.0*
PBE-D3		68.2	63.0	77.2	114.5
B3LYP		-153.2	-152.0	-143.1	-122.2
B3LYP-D4*		9.9	-18.4	12.2	3.6
B3LYP-NL		-15.2	-28.7	-0.2	-24.3
BHLYP-D4*		46.6	22.5	47.8	22.9
M06-2X-D3	ΔE_{int}	-19.2	-9.4	-18.0	-5.4
PW6B95-D4*		69.8	69.7	69.1	88.7
PW6B95-NL		59.0	67.1	55.3	76.3
REVPBE0-D4*		48.3	26.3	52.8	58.2
REVPBE0-NL		24.3	21.6	32.8	36.1
ωB97M-V		**0.7**	**1.6**	**-0.3**	**4.8**

5.4.2 Amorphous CO

Comparison between FF and DFT

We compared DFT and FF-based binding energy distributions for cluster sizes of 8, 10 and 12 CO molecules. Thanks to the computational efficiency of the FF method we have used larger sample sizes of 200, 250, and 300 respectively, in comparison to 60, 50, and 40 for the DFT calculations. The resulting distributions are depicted in Figure 5.2. Only for small clusters (16 or less CO molecules) the distributions were bi-modal, as such, only those distributions were fit with two Gaussian profiles. In both Figure 5.2 and Table 5.2, for the bi-modal cases only the descriptors for the higher BE distribution is shown. We find very good agreement between the DFT and FF binding energy distributions. The correspondence between FF and DFT results are underpinned by the descriptors of the distributions for all amorphous clusters studied, presented in Table 5.2. The standard deviations (σ, governing the width of the distribution) are in agreement even in cases where the means (μ, governing the average binding energy) differ between FF and DFT. However, the median (η) and the Median Absolute Deviation (MAD) on the other hand are more robust descriptors of the distributions. The median of the distribution is less sensitive to outliers and, in

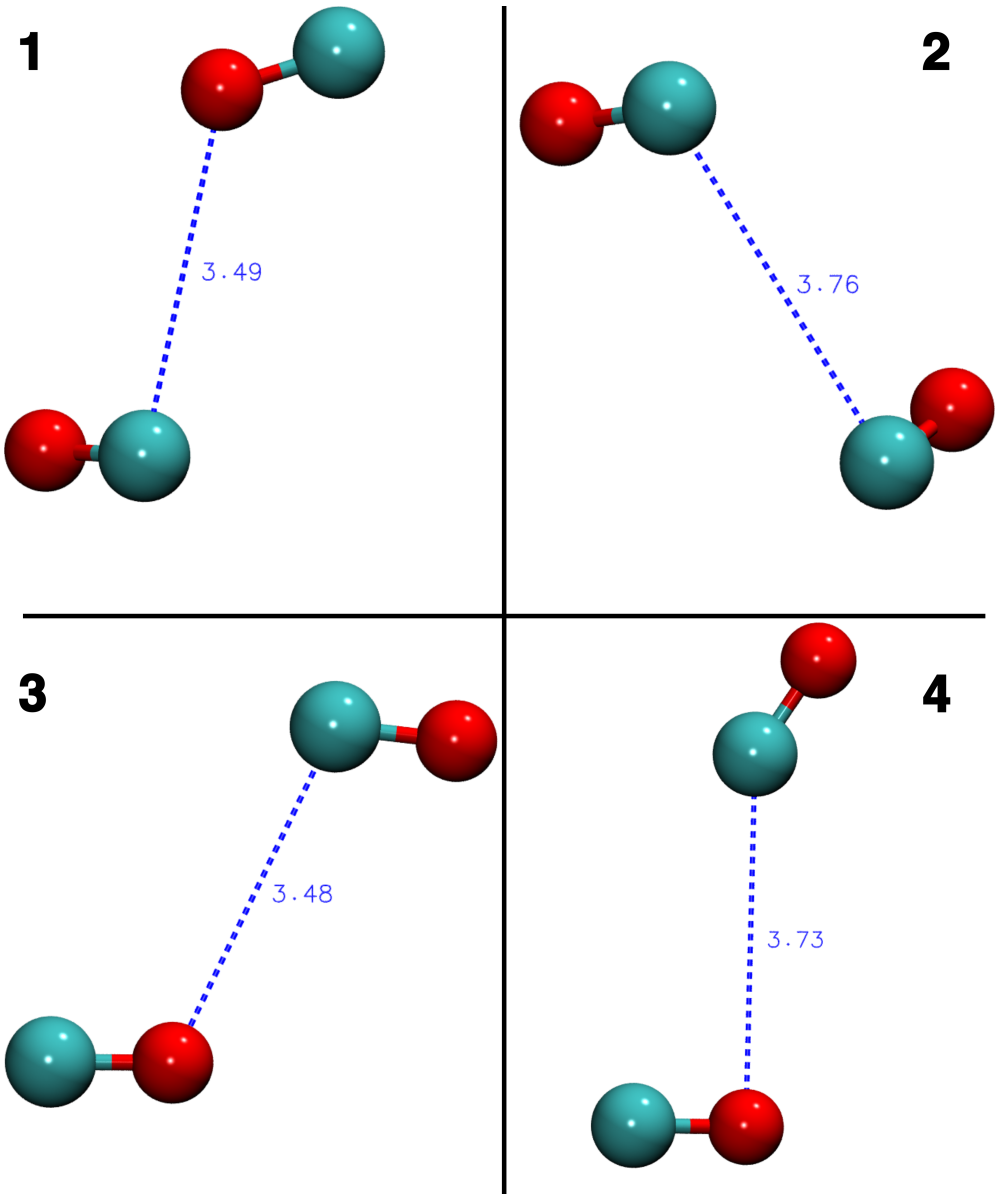

Figure 5.1: CO dimer configurations used to determine the interaction energies utilized in our benchmark study (Table 5.1). Full geometry coordinates are given in the SI.

line with earlier work, we recommend using the median to estimate binding energies in these weakly bound systems.[18]

Both methods find many weakly bound configurations, however, more so for the FF method. In particular, there is a significant amount of extremely weak (< 200 K) binding sites. Subsequent NVE MD simulations at the FF level (with time steps of 0.5 fs) revealed these binding sites are transient. Residual forces in those weakly bound configuration were sufficiently large so that the adsorbed CO diffuses to a stronger binding site during short timescales (∼ 1 ps). The relative abundance of these sites for FF simulations diminishes with increasing cluster size, see Figure 5.2d, as such, studies with small cluster sizes should scrutinize the relative abundance of these sites. For cluster sizes larger than 100 CO molecules these sites make 1% or less of the sample size, and for 350 CO molecules it is down to 1 transient site out of 550 samples. Since these sites disappear for larger cluster sizes, it implies they arise from adsorption at defect sites, where there is a reduced number of interactions.

Table 5.2: Mean (μ), standard deviation (σ), median (η), and median absolute deviation (MAD), smallest binding energy (E_{BE}^{min}) and largest binding energy (E_{BE}^{max}) of the CO-COn. All values of the table are in Kelvin.

Cluster Size	Method	μ		σ		η		MAD		E_{BE}^{min}		E_{BE}^{max}	
		a	b	a	b	a	b	a	b	a	b	a	b
8	FF	498	356	101	79	498	359	101	69	142	90	753	551
8	DFT	543		120		547		103		151		851	
10	FF	542	391	112	86	531	381	116	90	147	95	839	613
10	DFT	604		195		560		174		77		1044	
12	FF	562	409	130	105	565	397	115	92	147	95	1192	915
12	DFT	525		159		528		174		126		1049	
16	FF	611	451	148	125	611	459	152	129	153	97	954	753
24	FF	600	454	189	152	616	467	164	135	154	103	1088	795
32	FF	617	470	187	152	630	474	160	139	153	106	1161	917
48	FF	665	508	183	150	670	512	148	120	151	98	1280	1050
75	FF	676	523	175	145	689	526	137	112	157	106	1115	894
96	FF	717	550	183	148	730	552	144	119	172	129	1311	1030
150	FF	742	564	177	147	771	593	171	146	174	113	1205	899
200	FF	835	633	227	180	837	640	178	126	169	109	1610	1301
250	FF	755	598	181	154	785	624	161	139	167	107	1302	1088
350	FF	786	625	184	154	802	640	158	140	199	141	1506	1304

[a] Without ZPE corrections
[b] With ZPE corrections

Dispersion Contribution

Figure 5.3 shows the contribution of each intermolecular interaction on the binding energy of CO on amorphous CO clusters. The dispersion (V_{disp}) contribution dominates the binding energy, as expected, further underpinning the importance of the inclusion

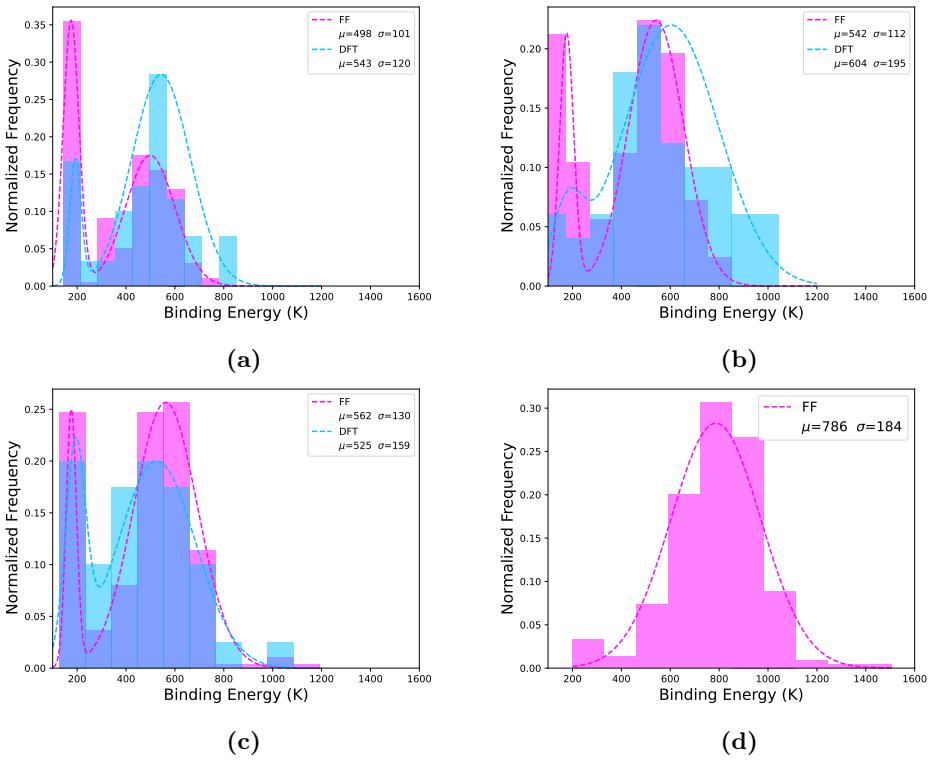

Figure 5.2: Distributions of binding energies calculated by DFT (blue) and FF (pink) methods for cluster sizes of (a) 8, (b) 10, (c) 12, and (d) 350 CO molecules. The mean (μ) and standard deviation (σ), both in K, for each distribution is shown in the plot legends. Dotted lines are probability density functions fitted to the binding energy distributions. For all distributions 10 equally spaced bins were used for plotting. Distributions consist of (a) 60 DFT samples and 200 FF samples (b) 50 DFT samples and 250 FF samples (c) 40 DFT samples and 300 FF samples (d) 550 FF samples. Note, overlapping blue and pink bars result in a third color within the plots.

of dispersion in exchange-correlation functionals used to simulate surface processes on CO ices. We also include the Buckingham potential ($V_{\text{exch}} + V_{\text{disp}}$) contribution since it illustrates the interplay between the exchange and dispersion contributions. Interestingly, the dispersion and exchange contributions vary significantly across binding arrangements, whereas, their combined interaction (Buckingham) seem to balance each other out to produce a contribution with less variation. Contrary to water clusters, here the electrostatic (V_{el}) contribution is the weakest (by absolute magnitude) contribution to the binding energy, with ~ 100 K of the binding energy resulting from electrostatic interactions.

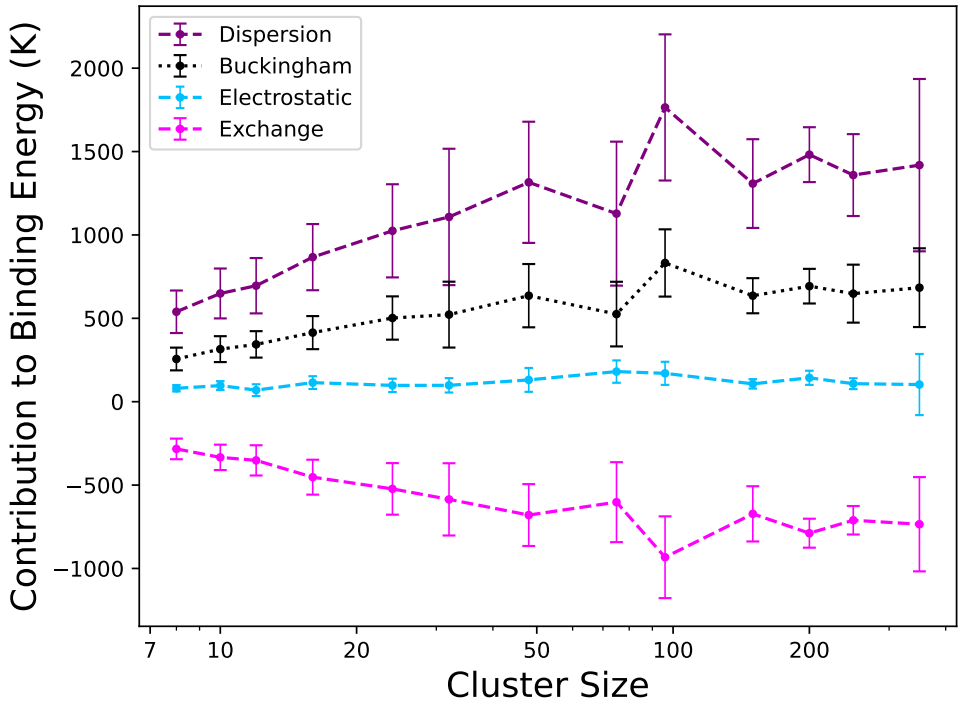

Figure 5.3: Average contribution to the binding energy of each part of the force field employed. Points are the mean of the contribution distributions, error-bars are the standard deviation and dashed/dotted lines are a guide for the eye.

$(CO)_x$ clusters have a key peculiarity in comparison with $(H_2O)_x$ ones, which has been the most commonly used substance to simulate interstellar ices. In water, the dominant interaction is brought about by the hydrogen bonds between molecules, which is directional and strong. On the contrary, in solid-state CO ices most of

the interaction energy stems from the dispersion interactions, as such, CO molecules tend to orient with less directionality than H_2O. As a consequence, while dual-level calculations with electronic energy refinement on a low-level geometry are a cheap and accurate way to describe reaction energetics, the physisorption of CO admolecules on CO clusters is not well captured.

Binding Energy Size Trend

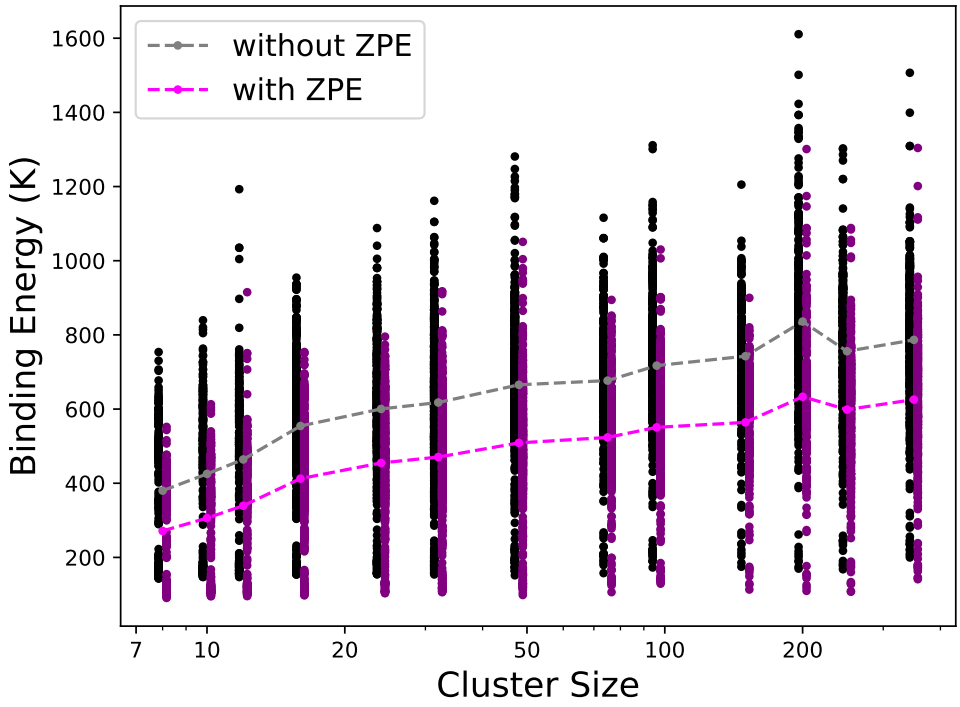

Figure 5.4: Black and purple dots are binding energy distributions, the grey and fuchsia dots are the median values of the distributions. Dashed lines do not indicate predicted trends.

It is important to study the cluster size dependence because the weak dispersion results in short-range interactions that do not dominate over the long-range ones. We find that the median binding energy for a cluster size of 350 molecules (802 K) is nearly twice the median binding energy for a cluster size of 8 molecules (426 K). Figure 5.4 shows the effect of cluster size on the binding energy distribution, where both ZPE corrected and uncorrected binding energies are shown. The binding energies are shown

as black and purple scatter points and demonstrate a wide range of binding sites on am-CO. Larger cluster sizes increase the overall binding energy, with the median value seeming to asymptotically approach the previously reported experimental values by Acharyya *et al.*[12] (858 ± 15 K) and Bisschop *et al.*[13] (855 ± 25 K).

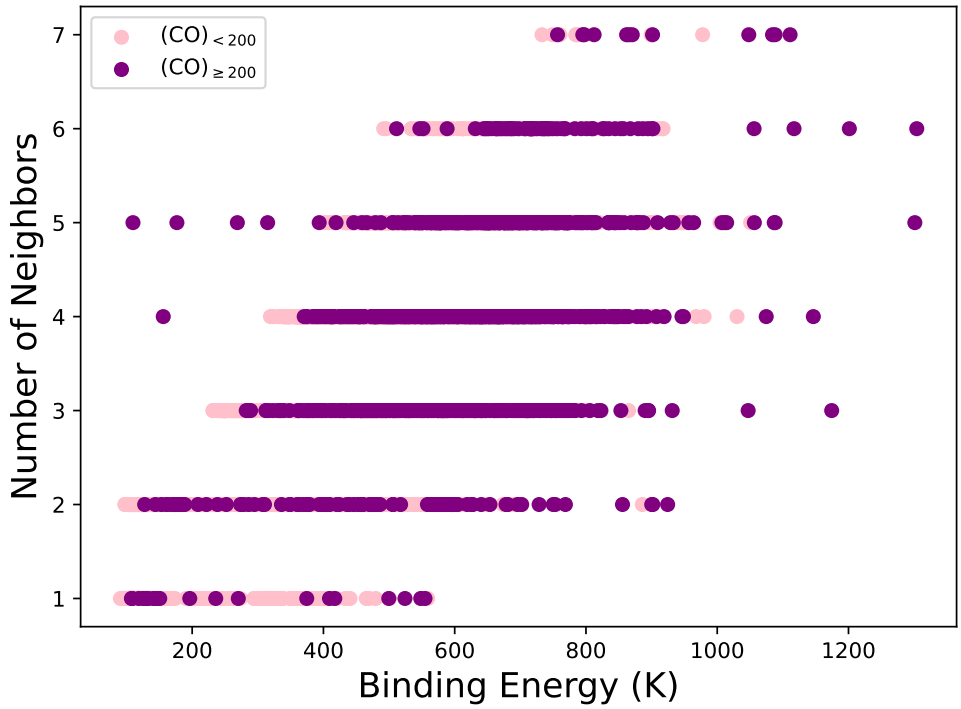

Figure 5.5: All FF calculated binding energies with ZPE corrections plotted as a function of number of nearest neighbors. Results for cluster sizes less than 200 molecules are pink and all larger clusters are purple.

In general, the largest binding energy at each cluster size increases with increasing size until 50 CO molecules. The $(CO)_{12}$ cluster is an exception due to one of the $(CO)_{13}$ complexes (CO + $(CO)_{12}$) having a uniquely symmetric orientation. This allowed the adsorbing CO to maximize its number of nearest neighbors, producing a binding energy significantly higher than on most other clusters. Larger clusters have maximum binding energies that depend less on the cluster size and depend more on the surface morphology, and the number of nearest neighbors. Figure 5.5 shows the relationship between binding energy and number of nearest neighbors. Increasing the number of neighbors shifts the distribution of binding energies to larger values, because

short range interactions contribute more to the binding energy.

The ZPE correction lowers the median binding energy by 20 – 30% and reduces the MAD by 15 – 20%. This reduction is greater than or equal to ZPE contributions found from previously reported studies of other molecules on water ice surfaces [48,49]. For a weakly interacting system, such as CO on CO, the ZPE corrections can influence binding significantly and should be carefully considered. The ZPE corrections are calculated within the harmonic approximation. This may result in an overestimation, because the weak CO−CO interactions on a relatively flat PES which are expected to be dominated by anharmonic character. We find that the low frequency modes dominate the ΔZPE with the largest contributions resulting from the frozen-out rotations and translation of the "newly" adsorbed CO molecule. Since these modes are more anharmonic in nature we expect anharmonic corrections to the ZPE to be significant. As such, the ZPE corrections reported here are an upper limit on the exact ZPE correction.

5.4.3 Crystalline CO

The binding energy distribution for CO on the (100) surface of α-CO is shown in Figure 5.6. The weakest binding sites ($\sim$ 500 K shown in red in Figure 5.6) correspond to sites directly on top of a CO molecule on the topmost CO layer, and the strongest binding sites ($\sim$ 800 K shown in pink in Figure 5.6) correspond to CO alignment with a subsurface α-CO molecule. Similar to the amorphous case, the weak binding sites ($<$ 650 K) are found to be transient, with CO diffusing into a site above a subsurface α-CO molecule when subsequent NVE simulations are performed. It then binds in orientations similar to those of the stronger binding sites mentioned above. Our calculations only consider the perfectly flat (100) CO crystal surface, and thus do not include the influence of step edges. Ignoring these effects, we find that the median binding energy of CO on α-$(CO)_{256}$ (742 K) is similar to that of CO on am-$(CO)_{250}$ (785 K); validating assumptions made in previous studies. [7]

In order to asses how the orientation of the adsorbing CO affects the binding energy we ran a density based spatial clustering of applications with noise (DBSCAN) [50] algorithm on the orientation of adsorbed molecules. The molecules were assigned a category based on their relative alignment with the second crystal layer, the categories were then used to color the distribution in Figure 5.6 (see S.I. for more details). A representative image for each category corresponding to the strongest binding sites is shown in Figure 5.7. The DBSCAN algorithm also separates "noise", points that are

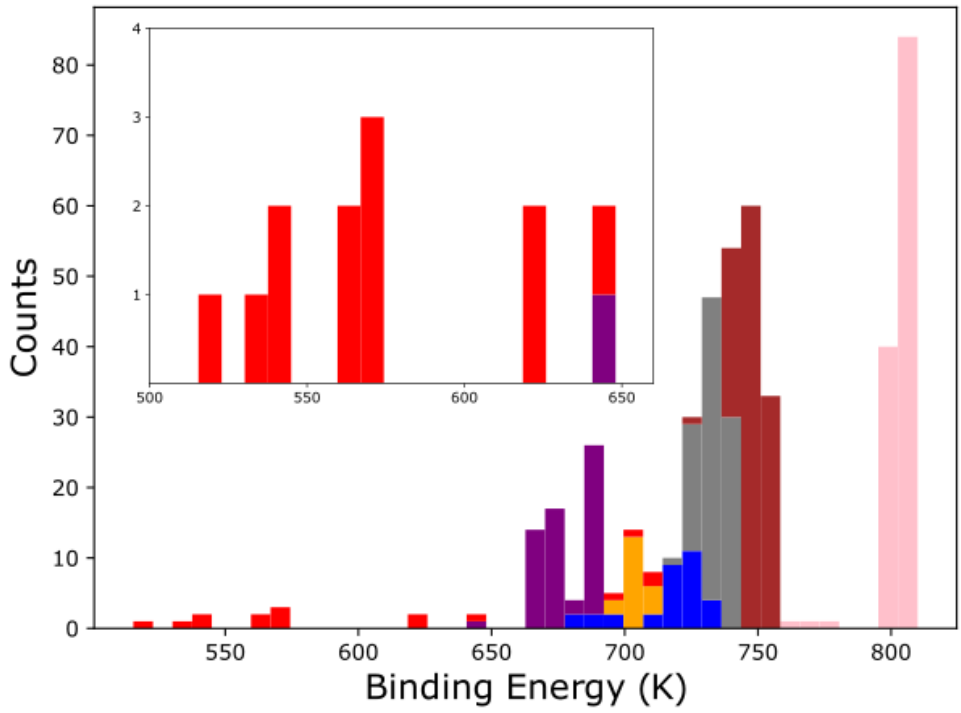

Figure 5.6: Distribution of binding energies calculated for a CO molecule adsorbed on the (100) surface of an α-CO crystal. Colors depict categories (see Figure 5.7) found by a clustering algorithm with reference to the orientation of the adsorbed CO. Inset is zoomed in on the low energy sites.

not similar to other points based on clustering space, represented by the red bars in Figure 5.6. In general, we can conclude that the more parallel the orientation of the adsorbed CO is with the subsurface α-CO below it, the higher the binding energy.

Many binding sites center around 740 K and they differ geometrically from the stronger sites around 800 K by the orientation of the adsorbed CO molecule, see Figure 5.7. Stronger binding occurs when the adsorbed molecule is approximately parallel to the sub-surface CO, with the adsorbed CO being inverted (in terms of C-down or O-down). Although being the strongest binding orientation, this does not correspond to full alignment with the crystal structure. Those orientations have a CO molecule parallel to the sub-surface CO, but non-inverted and the binding energies fall within the distribution centered around 740 K.

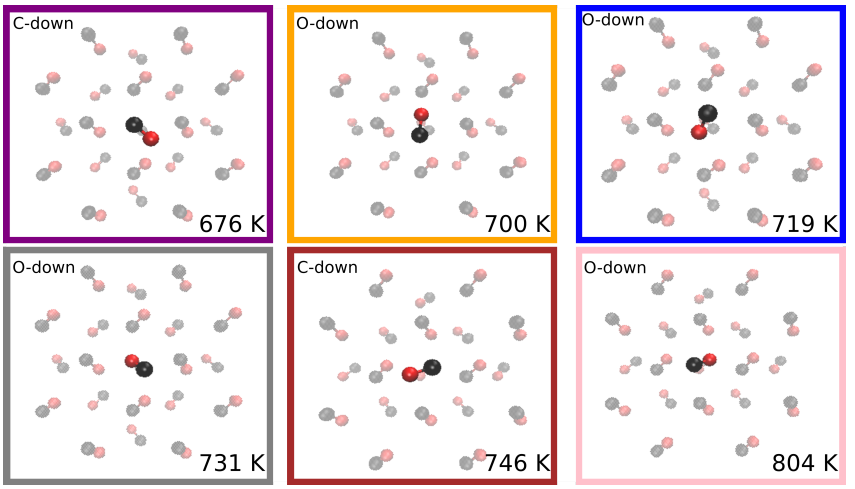

Figure 5.7: A representative image of each category for binding sites on the (100) surface of an α-CO crystal. Colored boxes indicate the category color in the histogram (see Figure 5.6), and text in upper left corner of each box indicates which atom is closest to the crystal face. Text in the lower right corner of each box is the median binding energy of the categories distribution. "Noise" points (red color in Figure 5.6) are not shown here since all orientations in the distribution differ significantly from each other. Note, all molecules shown here are adsorbed on a hollow site (over a CO molecule in the second layer).

5.5 Astrophysical Implications

We find that for large clusters (> 200 CO molecules) roughly 10% of the binding energy distributions falls below 600 K. This supports the idea that CO molecules are mobile even at low temperatures. This could promote the crystallization of the CO ice on interstellar timescales, which would support recent claims of interstellar CO being in crystalline form[7,9]. Whether or not the structural phase of CO ices has an effect on subsequent reactivity remains to be tested. It may lead to less accessible transition states for, e.g., the H + CO reaction, but given its intrinsic weakly interacting nature, it is possible that these effects are only observed in a single crystal without step edges or defects. As such, future studies on how the CO ice phase affects surface reactions would be of great interest to the astrochemical community.

The broad binding energy distributions reported herein are of particular interest to astrochemists modeling CO in pre-stellar cores. Within these regions there is evidence of a significant CO depletion in the gas-phase, between 74% and 94% of the gas-phase CO is observed to be frozen out.[51] However, models are unable to reproduce the observed gas-phase CO abundances and overestimate the CO depletion. For instance,

Keto and Caselli were only able to reproduce the observed value by increasing the cosmic-ray induced desorption rate for CO by a factor of 30 from what is expected.[52,53] Alternatively, Cazaux *et al.* showed that incorporating lower binding energy values for CO in models would decrease the CO depletion.[54] They found that using a binding energy of 350 K would lower the CO depletion by 10% and a value of 300 K would lower it by 100%.[54] Our results show that these binding energy values are within the distribution for CO. Additionally, we found that adsorption to defect sites are transient and in the limit of low CO coverage they will diffuse to stronger binding sites. At higher CO coverage, stronger binding sites will already be occupied and the admolecule will be unable to diffuse to a new site, resulting in a low temperature desorption event. Incorporating these concepts along with their probabilities into models could result in gas-phase CO abundances closer to those observed, without the need to invoke additional processes.

5.6 Conclusion

In summary, we find that CO binding is dominated by dispersion, and that many-body effects contribute minimally ($< 2\%$) to the interactions in CO ices. We also show that CO binding on amorphous CO occurs with a large range of binding energies (200 – 1600 K), and depends on both the cluster size and the number of nearest neighbors. Our results show a median binding energy of 802 K for $(CO)_{350}$, which is nearly twice as large as that for $(CO)_8$ (426 K). Accounting for ZPE within the harmonic approximation lowers the average binding energies by 20–30%. We expect this to be an upper limit because frustrated rotations and translations dominate the ZPE correction and the effect of these low-frequency modes might be overestimated by neglecting anharmonicity. This should be revisited in future studies.

We also report binding energy distributions (650 – 800 K) for CO binding on a flat α-CO crystal face, which we find to be orientation dependent. It also has a median value similar to that of amorphous CO, corroborating previous studies which assumed them to be equal. Lastly, we presented many dispersion corrected functionals that performed well, however, we find the ωB97M-V functional performs the best when treating the CO−CO dimer interaction and suggest this functional to be used for general adsorbates and reactions on ice clusters.

5.7 Data Availability Statement

All of the Python code used for the simulations is publicly available on GitHub at https://github.com/Cavenfish/CO_Project. XYZ files for all clusters used in this work can be found on Zenodo at https://zenodo.org/records/8068393.

5.A Appendix

5.A.1 Pair Interaction Validation

We estimate the (intermolecular) many-body effects beyond pair interactions to amount to less than 2% based on the procedure outlined below. We selected 20 trimer geometries and have performed CCSD(T)/aug-cc-pVQZ calculations using the same computational setup as used for the construction of the force field. Ten geometries were selected from the bulk of an unequilibrated $(CO)_{522}$ 'crystal' cluster, and the other ten were selected from the bulk of a $(CO)_{800}$ amorphous cluster equilibrated to 10 K.[17] For each geometry the total energy was calculated (E_{total}) and the energies of each pair ($E_{dimer,i}$) with the difference (Eqn. 5.A.3) attributed to non-additivity.

$$\Delta E = E_{\text{total}} - \sum_{i} E_{\text{dimer},i} \tag{5.A.3}$$

We find that ΔE can be both positive or negative and varies between 0 and 2% of E_{trimer}, indicating that a pair potential approach to study, e.g., binding of pure CO ices, is justified.

5.A.2 Geometry Optimization Threshold

Using the force field employed in thie work, we investigated the convergence threshold criteria for the creation of interstellar relevant CO clusters and for the subsequent binding energy calculations and concomitant distributions. While global sampling schemes provide a systematic way to obtain meta-stable states, instead, here we use a more pragmatic approach. This is also of more practical relevance to electronic structure calculations given their much higher computational cost. To this end, two $(CO)_{32}$ clusters were generated with the hit-and-stick method discussed in the manuscript. We tested six convergence criteria for the residual forces, namely 1×10^{-x} with $x = 1, 2, 3, 4, 5, 6$ eV/Å, leading to a total of 12 generated clusters. Subsequently, for each cluster ge-

ometry optimizations were performed for 60 binding sites and binding energies were computed for each convergence criterion equal to or looser than the one used for cluster generation, leading to 2520 simulations. The binding energies are calculated in the same method as described in the main article. The results are depicted in Fig. S5.A.8. As to be expected, the effect of the convergence criteria can be rationalized as follows: (a) during cluster generation, tightening the criteria results in a less disordered cluster and (b) during adsorption simulations, tightening the criteria forces the adsorbing molecule to overcome small barriers and progress toward stronger binding sites.

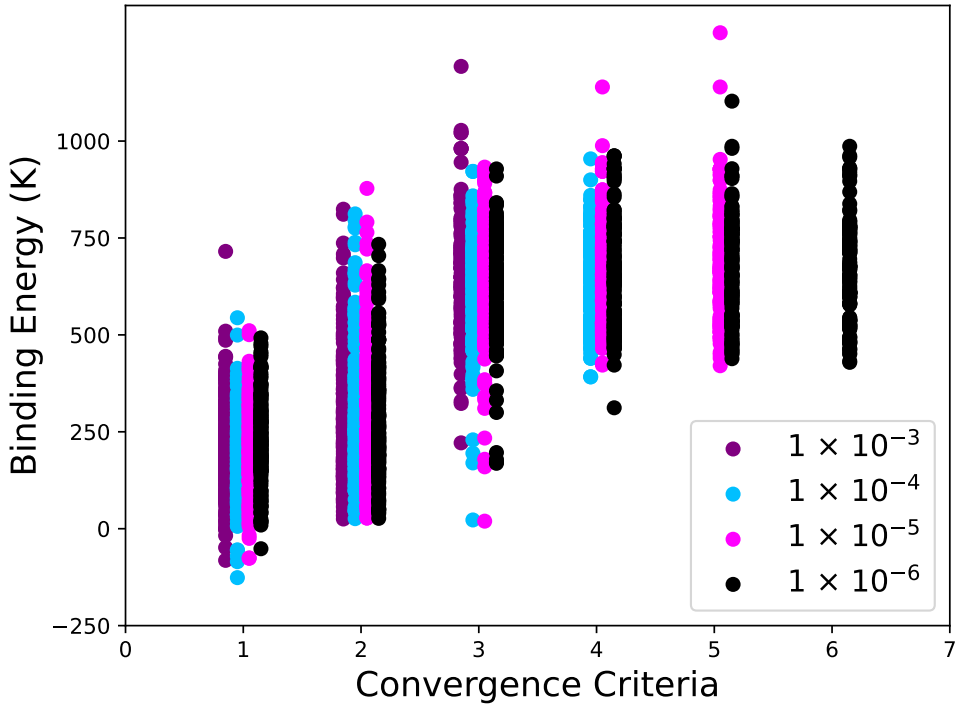

Figure 5.A.8: Binding energy distributions for simulations with varying optimization criteria, note that the points are artificially offset on x-axis for visibility. The x-axis denotes the convergence criteria for the binding energy (adsorption) simulations based on 1×10^{-x} eV/Å. The colors indicate the thresholds used for the cluster generation: (a) purple dots used 1×10^{-3} eV/Å (b) cyan dots used 1×10^{-4} eV/Å (c) magenta dots used 1×10^{-5} eV/Å (d) black dots used 1×10^{-6} eV/Å.

Tightening the criteria for the cluster creation overall leads to narrower binding energy distributions which can be seen by comparing within each set of calculations per criterion on the x-axis in Fig. S5.A.8. For instance, for a threshold of 1×10^{-3}

eV/Å on the adsorption simulations, the width of the black distribution (a threshold of 1×10^{-6} eV/Å for the cluster generation) is the smallest of all four colors. Tightening the criteria for the binding energy, *i.e.*, adsorption simulations, leads to an overall increase in binding energies and drastic reduction in the number of weak binding energies, because shallow minima will progress toward more stable local minima.

Computational chemistry studies usually focus on well-converged structures corresponding to local minima, if not even the global minimum. In this case it would mean to make use of threshold criteria of 1×10^{-6} eV/Å for both cluster formation and adsorption simulations. However, for the study of binding on cryogenic (10 K) interstellar ices, this would represent an unrealistic scenario: adsorbing molecules have near to no additional energy to reorient on the surface. In particular, transient binding sites for which the binding energy is sufficient to lead to adsorption, yet so low that subsequent diffusion leading to chemistry or fast desorption is expected, can not be captured with stringent convergence criteria. In fact, for CO, it has been shown that these weakly bound sites determine the gas-phase depletion rates and influence astronomical models[54]. At the same time, loose convergence criteria leads to negative binding energies representative of a repulsive force. Thus, for our work, keeping the interstellar conditions and questions in mind, we use 1×10^{-6} eV/Å as a criterion for generating the clusters and 1×10^{-3} eV/Å for computing the binding energies at the force field level. As detailed in the manuscript, different criteria are used for the electronic structure calculations in light of the concomitant computational costs.

5.A.3 Total Interaction Energy

In order to further elucidate the virtues and shortcomings of the ωB97M-V functional, we applied a spherical expansion analysis[55,56] previously used by van Hemert *et al.* for the original construction of the force field. We label the intermolecular distance (the distance between centers of mass of the two molecules) by R and use dimer jacobi angles (θ_A, θ_B and ϕ) for the orientation. The potential is then expressed as,

$$V(R, \theta_A, \theta_B, \phi) = \sum_{L_a, L_b, L} c_{L_a, L_b, L}(R)\ A_{L_a, L_b, L}(\theta_A, \theta_B, \phi) \tag{5.A.4}$$

with R-dependent expansion coefficients c (in energy units), dimensionless basis functions A and the angular momentum coupling labels given by L_a,L_b and L.

We focus here on the two best performing exchange-correlation functionals, ωB97M-V and B3LYP-D4 both including dispersion corrections, along with bare B3LYP to un-

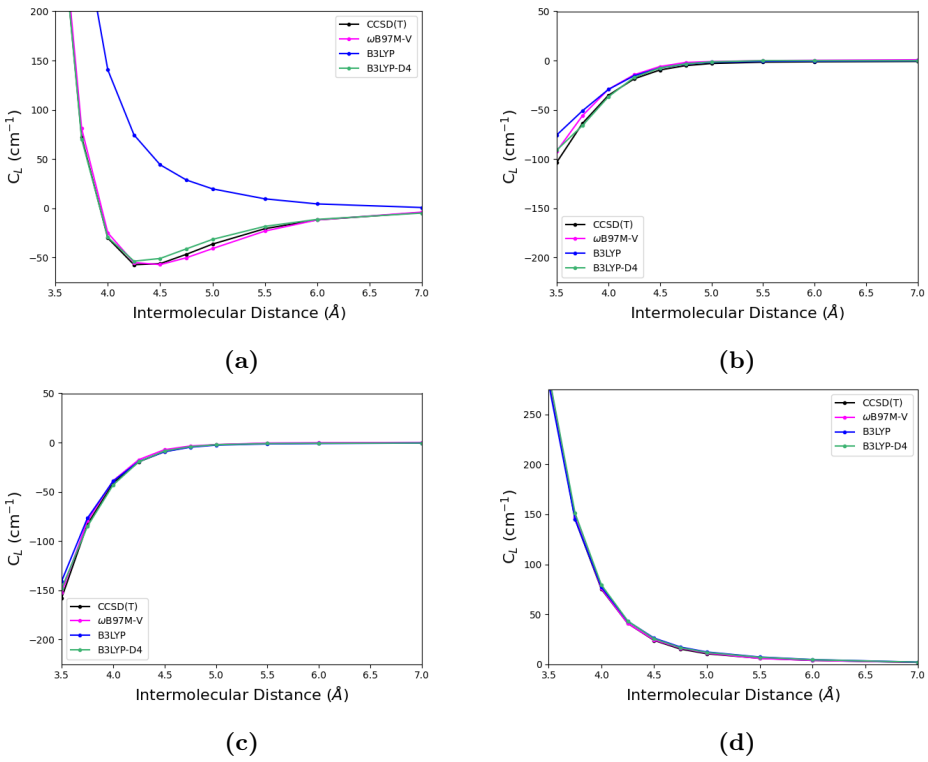

Figure 5.A.9: The intermolecular distance dependence of the dominant coefficients of the 140 term expansion. Shown here are (a) c_{000}, (b) c_{112}, (c) c_{123}, and (d) c_{224}.

derstand better the effects of dispersion. All functionals employed the ma-def2-TZVP basis set, and CCSD(T)/aug-cc-pVQZ acts as the reference. We use the Molpro program for all methods except ωB97M-V, which was run with ORCA. For 21 different intermolecular distances (R), the energy of 294 orientations was calculated. In Figure S5.A.9 we present the intermolecular distance dependence of the dominant coefficients of the truncated expansion including 140 terms.

Figures S5.A.9 (b), (c), and (d) show the 3 dominant anisotropy terms. At long range they determine the orientational dependence of (b) the dipole-dipole interaction, (c) the dipole-quadrupole interaction and (d) the quadrupole-quadrupole interaction. For R values larger than 10 Å, they show the expected R^{-n}, with n = 3, 4, and 5 for case (b), (c) and (d) respectively.

For the isotropic component, Figure S5.A.9 (a), the CCSD(T) reference curve (black) has its minimum at R=4.25 Å with -50 cm^{-1} energy. Both B3LYP-D4 (green)

and ωB97M-V (pink) reproduce the CCSD(T) curve closely, implying they incorporate dispersion in a similar way as CCSD(T). Bare B3LYP (blue) on the other hand demonstrates a lack of dispersion interaction, making it clear that B3LYP will always produce dimer equilibrium geometries with overestimated intermolecular distances.

This further underpins that ωB97M-V is well suited to treat CO ices, and may be able to describe other dispersion dominated systems as well. Considering its quality compared to its computational cost, we propose it to be an excellent functional for treating CO-CO interactions both for geometries and energies.

5.A.4 DBSCAN

Our goal in clustering the adsorbing geometries is to correlate the binding energy distributions with the orientation of the admolecule. In order to do so, we need to carefully select the features that will be supplied to the DBSCAN algorithm[50] to cluster the data. Within the α-CO crystal structure, there are two orientations of CO molecules per layer along the (100) direction, which defined the surfaces studied in the main article. Incidentally, the two have bond vectors that are nearly orthogonal. The relative alignment between the admolecule and one of these two CO orientations can be determined by taking the scalar product of unit vectors along the orientation of the two molecules. This provides a vector of 2 features that represents the general orientation of the admolecule, each in a range from -1 to 1. Figure 5.A.10 (a) shows these relative orientation features plotted for all sampled geometries prior to geometry optimization, and Figure S5.A.10 (b) shows them after geometry optimization. We then clustered the binding geometries based on these two features, using the DBSCAN algorithm. Figure S5.A.10 (c) shows the post-geometry optimization features plotted with color coded groupings determined by the DBSCAN algorithm.

The DBSCAN algorithm requires the selection of two important parameters, ϵ which is the 'neighborhood' radius and N which is the minimum number of points within a 'neighborhood' needed to make a point a core point. In our study we varied both parameters across $0.05 - 0.15$ for ϵ and $3 - 6$ for N, there was little difference in the resulting clusters. This is due to the tight packing of the data points. As such, we used a small value for the 'neighborhood' radius ($\epsilon = 0.05$) and a moderate minimum number of points ($N = 5$). This ensured that noise points were properly accounted for within the clustering scheme.

5.A.5 Dimer Geometries

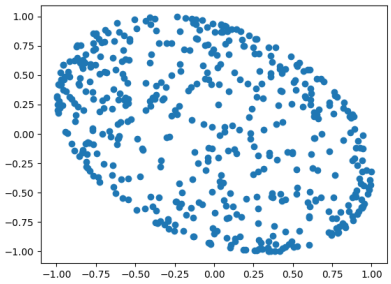

(a)

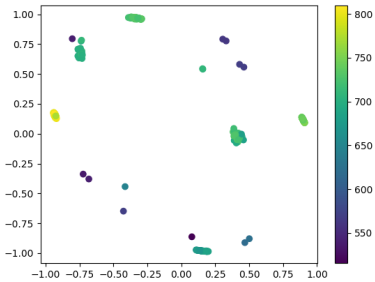

(b)

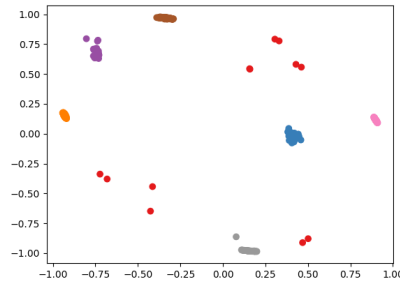

(c)

Figure 5.A.10: Relative orientation features plotted, with $x-$ and $y-$ describing the relative alignment between the admolecule and the CO molecules in the second layer as described in the text. The plots show (a) all sampled geometries prior to optimizations, (b) all optimized geometries with color bar indicating the binding energy and (c) all optimized geometries after DBSCAN clustering where the colors indicate their grouping.

Dimer 1	x	y	z
C	-0.19045519661532	-0.16135156541274	-0.90552295962114
O	-0.24781144304162	-0.21210633747172	0.22651845170074
C	2.05554035880910	1.76473141430682	1.93645844013598
O	1.92163442084784	1.61431360857763	3.05282589778442
Dimer 2	x	y	z
C	-0.02861196368715	0.14226748736038	-0.25438691023046
O	0.02917690189452	0.20456101059696	0.87674186711502
C	-0.05833331699430	-1.15110586453745	-3.94238709981301
O	0.00624938878693	-2.06114797341989	-3.26806560707154
Dimer 3	x	y	z
C	0.33269802910679	-0.27970796365053	-0.42781900490899
O	0.22589212548614	-0.11896432978238	0.69006372841763
C	-2.77905130484776	1.47739207659477	-2.53763134041904
O	-2.08999886745526	1.87256599749566	-1.72746787668853
Dimer 4	x	y	z
C	-0.46825007893992	0.20316684833911	-0.60019754337303
O	-0.47660149193020	0.25745548182980	0.53294588147191
C	3.05170157807967	-1.08533323930954	-0.35691671835964
O	3.01979134766368	-2.21624085850747	-0.43999546289307

Table 5.A.3: Cartesian coordinates of dimer geometries.

5.B Bibliography

[1] RW Wilson, KB Jefferts, and AA Penzias. Carbon monoxide in the orion nebula. *The Astrophysical Journal*, 161:L43, 1970.

[2] BT Soifer, RC Puetter, RW Russell, SP Willner, PM Harvey, and FC Gillett. The 4-8 micron spectrum of the infrared source W33A. *The Astrophysical Journal*, 232:L53–L57, 1979.

[3] SA Sandford, LJ Allamandola, AGGM Tielens, and GJ Valero. Laboratory studies of the infrared spectral propertries of CO in astrophysical ices. *The Astrophysical Journal*, 329:498–510, 1988.

[4] H. M. Cuppen, E. M. Penteado, K. Isokoski, N. van der Marel, and H. Linnartz. CO ice mixed with CH_3OH: the answer to the non-detection of the 2152 cm^{-1} band? *Monthly Notices of the Royal Astronomical Society*, 417(4):2809–2816, 11 2011. ISSN 0035-8711. doi: 10.1111/j.1365-2966.2011.19443.x. URL `https://doi.org/10.1111/j.1365-2966.2011.19443.x`.

[5] A.C. Adwin Boogert, Perry A. Gerakines, and Douglas C.B. Whittet. Observations of the icy universe. *Annual Review of Astronomy and Astrophysics*, 53(1): 541–581, 2015. doi: 10.1146/annurev-astro-082214-122348.

[6] Melissa K McClure, WRM Rocha, KM Pontoppidan, N Crouzet, Laurie EU Chu, E Dartois, T Lamberts, JA Noble, YJ Pendleton, G Perotti, *et al.* An ice age jwst inventory of dense molecular cloud ices. *Nature Astronomy*, pages 1–13, 2023.

[7] Akira Kouchi, Masashi Tsuge, Tetsuya Hama, Hiromasa Niinomi, Naoki Nakatani, Takashi Shimonishi, Yasuhiro Oba, Yuki Kimura, Sin-iti Sirono, Satoshi Okuzumi, *et al.* Formation of chiral CO polyhedral crystals on icy interstellar grains. *Monthly Notices of the Royal Astronomical Society*, 505(1):1530–1542, 2021.

[8] Akira Kouchi, Masashi Tsuge, Tetsuya Hama, Yasuhiro Oba, Satoshi Okuzumi, Sin-iti Sirono, Munetake Momose, Naoki Nakatani, Kenji Furuya, Takashi Shimonishi, *et al.* Transmission electron microscopy study of the morphology of ices composed of H_2O, CO_2, and CO on refractory grains. *The Astrophysical Journal*, 918(2):45, 2021.

[9] Jiao He, Francis E Toriello, Shahnewaz M Emtiaz, Thomas Henning, and Gianfranco Vidali. Phase transition of interstellar CO ice. *The Astrophysical Journal Letters*, 915(1):L23, 2021.

[10] JA Noble, E Congiu, F Dulieu, and HJ Fraser. Thermal desorption characteristics of CO, O_2 and CO_2 on non-porous water, crystalline water and silicate surfaces at submonolayer and multilayer coverages. *Monthly Notices of the Royal Astronomical Society*, 421(1):768–779, 2012.

[11] Scott A Sandford and Louis J Allamandola. The condensation and vaporization behavior of H_2O:CO ices and implications for interstellar grains and cometary activity. *Icarus*, 76(2):201–224, 1988.

[12] K Acharyya, GW Fuchs, HJ Fraser, EF Van Dishoeck, and H Linnartz. Desorption of CO and O_2 interstellar ice analogs. *Astronomy & Astrophysics*, 466(3):1005–1012, 2007.

[13] SE Bisschop, HJ Fraser, KI Öberg, EF Van Dishoeck, and S Schlemmer. Desorption rates and sticking coefficients for CO and N_2 interstellar ices. *Astronomy & Astrophysics*, 449(3):1297–1309, 2006.

[14] Lucas R Smith, Murthy S Gudipati, Rachel L Smith, and Robert D Lewis. Isotope effect on the sublimation curves and binding energies of ^{12}CO and ^{13}CO interstellar ice analogues. *Astronomy & Astrophysics*, 656:A82, 2021.

[15] Lorenzo Zamirri, Marta Corno, Albert Rimola, and Piero Ugliengo. Forsterite surfaces as models of interstellar core dust grains: computational study of carbon monoxide adsorption. *ACS Earth and Space Chemistry*, 1(7):384–398, 2017.

[16] Aurèle Germain, Marta Corno, and Piero Ugliengo. Computing binding energies of interstellar molecules by semiempirical quantum methods: Comparison between dft and gfn2 on crystalline ice. In *Computational Science and Its Applications–ICCSA 2021: 21st International Conference, Cagliari, Italy, September 13–16, 2021, Proceedings, Part V 21*, pages 632–645. Springer, 2021.

[17] Marc C. van Hemert, Junko Takahashi, and Ewine F. van Dishoeck. Molecular Dynamics Study of the Photodesorption of CO Ice. *Journal of Physical Chemistry A*, 119(24):6354–6369, jun 2015. ISSN 15205215. doi: 10.1021/acs.jpca.5b02611. URL `https://doi.org/10.1021/acs.jpca.5b02611`.

[18] G Molpeceres, V Zaverkin, N Watanabe, and J Kästner. Binding energies and sticking coefficients of H_2 on crystalline and amorphous CO ice. *Astronomy & Astrophysics*, 648:A84, 2021.

[19] GW Fuchs, HM Cuppen, S Ioppolo, C Romanzin, SE Bisschop, S Andersson, EF Van Dishoeck, and H Linnartz. Hydrogenation reactions in interstellar CO ice analogues-a combined experimental/theoretical approach. *Astronomy & Astrophysics*, 505(2):629–639, 2009.

[20] LJ Karssemeijer and HM Cuppen. Diffusion-desorption ratio of adsorbed co and co2 on water ice. *Astronomy & Astrophysics*, 569:A107, 2014.

[21] Trish Lauck, Leendertjan Karssemeijer, Katherine Shulenberger, Mahesh Rajappan, Karin I Öberg, and Herma M Cuppen. CO diffusion into amorphous H_2O ices. *The Astrophysical Journal*, 801(2):118, 2015.

[22] Ask Hjorth Larsen, Jens Jørgen Mortensen, Jakob Blomqvist, Ivano E Castelli, Rune Christensen, Marcin Dułak, Jesper Friis, Michael N Groves, Bjørk Hammer, Cory Hargus, Eric D Hermes, Paul C Jennings, Peter Bjerre Jensen, James Kermode, John R Kitchin, Esben Leonhard Kolsbjerg, Joseph Kubal, Kristen Kaasbjerg, Steen Lysgaard, Jón Bergmann Maronsson, Tristan Maxson, Thomas Olsen, Lars Pastewka, Andrew Peterson, Carsten Rostgaard, Jakob Schiøtz, Ole Schütt, Mikkel Strange, Kristian S Thygesen, Tejs Vegge, Lasse Vilhelmsen, Michael Walter, Zhenhua Zeng, and Karsten W Jacobsen. The atomic simulation environment—a python library for working with atoms. *Journal of Physics: Condensed Matter*, 29(27):273002, 2017. URL `http://stacks.iop.org/0953-8984/29/i=27/a=273002`.

[23] S. R. Bahn and K. W. Jacobsen. An object-oriented scripting interface to a legacy electronic structure code. *Comput. Sci. Eng.*, 4(3):56–66, MAY-JUN 2002. ISSN 1521-9615. doi: 10.1109/5992.998641.

[24] William C Swope, Hans C Andersen, Peter H Berens, and Kent R Wilson. A computer simulation method for the calculation of equilibrium constants for the formation of physical clusters of molecules: Application to small water clusters. *The Journal of Chemical Physics*, 76(1):637–649, 1982.

[25] MBBJM Tuckerman, Bruce J Berne, and Glenn J Martyna. Reversible multiple time scale molecular dynamics. *The Journal of Chemical Physics*, 97(3):1990–2001, 1992.

[26] Roger Fletcher. *Practical methods of optimization*. John Wiley & Sons, 2013.

[27] Herbert Edelsbrunner and Ernst P Mücke. Three-dimensional alpha shapes. *ACM Transactions On Graphics (TOG)*, 13(1):43–72, 1994.

[28] Frank Neese. The ORCA program system. *WIREs Computational Molecular Science*, 2(1):73–78, jan 2012. ISSN 1759-0876. doi: 10.1002/wcms.81. URL https://doi.org/10.1002/wcms.81.

[29] Frank Neese, Frank Wennmohs, Ute Becker, and Christoph Riplinger. The ORCA quantum chemistry program package. *Journal of Chemical Physics*, 152(22):224108, jun 2020. ISSN 10897690. doi: 10.1063/5.0004608. URL https://doi.org/10.1063/5.0004608.

[30] Stefan Grimme. Density functional theory with london dispersion corrections. *Wiley Interdisciplinary Reviews: Computational Molecular Science*, 1(2):211–228, 2011.

[31] Eike Caldeweyher, Sebastian Ehlert, Andreas Hansen, Hagen Neugebauer, Sebastian Spicher, Christoph Bannwarth, and Stefan Grimme. A generally applicable atomic-charge dependent London dispersion correction. *Journal of Chemical Physics*, 150(15), 2019. ISSN 00219606. doi: 10.1063/1.5090222.

[32] Stefan Grimme, Jens Antony, Stephan Ehrlich, and Helge Krieg. A consistent and accurate ab initio parametrization of density functional dispersion correction (DFT-D) for the 94 elements H-Pu. *Journal of Chemical Physics*, 132(15):154104, 2010. ISSN 00219606. doi: 10.1063/1.3382344. URL https://doi.org/10.1063/1.3382344.

[33] Oleg A. Vydrov and Troy Van Voorhis. Nonlocal van der Waals density functional: The simpler the better. *Journal of Chemical Physics*, 133(24):244103, dec 2010. ISSN 00219606. doi: 10.1063/1.3521275. URL https://doi.org/10.1063/1.3521275.

[34] Florian Weigend and Reinhart Ahlrichs. Balanced basis sets of split valence, triple zeta valence and quadruple zeta valence quality for H to Rn: Design and assessment of accuracy. *Physical Chemistry Chemical Physics*, 7(18):3297–3305, 2005. ISSN 14639076. doi: 10.1039/b508541a. URL http://dx.doi.org/10.1039/B508541A.

[35] Jingjing Zheng, Xuefei Xu, and Donald G. Truhlar. Minimally augmented Karlsruhe basis sets. *Theoretical Chemistry Accounts*, 128(3):295–305, 2011. ISSN 1432881X. doi: 10.1007/s00214-010-0846-z. URL https://doi.org/10.1007/s00214-010-0846-z.

[36] Germán Molpeceres and Johannes Kästner. Computational Study of the Hydrogenation Sequence of the Phosphorous Atom on Interstellar Dust Grains. *Astrophys. J.*, 910(1):55, 2021. ISSN 0004-637X. doi: 10.3847/1538-4357/abe38c.

[37] L. Martinez, R. Andrade, E. G. Birgin, and J. M. Martínez. PACKMOL: A package for building initial configurations for molecular dynamics simulations. *J. Comp. Chem.*, 30(13):2157–2164, 2009. ISSN 1096987X. doi: 10.1002/jcc.21224. URL https://onlinelibrary.wiley.com/doi/abs/10.1002/jcc.21224.

[38] Sebastian Spicher and Stefan Grimme. Robust Atomistic Modeling of Materials, Organometallic, and Biochemical Systems. *Angew. Chem. Int. Ed.*, 59(36):15665–15673, 2020. ISSN 15213773. doi: 10.1002/anie.202004239. URL https://onlinelibrary.wiley.com/doi/abs/10.1002/anie.202004239.

[39] Christoph Bannwarth, Sebastian Ehlert, and Stefan Grimme. GFN2-xTB—An Accurate and Broadly Parametrized Self-Consistent Tight-Binding Quantum Chemical Method with Multipole Electrostatics and Density-Dependent Dispersion Contributions. *J. Chem. Theory Comp.*, 15(3):1652–1671, mar 2019. ISSN 1549-9618. doi: 10.1021/acs.jctc.8b01176. URL https://doi.org/10.1021/acs.jctc.8b01176.

[40] John P. Perdew, Kieron Burke, and Matthias Ernzerhof. Generalized gradient approximation made simple. *Physical Review Letters*, 77(18):3865–3868, 1996. ISSN 10797114. doi: 10.1103/PhysRevLett.77.3865. URL http://www.ncbi.nlm.nih.gov/pubmed/10062328%5Cnhttp://link.aps.org/doi/10.1103/PhysRevLett.77.3865%5Cnhttp://link.aps.org/abstract/PRL/v77/p3865. ISBN: 9780596529321.

[41] Axel D. Becke. Density-functional thermochemistry. III. The role of exact exchange. *J. Chem. Phys.*, 98(7):5648–5652, 1993. ISSN 00219606. doi: 10.1063/1.464913. URL http://scitation.aip.org/content/aip/journal/jcp/98/7/10.1063/1.464913.

[42] Carlo Adamo and Vincenzo Barone. Toward reliable density functional methods without adjustable parameters: The PBE0 model. *J. Chem. Phys.*, 110(13):6158–6170, mar 1999. ISSN 0021-9606. doi: 10.1063/1.478522. URL https://doi.org/10.1063/1.478522.

[43] Axel D. Becke. A new mixing of Hartree-Fock and local density-functional theories. *J. Chem. Phys.*, 98(2):1372–1377, 1993. ISSN 00219606. doi: 10.1063/1.464304. URL https://doi.org/10.1063/1.464304.

[44] Yan Zhao and Donald G. Truhlar. The M06 suite of density functionals for main group thermochemistry, thermochemical kinetics, noncovalent interactions, excited states, and transition elements: Two new functionals and systematic testing of four M06-class functionals and 12 other function. *Theor. Chem. Acc.*, 120 (1-3):215–241, jul 2008. ISSN 1432881X. doi: 10.1007/s00214-007-0310-x. URL http://link.springer.com/10.1007/s00214-007-0310-x.

[45] Yan Zhao and Donald G Truhlar. Design of density functionals that are broadly accurate for thermochemistry, thermochemical kinetics, and nonbonded interactions. *J. Phys. Chem. A*, 109(25):5656–67, jun 2005. ISSN 1089-5639. doi: 10.1021/jp050536c. URL http://www.ncbi.nlm.nih.gov/pubmed/16833898.

[46] Narbe Mardirossian and Martin Head-Gordon. ωB97M-V: A combinatorially optimized, range-separated hybrid, meta-GGA density functional with VV10 nonlocal correlation. *J. Chem. Phys.*, 144(21):214110, jun 2016. ISSN 0021-9606. doi: 10.1063/1.4952647. URL https://doi.org/10.1063/1.4952647.

[47] Lorenzo Zamirri, Silvia Casassa, Albert Rimola, Mireia Segado-Centellas, Cecilia Ceccarelli, and Piero Ugliengo. Ir spectral fingerprint of carbon monoxide in interstellar water–ice models. *Monthly Notices of the Royal Astronomical Society*, 480(2):1427–1444, 2018.

[48] Jessica Perrero, Joan Enrique-Romero, Stefano Ferrero, Cecilia Ceccarelli, Linda Podio, Claudio Codella, Albert Rimola, and Piero Ugliengo. Binding energies of interstellar relevant s-bearing species on water ice mantles: A quantum mechanical investigation. *arXiv preprint arXiv:2209.07255*, 2022.

[49] Lorenzo Tinacci, Aurele Germain, Stefano Pantaleone, Stefano Ferrero, Cecilia Ceccarelli, and Piero Ugliengo. Theoretical distribution of the ammonia binding energy at interstellar icy grains: a new computational framework. *ACS Earth and Space Chemistry*, 2022.

[50] Martin Ester, Hans-Peter Kriegel, Jörg Sander, Xiaowei Xu, *et al.* A density-based algorithm for discovering clusters in large spatial databases with noise. volume 96, pages 226–231, 1996.

[51] Aurore Bacmann, Bertrand Lefloch, Cecilia Ceccarelli, Alain Castets, Juergen Steinacker, and Laurent Loinard. The degree of CO depletion in pre-stellar cores. *Astronomy & Astrophysics*, 389(1):L6–L10, 2002.

[52] Eric Keto and Paola Caselli. The different structures of the two classes of starless cores. *The Astrophysical Journal*, 683(1):238, 2008.

[53] Eric Keto and Paola Caselli. Dynamics and depletion in thermally supercritical starless cores. *Monthly Notices of the Royal Astronomical Society*, 402(3):1625–1634, 2010.

[54] S Cazaux, R Martín-Doménech, YJ Chen, GM Muñoz Caro, and C González Díaz. CO depletion: A microscopic perspective. *The Astrophysical Journal*, 849 (2):80, 2017.

[55] Rut M Berns and Ad van der Avoird. N_2–N_2 interaction potential from abinitio calculations, with application to the structure of $(N_2)_2$. *The Journal of Chemical Physics*, 72(11):6107–6116, 1980.

[56] MC van Hemert. Potential energy surface for the study of inelastic collisions between nonrigid co and H_2. *The Journal of Chemical Physics*, 78(5):2345–2354, 1983.

Chapter 6

Vibrational Energy Relaxation in Solid Carbon Monoxide

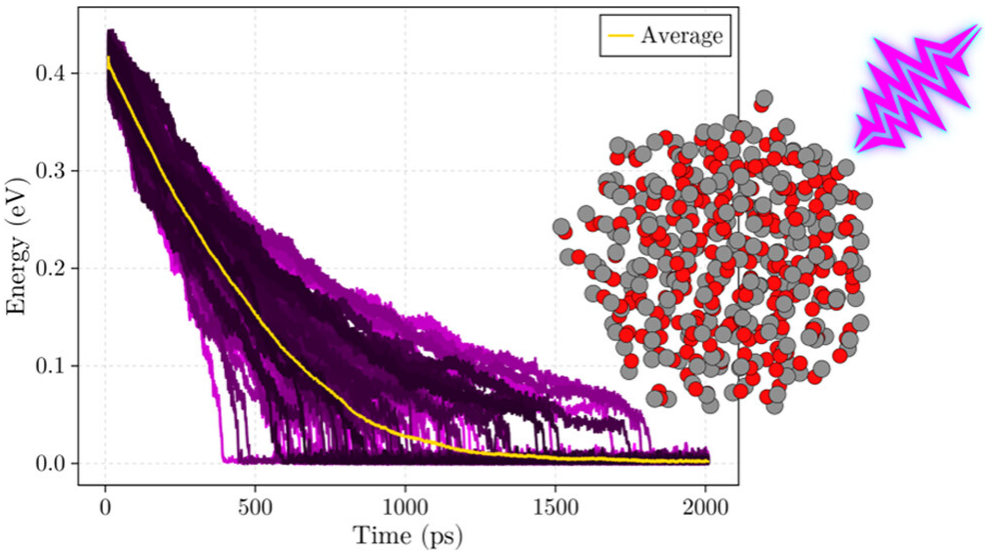

This chapter is based on:
Ferrari, B. C., van Hemert, M., Meyer, J., & Lamberts, T. (2024). Vibrational Energy Relaxation in Solid Carbon Monoxide. The Journal of Physical Chemistry C, 128(49), 21060-21072.

6.1 Abstract

Theory predicts vibrational energy relaxation (VER) in a dense medium exhibits an exponential dependence on the order of the multiphonon process (energy-gap law). Simply put, the vibrational energy decay rate (τ^{-1}) has an exponential dependence on the difference between the excited and accepting frequencies $\Delta\nu$ (frequency-gap law). Additionally, the vibrational density of states (VDOS) of the "bath" of low-frequency modes, into which vibrational energy is being dissipated, play a role in the VER. Although analytical studies at the quantum mechanical level for model systems have provided great insights, quantification of VER dynamics for systems described by realistic interaction potentials are still scarce. Here we focus on a simple diatomic molecule (carbon monoxide) to exclusively probe intermolecular VER without contributions from intramolecular vibrational energy redistribution. Using classical non-equilibrium molecular dynamics (NEMD) simulations we study VER within amorphous and crystalline clusters for mixtures of four different carbon monoxide isotopologues all described by two different interaction potentials. We also present a novel method for extracting $\tau(\Delta\nu)$ for trajectory ensembles of such NEMD simulations of weakly coupled molecules that have slow dissipation rates. For amorphous clusters, $\tau(\Delta\nu)$ is best described by a bi-exponential fit, whereas the situation is more complicated for crystalline clusters. In both cases we find links to the VDOS. Although the energy transfer occurs continuously in our classical simulations, further analysis of our trajectory ensembles suggests very interesting analogies to quantum mechanical descriptions of non-resonant and resonant vibrational to vibrational (V–V) energy transfer.

6.2 Introduction

An essential step in many chemical and physical processes in condensed phase is vibrational energy relaxation (VER).[1] For instance, an intermediate formed via an exothermic step may be vibrationally excited, and the VER rate or pathway may determine the subsequent step in the reaction.[2,3] Furthermore, vibrational energy transfer is essential for understanding energy flow in proteins[4,5], chemical reactions[6], molecular collisions[7,8], and between interfaces[9,10]. As such, an understanding of VER at the atomic scale is very important in physical and theoretical chemistry.

In pursuit of a theoretical framework for vibrational energy transfer, theoreticians initially turned to analogous radiationless transitions, such as, electronic relaxation.

Electronic relaxation has been shown to obey the energy gap law, which states that the transition probability has an exponential dependence on the energy gap between the two electronic states.[11] Nitzan *et al.*[12] derived an analogous expression for VER in a dense medium, where the VER rate exhibits an exponential dependence on the order of the multiphonon process. The order of the multiphonon process is given by the number of phonons that need to be created to accept the vibrational energy. In VER theory the energy-gap is more commonly expressed as a vibrational frequency-gap, as such, within this context its simpler to refer to it as the frequency-gap law.[13] Sun *et al.*[13] studied the vibrational lifetimes of the bending modes of hydrogen and deuterium defects in crystalline silicon and germanium through transient bleaching spectroscopy. They showed that the lifetimes obeyed the frequency-gap law and exhibited an exponential dependence on the decay order, validating the previously established theoretical framework. Tangentially, Kandratsenka *et al.*[14] carried out non-equilibrium molecular dynamics simulations of the VER of the two stretching and one bending modes HOD in D_2O. They found VER lifetimes of 2.7, 0.9 and 0.57 ps for the OH-stretch, OD-stretch and HOD bending respectively, where the OH-stretch has the largest frequency-gap from any accepting mode in D_2O (see FIG. 1 in their manuscript). This demonstrates that classical simulations can also reproduce the quantum mechanical principle of the frequency-gap law.

Despite the robustness of the frequency-gap law, there have been a few notable exceptions. Lüpke *et al.*[15] showed that two hydrogen defects (H_2^* and the di-vacancy defect HV · VH) within crystalline Si had VER lifetimes that differed by two orders of magnitude, despite having nearly identical frequencies. They speculated that the longer VER lifetime of the HV · VH defect arose from the larger spatial separation between the hydrogen and the surrounding silicon atoms. A few years later, West and Estreicher[16] studied the VER of a variety of hydrogen and deuterium defects (including those previously studied by Lüpke *et al.*[15]) in crystalline silicon with first principles molecular dynamics. They also found that certain defects deviated from the frequency-gap law, however, they attributed these deviations to the differences in local vibrational mode (LVM) coupling. In particular, they found the VER lifetime of the H_2^* defect was shorter than its deuterated counterpart (D_2^*). Upon closer inspection, they noted that the H_2^* defect was dissipating its vibrational energy into an LVM and a pseudo-local vibrational mode (pLVM), whereas, the D_2^* defect stretch mode was decaying into an LVM and a bulk phonon mode. They defined a pLVM as a localized mode with a frequency within the phonon continuum. Further analysis of other types of defects allowed the authors to conclude that the coupling between an LVM and

another LVM or pLVM was much stronger than the coupling between an LVM and bulk phonon modes. Additionally, Kohli *et al.*[17] studied the VER lifetime of the 1136 cm^{-1} vibration of oxygen defects in crystalline ^{28}Si and ^{30}Si. They found that the vibrational energy would decay into the symmetric-stretch of Si−O−Si, and the excess energy (the frequency difference between the donor and acceptor modes) would go into lattice modes. For cases where the excess energy was taken up by a single phonon they found that the VER lifetime would depend on the vibrational density of states (VDOS) constituted by the phonons at the frequency equal to the excess energy. In particular, the decay rate increases as the VDOS at the frequency equal to the excess energy increases. A better understanding of how LVM couplings and the VDOS can influence VER rates is necessary for a complete picture of VER theory.

In regard to CO, various pathways of vibrational energy transfer for a monolayer of ^{13}CO on an NaCl(100) surface have been investigated, with a particular focus on understanding the dynamics of vibrational energy pooling.[18–20] Vibrational energy pooling is possible because the lifetime for VER into the NaCl(100) surface is on the order of milliseconds, which is significantly larger than the time for vibrational to vibrational (V–V) energy transfer within the CO monolayer. The reason is that a large number of phonons are needed dissipate a CO stretch mode vibrational quantum, which in accordance with the energy-gap law will results in a long lifetime. Both resonant and non-resonant V–V energy transfer is relevant, i.e., the energy difference between the frequency levels of the donor and acceptor molecules being zero or non-zero, respectively. Corcelli and Tully[19] calculated the rate for resonant V–V energy transfer by assuming only a dipole–dipole coupling between parallel molecules, finding a (life-)time of 623 ps between individual resonant V–V energy transfer events. For the non-resonant V–V energy transfer from the donor molecule in a lower vibrational state pooling towards the acceptor already in a higher vibrational state, the excess energy must be taken up by a small number of phonons of the NaCl(100) surface. When only a single phonon is involved in the uptake, the corresponding lifetime varied between 1 μs and 10 ns, growing larger as the excess energy grew larger. They subsequently followed up this work with calculations of these same rates but for CO and for CO $\rightarrow$ ^{13}CO, where they found similar trends for the rates.[21]

Simulating VER in a molecular solid of a diatomic molecule (such as CO) allows us to ignore intramolecular energy redistribution, as well as constrain the number of available pathways for energy dissipation. For CO in particular, three main vibrational energy dissipation pathways are available; (i) resonant V–V energy transfer, (ii) non-resonant V–V energy transfer, and (iii) direct dissipation of vibrational energy into low-

frequency ("lattice") modes. Through isotopic substitutions we can probe the CO VER across a wide range of frequency-gap values. This allows us to scrutinize the frequency-gap law and analyze influence of the VDOS for the VER, whereby the latter aspect has never been studied in depth by dynamical simulations. Additionally, simulating the VER within amorphous and crystalline structures allows us to compare how an LVM couples to another LVM or a non-local (collective) vibrational mode. Within a crystalline CO ice the normal modes can be considered collective, consequently, isotopic substitution of the excited molecule will result in an isolated LVM. As such, VER simulations with crystalline CO allows us to study how LVM couplings affect the frequency-gap law.

We performed classical non-equilibrium molecular dynamics (NEMD) simulations of VER in solid carbon monoxide with four different isotopologues. We first show that the VER in our simulations traces the resonant (when the frequency-gap is near zero) and non-resonant V–V energy transfer pathways. Next we show how the VDOS influences the VER rate for amorphous and crystalline clusters. Finally, we discuss how the resonant V–V energy transfer is independent of isotopologue pairings, and is not restricted by the crystal structure.

6.3 Methods

All molecular dynamics simulations, data analysis and plotting was done using the Julia (version 1.9.0) programming language [22]. A variety of Julia packages were used; *Optim.jl* [23] (version 1.7.7) was used for optimizations, *LsqFit.jl* (version 0.15.0) was used for least square fittings, *FiniteDifferences.jl* (version 0.12.30) was used for calculating Jacobians, *DifferentialEquations.jl* [24] (subpackage *OrdinaryDiffEq.jl* version 6.54.0) was used for integrating the equations of motion for NEMD simulations, and *Makie.jl* [25] (subpackage *CairoMakie.jl* version 0.10.8) was used for plotting. Fast Fourier transforms (FFTs) were carried out using Julia bindings for the FFTW [26] library. Delaunay triangulations (used for calculating α-shapes) were carried out using a Julia wrapper for the Qhull [27] code.

The Jacobian used for calculating harmonic frequencies was found using a central finite difference method with 7 points (1 center point and 6 displaced points). The α parameter for the α-shape was optimized by minimizing the surface-area to volume ratio, with constraints that all points be included in the set of kept simplexes and the unique edges are a non-empty set.

We carried out molecular dynamics simulations with two different CO potentials;

a site–site interaction potential[28] and a permutation invariant polynomial neural network (PIP–NN) potential[29]. Both potentials are pair–potentials which do not include many-body effects, however, we have recently shown that for CO the many-body contributions beyond pair interactions account for less than 2% of the total interaction energy.[30] The PIP–NN potential was fit to *ab initio* data calculated with a smaller (extrapolation of double and triple zeta) basis set than what was used to fit the site–site potential (quadruple zeta), resulting in a reduction of the cohesive energy (consequently reducing the density) in the PIP–NN potential. The potential energy surface (PES) explored in the site–site potential was based on a smaller number of geometries than in the PIP–NN potential. The difference lies mainly in the smaller number of different intranuclear distances considered for the site-site potential. Recently, the reliability of the site–site potential to accurately simulate high-vibrational energy ($\nu = 40$) dynamics was brought into question.[31] Also, Chen *et al.*[29] state that their couple-cluster-based training data allows their potential to cover the lowest 33 vibrational states of the CO monomer reliably. As such, we limit the energy used for vibrational excitation in our simulations to less than 1 eV where we expect both potentials to give fully reliable results. We also note that the computational cost of the PIP–NN is more than an order of magnitude larger than the site–site potential.

Amorphous clusters were grown using an in-house "hit-and-stick" algorithm, similar to our previously used cluster growing scheme.[30] Here, we replace the optimization cycle with an NVT cycle, which employed the velocity rescaling thermostat (with a 100 fs time constant)[32]. For all NVE and NVT simulations herein the equations of motion were integrated with the velocity Verlet algorithm[33,34], using a 1 fs timestep (unless otherwise stated). We grew clusters using cycles of 5 ps for each simulation type, with the incoming molecule having 10 K translation energy directed at the center of mass of the cluster. We grew clusters of various sizes and did preliminary checks on the influence of the cluster size on the VER (see Appendix), but noted very little influence so we opted for a size of 250 molecules. Crystalline clusters were made by taking a spherical cut from the center of our previously used α–phase CO (α–CO) crystal; an 864 molecule α–CO cluster.[30] The space group and lattice parameters for our α–CO cluster are taken from literature.[35,36] The spherical cut was done with radius 13.75 Å, and isolated surface molecules were removed until the total cluster size was 250 α–CO molecules. The crystalline cluster was optimized, once with each potential, with a convergence criteria of 1×10^{-6} gradient norm. Crystalline order is unperturbed up to $\sim$ 10 Å from the center of the cluster, and no particular Miller-indices were favored for surface termination. Finally, we ran a 20 ps NVT simulation

with 10 K temperature. After preparing the clusters, we ran a 30 ps NVE simulation where a snapshot of the cluster was taken every 1.5 ps (20 total snapshots). These cluster snapshots are used to increase the variety of starting conditions to improve our statistical sampling. Isotopic substitutions for the cluster or excited molecule are done prior to the dissipation simulation.

To ensure proper statistical sampling for the energy dissipation studies, 100 trajectories have been calculated by general initial conditions in the following way: First, we randomly choose one of the 20 snapshots, then we calculate its α-shape to distinguish surface and bulk molecules. After that, we randomly select a molecule within the desired region, if applicable, we swap the mass of the selected molecule or of the cluster and then run a 10 ps NVE simulation to equilibrate the system. The selected molecule is subsequently excited to a specific vibrational energy by increasing the momenta of its atoms along the eigenvector of the mass weighted Hessian (calculated as an isolated molecule). A 1.5 or 2 ns (depending on the potential used) NVE simulation is carried out to monitor the VER of the excited molecule.

We study the VER of four different isotopologues, $^{12}C^{16}O$ (referred to simply as CO), $^{13}C^{16}O$, $^{12}C^{18}O$, $^{13}C^{18}O$, within clusters composed exclusively of one of these isotopologues. We adopt the following naming convention Excited–phaseCluster; where Excited is the isotope of the excited molecule, phase is the structural phase of the cluster (am = amorphous; cry = crystalline), and Cluster is the isotope of the cluster molecules. For example, CO–amCO denotes an excited $^{12}C^{16}O$ molecule within an amorphous $^{12}C^{16}O$ cluster.

We calculate the radial distribution of clusters by taking the distances between the center-of-mass of CO molecules. Similarly, we use the angle between CO molecular axes for calculating the angular distribution of clusters. We evaluate the degree of delocalization of each CO-stretch mode through the inverse participation ratio (IPR)

$$\rho_i = \frac{(\vec{u}_i \cdot \vec{u}_i)^2}{(\sum_j^N \vec{u}_j \cdot \vec{u}_j)^2} \quad . \tag{6.1}$$

Here $N = 250$ is the number of molecules in each cluster. The ($6N$ =) 1500-dimensional displacement vector $\vec{u}$ associated with the CO-stretch mode of each molecule is obtained from the harmonic frequency calculations. $\vec{u}_j$ denotes the six components describing the displacements of molecule j for this particular normal mode. For each CO stretch mode, we calculate the number of participating molecules for this mode by counting all ρ_i values larger than $\frac{1}{250^2}$. Here, $\rho_i = \frac{1}{250^2}$ corresponds to all molecules participating equally, ie., perfect delocalization of this mode, whereas for $\rho_i = 1$ the

mode is fully localized on a single CO molecule. The number of participating molecules is calculated for all CO stretch normal modes across all snapshots, resulting in $250 \cdot 20 = 5000$ values for each configuration (potential and cluster type).

Following a similar methodology as previously used[37], we calculate the vibrational coupling parameter between pairs of CO molecules. The vibrational coupling parameter (β)[38] is given by

$$\beta = \frac{\partial}{\partial r_\nu} \ln(V + 2\epsilon) \quad , \tag{6.2}$$

where V is the intermolecular interaction potential, ϵ is the well depth (preventing the argument of the logarithm to become negative), and $\frac{\partial}{\partial r_\nu}$ is the partial derivative with respect to the vibrational mode. Here we use the dimer well depth calculated using the PIP–NN potential ($\epsilon = 130$ cm^{-1}). In order to sample a distribution of coupling parameters relevant to our VER simulations we sample pairs of CO molecules within the bulk of a cluster at 200 different timesteps of an NVE simulation. Pairs of CO molecules were selected by taking molecules with centers of mass less than 4 Å apart.

The vibrational density of states (VDOS) of clusters was obtained by making use of the velocity autocorrelation function (VACF). For each snapshot (20 per cluster type) we ran a 75 ps NVE with 1 fs timestep, from this trajectory we calculated the VACF across 15 ps windows ($5 * 20 = 100$ total VDOS). We normalized the VACF, then applied a von Hann window[39], 8 factor zero-padding, and mirroring. An FFT was then carried out to produce a VDOS, and finally all 100 VDOS were averaged to a single VDOS.

We investigate energy interconversion by taking the average vibrational, translational and rotational energy per non-excited molecule, then further averaged across the 100 trajectories. The vibrational energy is calculated by taking both the intramolecular potential energy and the kinetic energy component of vibrational motion, whereas rotational and translation energies do not include their potential energy counterparts.

6.4 Structural and Vibrational Properties

Table 6.1 compiles the vibrational frequencies of all isotopologues as isolated molecules in the gas phase, using both interaction potentials under the harmonic approximation. While the absolute frequencies differ from experimental ones, the calculated frequency-gap $\Delta\nu$ relative to CO is at most 3 cm^{-1} off from the corresponding experimental frequency gap values. In the context of the VER simulations carried out in our work, the frequency-gap holds significantly more importance than the absolute frequencies. As

Table 6.1: Gas-phase vibrational frequencies (cm^{-1}) of the four isotopologues used in this study and their shifts $\Delta\nu$ (cm^{-1}) with respect to CO. For both potentials the frequencies are calculated from isolated molecules *in vacuo*, and using the harmonic approximation. The experimental values are gas-phase measurements.

Isotopologue	Site–Site		PIP–NN		Experiment [40]	
	ν	$\Delta\nu$	ν	$\Delta\nu$	ν	$\Delta\nu$
CO	2196	0	2169	0	2139	0
^{13}CO	2148	48	2121	48	2092	47
C^{18}O	2143	53	2116	53	2088	51
^{13}C^{18}O	2094	102	2067	102	2040	99

such, the worse agreement between absolute theoretical and experimental frequencies is not expected to be a significant source of error in the VER simulations.

In the top two panels of Figure 6.1 the radial (left) and angular (right) distributions of the amorphous and crystalline clusters are shown based on the site–site potential. All features are qualitatively identical also for the PIP–NN potential (see Appendix). As expected, the radial distribution for the crystalline clusters shows increased short-range ordering (see also Karssemeijer *et al.* [41]), whereas the long-range component is in better agreement with the amorphous distribution due to less well-ordered surfaces dominating the former at long distances. The sharpest contrast between the two structures is seen in the angular distributions, where the crystalline distribution shows two distinct peaks centered at 11 and 109 degrees. Distributions of the number of participating molecules per vibrational mode for crystalline and amorphous clusters is shown in the bottom panel of Figure 6.1. The crystalline distribution is trimodal with one peak being more non-local than the amorphous distribution, although it still contains a strongly localized peak because of the lack of periodic boundary conditions.

Figure 6.2 shows the low frequency vibrational density of states (VDOS) for a crystalline and amorphous CO cluster with both the site–site and PIP–NN potentials. The low frequency component of the VDOS is not significantly affected by the cluster isotopologue, as such, we only show the VDOS of CO clusters. It is worth discussing the differences in the low frequency modes predicted by each potential, however, an in-depth discussion and highly accurate phonon band are beyond the scope of this paper. Both potentials yield broad Lorentzian bands centered around 35 cm^{-1} for amorphous clusters, with the PIP–NN potential having a slightly longer tail. These are in good agreement with experiments that observe a broad Lorentzian band centered at 50 cm^{-1}.[42] For the crystalline clusters the two vibrational spectra are more different, however, they both still exhibit two distinct peaks at roughly 45 cm^{-1} and 80 cm^{-1}.

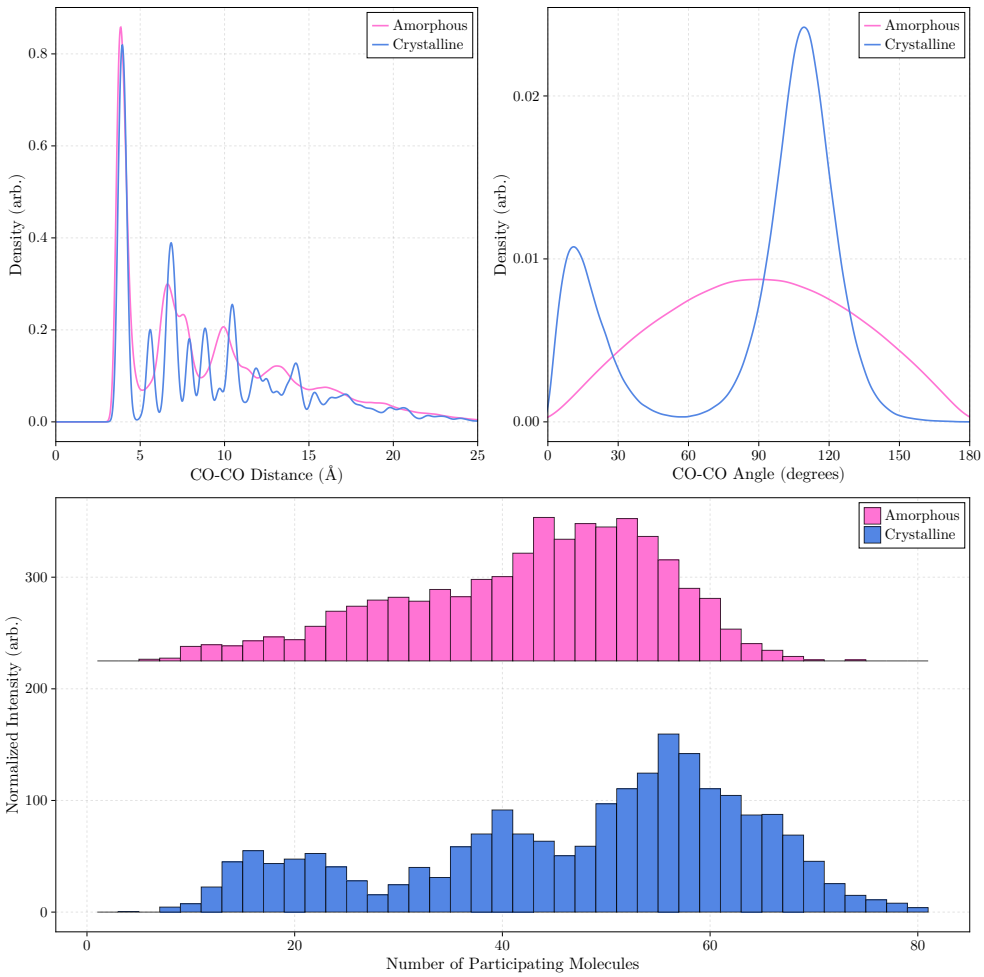

Figure 6.1: Comparison of geometric and vibrational properties from 10 K clusters made using the site–site potential. Top Left: radial distribution of CO molecules in amorphous (pink) and crystalline (blue) clusters. Top Right: angular distribution between CO molecules in amorphous (pink) and crystalline (blue) clusters. Bottom: number of participating molecules for the CO stretch vibrations in amorphous (pink) and crystalline (blue) clusters. The amorphous distribution is offset by 225 for visual clarity.

In close agreement with THz measurements of α-CO, which show one peak centered at 50 cm^{-1} and another at 80 cm^{-1}.[43]

A distinct difference in the two potentials is the sharp peak towards 0 cm^{-1} for the crystalline cluster using the PIP–NN potential. Peaks at 0 frequency are usually caused by so-called "bias" in the "signal" that undergoes the Fourier transform step in the

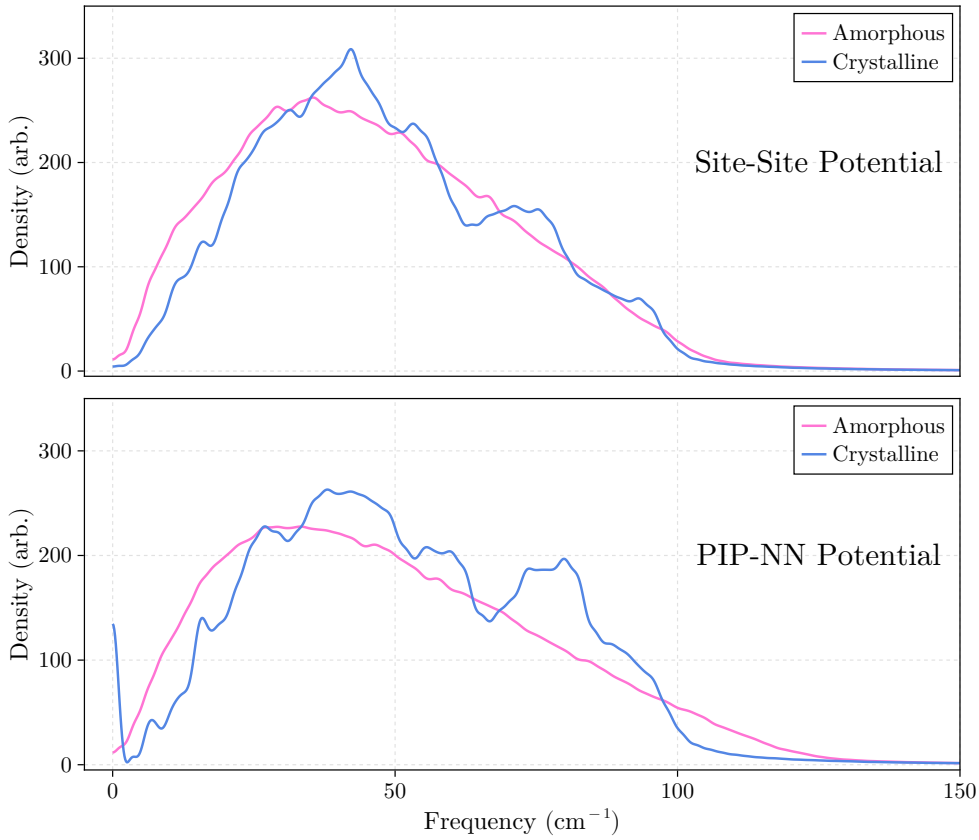

Figure 6.2: Low-frequency part of the vibrational density of states (VDOS) of amorphous (pink) and crystalline (blue) CO clusters with (top) the site–site potential and (bottom) the PIP–NN potential.

VACF calculation. In all spectra shown here this has been dealt with by subtracting the mean from the signal, however, for some of the crystalline clusters with the PIP–NN potential a bias remained. A source of bias that is not fully removed by the aforementioned procedure is cluster restructuring towards a different local minimum. Where the conversion of potential energy into kinetic energy can result in a bias in the VACF signal not equal to the signal mean. Peaks caused by bias in the signal typically have the largest density, since the observed peak is not the largest it means only a few trajectories used to calculate the VDOS present restructuring. Since our results are taken from the ensemble average of 100 trajectories, any influence of restructuring on the VER will be negligible in the ensemble average. As such, we do not suspect it to

have caused any differences in the results of the PIP–NN potential as compared with the site–site potential.

The structural and vibrational properties shown in Figures 6.1 and 6.2 display the key differences between the two clusters types, and any differences in the VER between amorphous and crystalline clusters must be explained by one of these differences.

6.5 Analyzing Vibrational Energy Relaxation with Classical Dynamics

6.5.1 Trajectory Ensembles

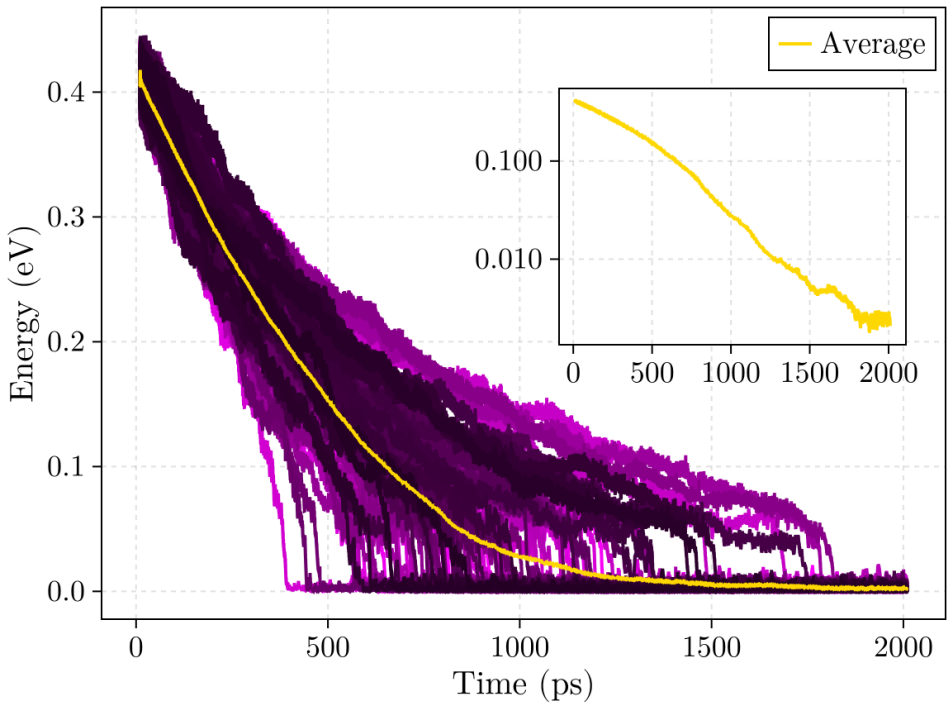

Figure 6.3: Vibrational energy dissipation for CO–amCO simulations with the site–site potential. All 100 trajectories are shown in purple, and the average of them is shown in gold. Inset plot shows only the average energy decay with the a logarithmic y-axis.

All results discussed herein are ensemble averages of 100 trajectories, as shown by Figure 6.3. Individual trajectories (purple lines) generally show very similar shapes,

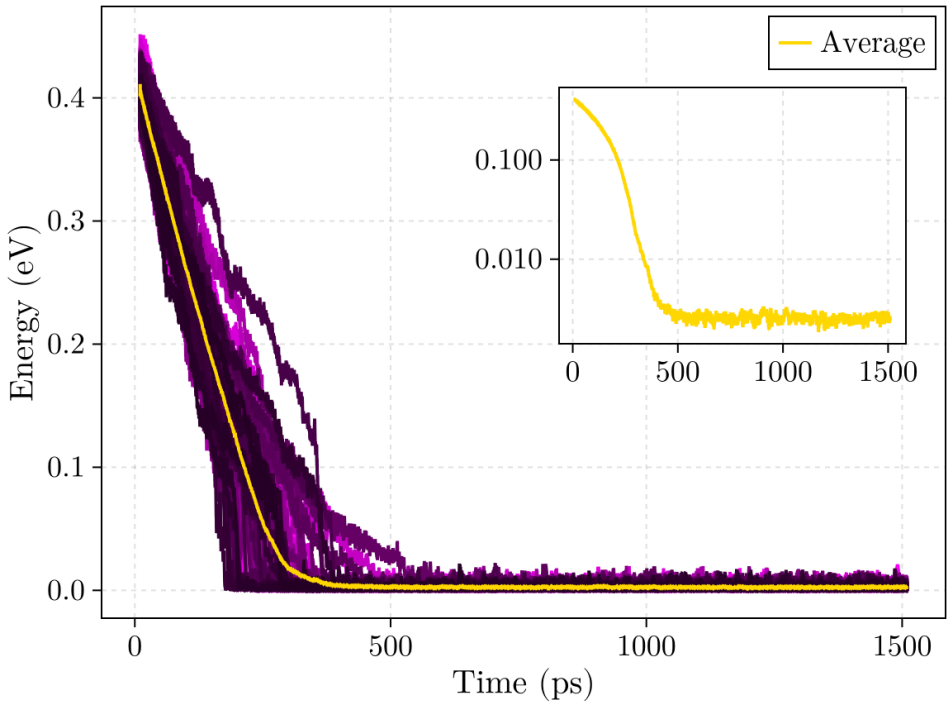

Figure 6.4: Same as Figure 6.3 but using the PIP–NN potential.

however, there is a broad range of lifetimes (spanning roughly 500 to 1500 ps). Their average (gold line) is used to determine the time dependent vibrational decay rates. Figure 6.3 shows the results of simulations for CO–amCO using the site–site potential, Figure 6.4 is the equivalent plot for the corresponding configuration obtained with the PIP–NN potential. In both cases, these trajectories are for "self-dissipation", i.e., an isotope within a cluster of the same isotope, which results in a resonant energy transfer event at low energies (*vide infra*). In the Appendix another representative example is provided for CO–cryCO (using the site–site potential).

Across all simulations, the PIP–NN potential produces faster relaxation rates than the site–site potential. To better understand how the vibrational coupling differs in each potential, we calculated the vibrational coupling parameter between neighboring CO molecules. Figure 6.5 shows the kernel density estimation of the distribution of vibrational coupling parameters found for each potential. The average vibrational couplings are -0.0156 a_0^{-1} for the site–site potential, and -0.0218 a_0^{-1} for the PIP–NN, which is in agreement with the shorter relaxation lifetimes observed with the PIP–NN

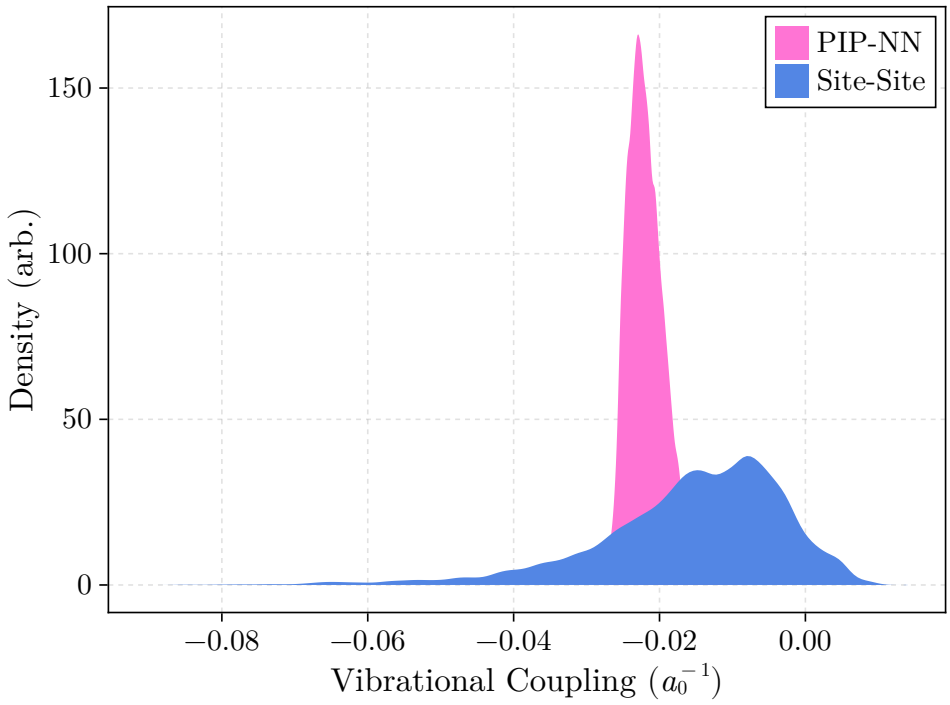

Figure 6.5: Vibrational coupling parameter for pairs extracted from amorphous clusters.

potential. Furthermore, the site–site potential produces a much broader distribution of couplings than the PIP–NN potential. This is reflected in the broad range of VER lifetimes seen across the 100 trajectories using the site–site potential (see Figure 6.3) compared to the trajectories using the PIP–NN (see Figure 6.4).

6.5.2 Frequency Shift

For diatomic molecules described by intramolecular Morse potentials, the excited frequency for a given excitation energy is given by[44]

$$\nu^\star = \nu_\circ \sqrt{\frac{D-E}{D}} \quad , \tag{6.3}$$

where $\nu^\star$ is the excited frequency, $\nu_\circ$ is the frequency of classical small vibrations, D is the dissociation energy and E is the vibrational energy. Since this equation was derived for a single Morse potential, it does not include many-body effects resulting

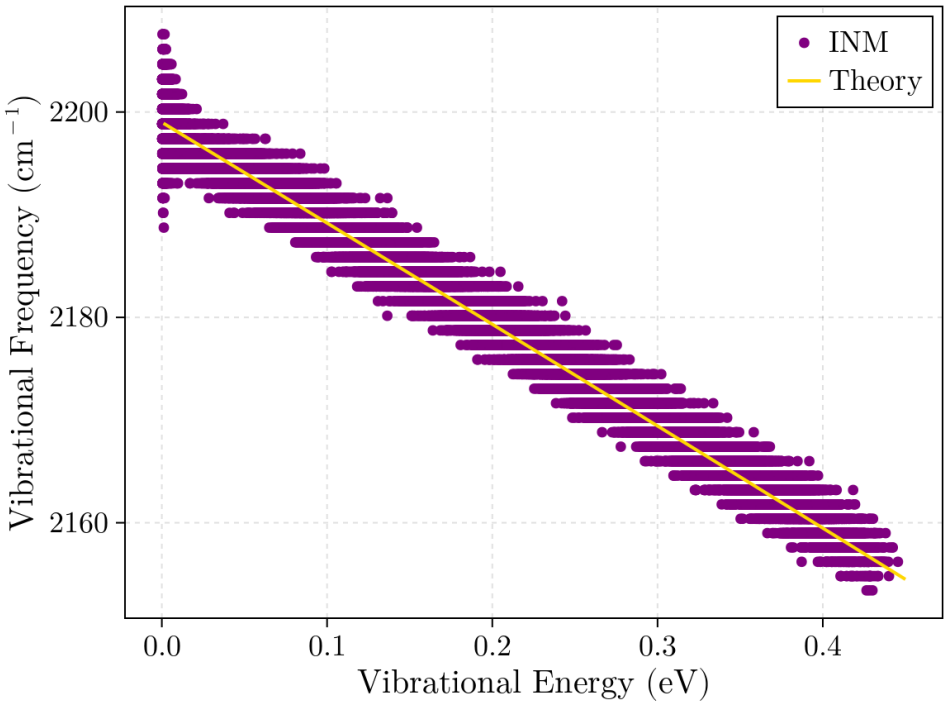

Figure 6.6: INMs (purple dots) of an excited CO molecule within an amorphous $(CO)_{250}$ cluster versus the vibrational energy of the excited molecule. The predicted excited frequency for given a vibrational energy is shown in gold (see Equation (6.3)). All data from 100 trajectories using the site–site potential are shown.

from intermolecular interactions. To confirm this holds for a molecule within a cluster, we calculate the instantaneous normal mode (INM) of the excited molecule including the interactions with all other molecules at every picosecond of the simulation. The INMs were calculated by running a short NVE simulation (50 fs with 0.01 fs time step) at each picosecond, then taking the bond length of the excited molecule during this NVE. This bond length array was then sliced between the first three turning points (one full wave), then repeated 1000 times and run through an FFT algorithm to get the INM of the excited molecule. Figure 6.6 shows the INMs (purple dots) of the excited molecule (across all 100 trajectories of the CO–amCO simulations) across the full simulation, as well as the predicted frequency shift based on Equation (6.3) (gold line). For the predicted frequency shift $\nu_\circ$ was set as the mean INM (roughly 2199 cm^{-1} for Figure 6.6) after the vibrational energy had equilibrated with the cluster. A

range of frequencies per vibrational energy is observed in the INMs due to the large configurational space sampled.

Excellent agreement between the predicted frequency and the calculated INMs reveals that intermolecular contributions are negligible in the frequency shift of excited CO. The PIP–NN potential also yields a perfect agreement between predicted frequency and calculated INM. As such, we can calculate the INM of our ensemble average (*vide infra*) by using Equation (6.3) with $\nu_\circ$ set to the mean INM of the excited molecule prior to excitation. We can then calculate the instantaneous frequency-gap

$$\Delta\nu = \nu^\star - \nu_{\text{clu}} \quad , \tag{6.4}$$

where ν_{clu} is the mean frequency of the cluster. In this formalism a negative frequency-gap implies an excited molecule frequency lower than that of the cluster frequency.

6.5.3 Frequency-Gap Dependent Decay Rate

A consequence of the frequency-gap law is a non-exponential decay in the slow regime, where the VER is slow enough to allow the decay rate to change as the frequency changes. Goldstein and Bialek[45] derived an expression for radiationless transitions in the slow regime, and found that the decay rate may increase or decrease over the course of the transition. This is particularly important for classical simulations where the frequency of the excited molecule shifts (shifting the frequency-gap) during the dissipation process, resulting in a non-constant decay rate. Zhang *et al.*[46] speculated that this phenomenon was occurring in the VER of DF in CD_2Cl_2, more specifically, as the DF dissipated its energy the vibrational frequency red-shifted resulting in less spectral overlap with the solvent. When they fit an exponential to the first 5 ps of the time evolution of the vibrational energy they found a time constant of 7.6 ps, whereas, fitting the full time evolution gave a time constant of 8.8 ps. For systems with strongly coupled excited and accepting modes the variation in the decay rate is negligible and a typical exponential decay is still produced. This is not the case for the CO clusters studied here, where the coupling is weak and the variation in the decay rate is quite large. Consequently, fitting an exponential decay to the time evolution of the original excitation extracted from our NEMD simulations is insufficient, and we have developed a new procedure instead. Below we describe our procedure for calculating pseudo-instantaneous decay rates.

For short timescales the frequency-gap shift is negligible, which in turn results in a nearly constant decay rate. As such, within short timescales the vibrational energy

decay can be fit with the typical exponential decay function

$$E(t) = E_{\circ} e^{-\frac{t}{\tau}} \quad , \tag{6.5}$$

where $E_{\circ}$ is the initial excitation energy, τ is the decay time constant and t is the simulation time. Note, the decay time constant is a pseudo-instantaneous value related to the time dependent vibrational decay rate. As such, it should not be confused with typical exponential lifetimes found by fitting across the full simulation time. To get the decay time constant as a function of simulation time we employed a fitting procedure analogous to the Savitzky-Golay filter[47] algorithm. We fit a standard exponential (Equation (6.5)) to successive adjacent subsets (of length N) of the energy decay, where each new subset differs by only 1 data point (corresponding to 1 fs in the simulation time). The fitted decay time constant is then attributed to the time corresponding to the first data point in the subset. When the standard error in the decay time constant became larger than 5% of the fitted decay time constant the algorithm was terminated and no new subsets were included in the fitting procedure. The only variable parameter in this method is the subset length (N), which if set too large (or too small) would result in large oscillations of the decay time constant. We carefully selected the length to reduce the oscillations, and in general found values between 400 and 850 to be ideal.

6.6 Results and Discussion

6.6.1 Amorphous Cluster

Figure 6.7 shows the decay time constant as a function of the frequency-gap between the excited molecule and the amorphous cluster for both potentials. Both potentials produce similar frequency-gap dependencies, where τ increases as the frequency-gap increases. Across the entire frequency-gap range we studied, the site–site potential produces larger τ values compared to those produced by the PIP–NN potential. Inline with our findings that the PIP–NN potential has a stronger average coupling strength (see Figure 6.5) for vibrational modes. Unlike the site-site potential the PIP–NN potential does not allow to decompose these couplings into contributions from different interactions. In fact, the total energies from the quantum chemical calculations, which it has been fitted against, do not feature such a decomposition. Electrostatic interactions typically represent the strongest portion of vibrational coupling, however, in the case of CO its the weakest contribution to the intermolecular interaction in the

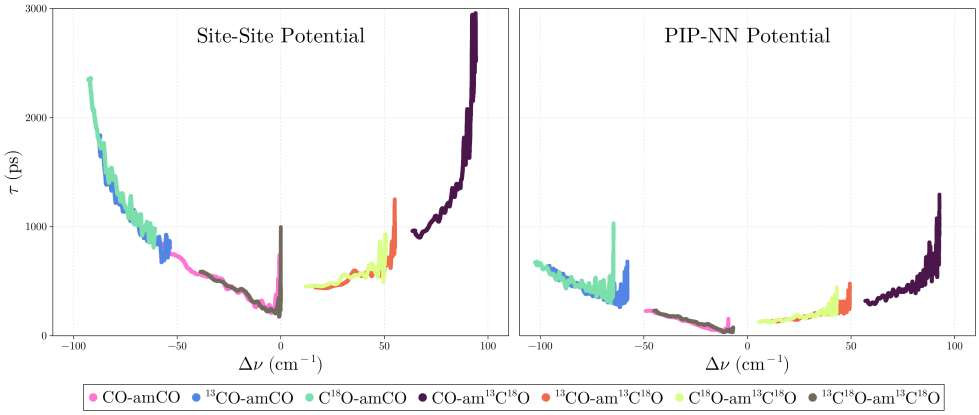

Figure 6.7: Vibrational energy decay time constant as a function of frequency-gap for amorphous clusters using the site–site potential (left) and the PIP–NN potential (right). Various isotopologue configurations are included in the figure, where the isotopologue-induced frequency shifts help cover a larger frequency-gap range. A larger excitation energy (0.6 eV) was used for the CO-amCO case (pink) in the site–site potential, which results in a larger frequency gap range than other curves. The frequency-gap was calculated through the excited molecules vibrational energy, as explained in Section 6.5.2. The $^{13}C^{18}O$-amCO case was excluded from the plot due to the decay time constant produced by both potentials being extremely large.

site–site potential.[30] This should be consistent within the PIP–NN training set data, nevertheless, the PIP–NN potential clearly exhibits an enhanced vibrational coupling when compared with the site–site potential.

Despite the faster VER with the PIP–NN potential, both potentials provide qualitatively similar results. An offset between the curves for negative and positive frequency gaps is seen in Figure 6.7 for both potentials, indicative of an enhancement of the VER rate when the excited frequency is lower than the accepting mode frequency. The magnitude of the offset diminishes as the frequency-gap increases, with decay time constants at gaps above 50 cm^{-1} being essentially equal to their negative counterparts. Incidentally, this is also where the excited molecule is a different isotopologue compared to the cluster; making it possible that this enhancement is not inherent to the sign of the frequency gap, but rather due to the isotopic combinations. Following this logic, it would appear that the offset is a result of a different anharmonic coupling, possibly produced by the differing degrees of LVM character, between isotopologues.

With both potentials the decay time constant for $^{13}C^{18}O$-amCO was so large that the total energy dissipated was negligible across the total simulation time of 1.5 or 2 ns. This is in line with recent experimental findings that showed how vibrational energy

could be transported in the CO → $^{13}C^{18}O$ direction but the reverse was not possible.[48] However, the exact mechanism constraining the allowable direction of energy transfer in experiments is different compared to our simulations. In the experiments the lack of thermal energy sufficient enough to compensate the higher energy vibration of CO over $^{13}C^{18}O$ produces the constraint. In contrast, for our simulations this arises from the large frequency-gap producing an extremely weak vibrational coupling, resulting in a negligible energy transfer rate.

6.6.2 Crystalline Cluster

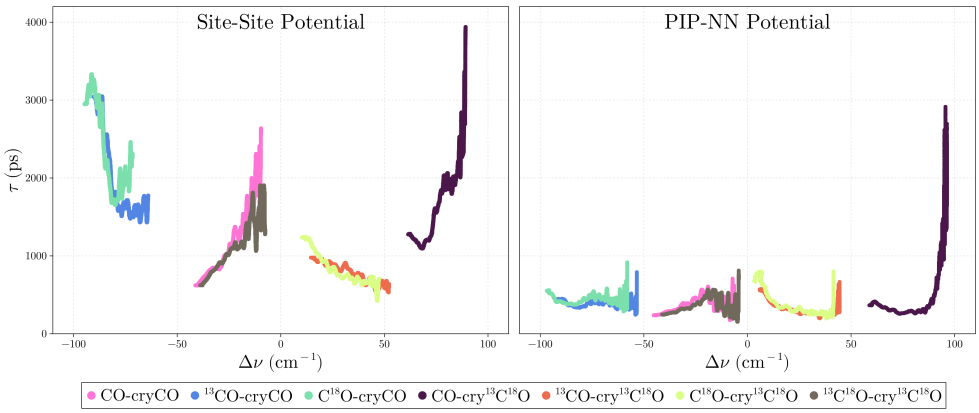

Figure 6.8: Same as Figure 6.7 but for crystalline clusters.

Figure 6.8 shows the decay time constant as a function of the frequency-gap between the excited molecule and the crystalline cluster using the site–site (left) and PIP–NN (right) potentials. As was the case for the amorphous clusters (see Figure 6.7), both potentials again produce similar trends with the PIP–NN having smaller τ values. Furthermore, both potentials produce very similar structures and distributions of participating molecules for both amorphous and crystalline clusters (see Figure 6.1 and Figure S3 in the Appendix). One peculiarity in the crystalline case is the asymmetry in the PIP–NN potential, where the CO–cry$^{13}C^{18}O$ simulation has a much stronger frequency-gap dependence.

Within the -50 to 50 cm^{-1} frequency-gap range the crystalline clusters exhibit a different frequency-gap dependence than the amorphous clusters. This is observed in both potentials, however, it is less drastic in the PIP–NN potential. Across the entire frequency-gap curve for each cluster configuration the degree of LVM–LVM

coupling is reduced, as such, changes localized to certain frequency-gap ranges are not directly resulting from the diminished LVM–LVM coupling. At small frequency-gaps the excited molecule couples strongly to a nearby molecule, and can even resonantly transfer vibrational energy. This resonance is not captured by the τ values in Figure 6.8 due to the resonant energy transfer (discussed in more detail in Section 6.6.5) not producing an exponential energy decay curve. As such, our methodology for producing frequency-gap dependent decay rates does not produce τ values at these frequency-gaps.

6.6.3 Analysis of Energy Redistribution

Although clearly not the goal of this study, it is instructive to do an order-of-magnitude comparison with what has been found for CO adsorbed on NaCl(100) before going into a more detailed analysis: In all configurations involving different CO isotopologues we studied, the VER lifetime is near the nanosecond regime. This is several orders of magnitude different from direct VER of a CO vibrational quantum into lattice modes – and thus indicative of V–V energy transfer rather than direct dissipation. On the other hand, the VER lifetime for converting one CO vibrational quantum into lattice modes of NaCl(100) and solid CO could be very different. For the resonant V–V energy transfer Corcelli and Tully [19] found a lifetime of 623 ps, which is fairly similar to the lifetime observed in our simulations. However, most of our simulations are with mixed isotopologues and thus do not meet the conditions required for resonant V–V energy transfer. For single-phonon non-resonant V–V energy transfer, Corcelli and Tully [19] obtained lifetime between 10 ns and 1 μs. Their quantum mechanical model assumes parallel CO molecules described as interacting dipoles. In contrast, our simulations are classical for non-parallel-oriented assemblies of CO molecules, and both interaction potentials go clearly beyond dipole-dipole interactions. The ensuing detailed analysis of the energy redistribution allows to better understand which energy transfer processes are (predominantly) described by our simulations.

Figure 6.9 shows the average energy gained per non-excited molecule during CO–amCO and CO-cryCO VER simulations with each potential, decomposed into kinetic and potential energy contributions of intramolecular vibrations (V) together with kinetic energy contributions of translations (T) and rotations (R). We only include simulations of CO VER within CO clusters since all other simulations for different isotopologue combinations (with both potentials) revealed similar trends.

Although not directly visible in Figure 6.9, we note in passing that the average total

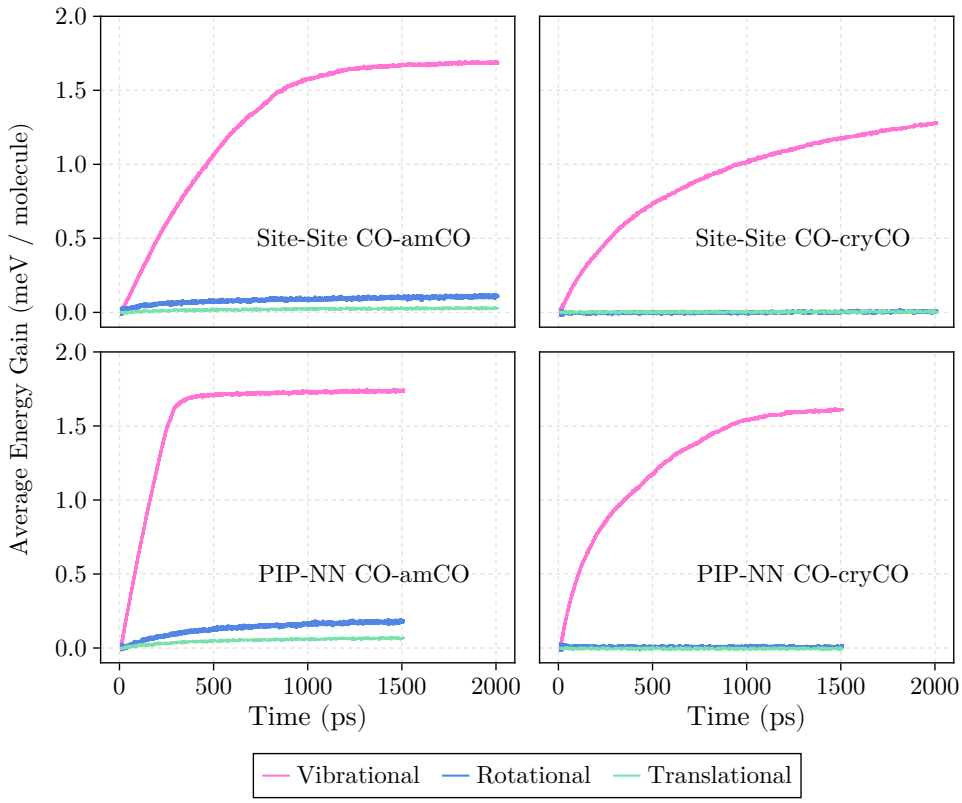

Figure 6.9: Average energy gained per molecule during a site–site CO–amCO (top-left), site–site CO–cryCO (top-right), PIP–NN CO–amCO (bottom-left), and PIP–NN CO–cryCO (bottom-right) simulation.

energy gained ($V + T + R$) is larger than the 0.4 eV excitation energy by 60 meV for the CO–amCO and 5 meV for the CO-cryCO clusters. We confirmed that the total energy is constant during each trajectory, hence, this is not a result of issues with the time integration algorithm of our NEMD simulations. Further analysis reveals that during the simulation potential energy is converted to translational or rotational kinetic energy due to structural reorganization, i.e. transition towards a different local minimum in the weakly bound clusters. The smaller average total energy gain for the crystalline clusters can be rationalized by the fact that they are intrinsically more stable: While molecules in the bulk of the amorphous clusters can contribute to the "minima hopping" by reorienting, only molecules at the edges of the crystalline clusters (can) do the same.

Most importantly, Figure 6.9 reveals that only a very small amount of the vibrational excitation is transformed into rotational and translational energy of the surrounding CO molecules. Since the latter constitutes the low-energy "lattice" modes of all clusters, our simulations are clearly not dominated by direct VER via multiphonon processes. In other words, the difficulty in converting high frequency vibrational energy into translational or rotational energy is consistent with the frequency-gap law. Instead, fractions of vibrational quanta are predominantly transferred to the vibrational stretch modes of the surrounding CO molecules, which can be seen as a realization of V–V energy transfer pathways within our classical simulations. In what follows we further analyze the non-resonant and resonant energy transfer pathways in our trajectory ensembles, whereby the former should also involve energy uptake by low-energy "lattice" modes.

6.6.4 Non-Resonant Energy Transfer

Originally motivated by the frequency-gap law, we have taken a bird's eye view at the data for the lifetimes τ presented in Figure 6.7 and attempted to fit exponential functions. Not (further) distinguishing between the different isotopologue combinations, the result for amorphous clusters (i.e., all the data included in Figure 6.7) is shown in Figure 6.10. Both a single exponential (pink) and a linear combination of two exponentials (blue) has been used, including a y-intercept constant since the τ data appears to have a non-zero asymptote. For positive frequency shifts ($\Delta\nu > 0$), it is clear that the bi-exponential fit is better than the one based on a single exponential for both interaction potentials over the entire range. For the negative frequency shifts ($\Delta\nu < 0$), the bi-exponential is favorable at least for the Site–Site Potentials at large $|\Delta\nu| > 80$ cm^{-1}. The best two exponential fit for the negative shifts using the PIP–NN potential is two half amplitude exponentials equal to the single exponential fit. As such, the two exponential fit is plotted over the single exponential (hence the lack of a pink line) fit for the bottom right panel of Figure 6.10.

If the frequency-gap law would provide a good description, only a single exponential should have been required for the fit, with the decay constant of this exponential reflecting the multi-phonon order of the direct dissipation process to low-frequency modes. Furthermore, we have also looked at the intersection points of the bi-exponentials (see Appendix): Focussing on $\Delta\nu > 0$, it is interesting to note that the intersection occurs at $\Delta\nu \approx 100$ cm^{-1} for both interaction potentials. It coincides with the tail of the VDOS for the low-frequency modes (see Figure 6.2 and decomposition

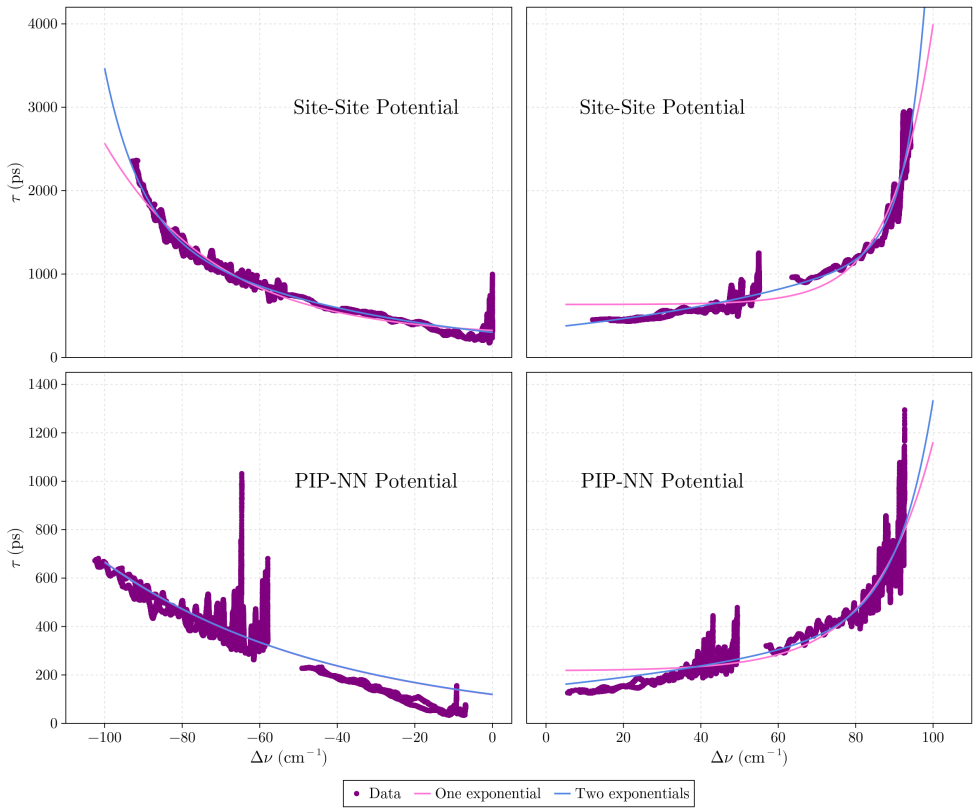

Figure 6.10: Least square fitting of the vibrational energy decay time constant as a function of frequency-gap for amorphous clusters using the site–site potential (top two panels) and the PIP–NN potential (bottom two panels). The data (purple) was fit with both a single exponential (pink) and a linear combination of two exponentials (blue).

into bulk and surface modes in the Appendix). In other words, as soon as the excess energy connected with $\Delta\nu > 0$ (see Equation (6.4)) does no longer "fit" to the energy equivalent of the maximum low-frequency mode, the $\tau(\Delta\nu)$ dependence changes. This is consistent with the non-resonant V–V energy transfer pathway suggested by energy redistribution analysis presented in the previous section: The quantum-mechanical expressions derived by Corcelli and Tully [19] for CO adsorbed on NaCl(100) result in a change of the $\tau(\Delta\nu)$ dependence when switching from one to two (or more) low-frequency mode (phonon) quanta during the non-resonant V–V energy transfer.

A similar bird's eye view on the data for the crystalline clusters shown in Figure 6.8 is complicated by the fact that τ decreases as the frequency-gap approaches

$|\Delta\nu| = 50$ cm^{-1}. It is interesting to note that this is roughly where both potentials produce a peak in the VDOS. In other words, the highest VER rate coincides with the highest density of phonon states, which is in line with the observations of Kohli *et al.*[17] for the VER of oxygen defects in crystalline silicon. Contrary to the crystalline clusters, both potentials produce the smallest τ values near zero frequency-gap despite the VDOS of the amorphous clusters peaking near 35 cm^{-1}. Decomposing the VDOS into contributions from only surface or bulk atoms, it turns out that the frequency range between 10 and 30 cm^{-1} is dominated by the surface for the crystalline clusters , whereas for the amorphous clusters the contribution from the bulk is much more pronounced in the same frequency range (see Appendix). Given that the excited molecule is within the bulk of the cluster, this disparity in bulk states could be responsible for the different behavior of the VER rate in the interval $|\Delta\nu|$ between ± 50 cm^{-1}.

6.6.5 Resonant Energy Transfer

As detailed in Section 4, none of the VER simulations underlying Figures 6.7 and 6.8 start with a zero frequency gap due to the anharmonic shift of the excited CO molecule. To deliberately make $\Delta\nu$ vanish at the beginning of the trajectories, we have run additional VER simulations for CO-am^{13}CO, Exciting the CO molecule by 0.6 eV of vibrational energy yields essentially the same vibrational stretch frequency as the average of ^{13}CO host cluster. Figure 6.11 shows all the trajectories (purple) and the average (gold), where its possible to see that for all trajectories the excited molecule loses roughly 0.2 eV in vibrational energy in the first 200 ps. Once the frequency mismatch becomes large again, i.e., the initial resonance condition is lost, the VER slows down significantly (see Figure 6.11).

We have observed the same resonant energy transfer phenomenon also in crystalline clusters (not shown). In both amorphous and crystalline it occurs in all 100 trajectories. This implies that it is independent of the cluster structure and thus the relative orientation of the CO molecules. Instead, it really only depends on the frequency mismatch. Furthermore, the average energy redistribution for the entire trajectory reveals that energy is dominantly transferred into the stretch vibrations of the neighboring molecules, in the same way as it is shown in Figure 6.9 - albeit much faster initially. Consequently, we interpret the initial parts of these simulations as classical manifestations of resonant V–V energy transfer, switching over to non-resonant V–V energy transfer during the remainder of the trajectories. The decay time constants on the order of ≈ 100 ps that we observe for the former is again consistent with the quantum

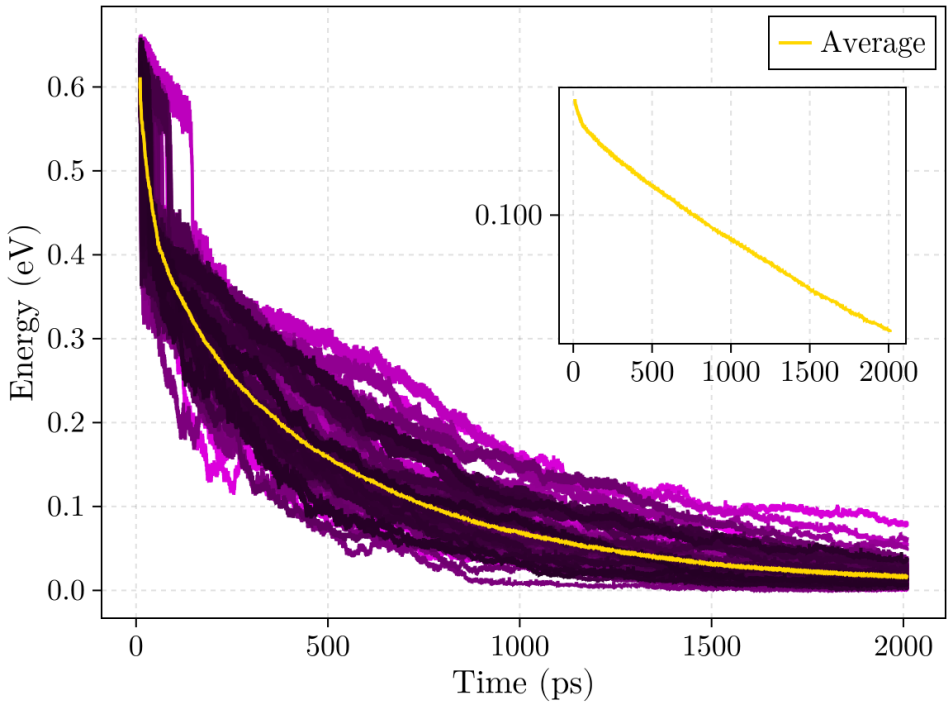

Figure 6.11: Same as Figure 6.3 but using the site-site potential for the CO-am ^{13}CO case with a 0.6 eV excitation energy.

mechanical description provided by Corcelli and Tully [19] for a CO film adsorbed on NaCl(100).

6.7 Summary and Outlook

We performed classical NEMD simulations of the VER of combinations of four different CO isotopologues, in both amorphous and crystalline clusters. Using trajectory ensembles we have determined average VER lifetimes in the order of nanoseconds from these simulations.

Originally motivated by the frequency-gap law, we have developed a novel analysis technique which allows to analyze the frequency-gap dependence $\Delta\nu$ of the decay time constants τ. An offset between decay time constants at positive and negative frequency-gaps was observed, where the VER rate was faster when the excited frequency was lower than the accepting frequency. These negative frequency-gaps are

only possible when the excited molecule is a different isotopes from the cluster, hence, we attribute this offset to a difference in anharmonic coupling between molecules of the same isotope and those of different isotopes. Crystalline clusters exhibit a different frequency-gap dependence than that of the amorphous clusters, where the VER was most efficient near $|\Delta\nu| = 50$ cm^{-1}.

A detailed analysis of the energy redistribution has revealed that vibrational energy dissipated into the cluster predominantly excites vibrational stretch modes of the surrounding molecules. This is not surprising when comparing to collisions of pairs of vibrationally excited CO molecules in gas phase: Chen *et al.*[29] found a lack of energy conversion between vibrational and rotational or translational energy. They attributed the lack of energy conversion to the energy-gap law, owing to the fact that vibrational quanta are much higher in energy than their rotational counterparts or the continuum provided by translational motion. The fact that rotational and translational modes form the low-frequency parts of the VDOS of the different forms of solid carbon monoxide studied here does not change the validity of this argument. Experiments for a monolayer of CO adsorbed on an NaCl(100) surface convey the same trend. Chang and Ewing[49] measured the rate of vibrationally induced desorption and found that is a slow process for this system due to inefficient energy transfer from vibrational to rotational and translation degrees of freedom.

Although the energy transfer occurs continuously in our classical simulations, further analysis of our trajectory ensembles elucidates very interesting analogies to the quantum mechanical description of V–V energy transfer for CO adsorbed on an NaCl(100) established by Corcelli and Tully[19]. While their model assumes parallel CO molecules that couple only through dipole-dipole interactions only, our cluster studies include more variation in the angular distribution (amorphous clusters in particular), and the interactions between CO molecules are not limited to dipole-dipole interactions. Apart from that, our novel analysis technique has allowed us to identify a qualitative change of the $\tau(\Delta\nu)$ relation when $\Delta\nu$ reaches the tail of the low-frequency VDOS – analogous to what the quantum mechanical theory predicts when switching from one-phonon to two phonon-assisted non-resonant V–V energy transfer. From the time evolution of the vibrational energy alone it is not easily noticed that this occurs, thus highlighting the usefulness of our novel technique. Furthermore, when the frequency-gap was essentially zero, we have observed a classical manifestation of the resonant V–V energy transfer mechanism described by Corcelli and Tully[19]. We found this mechanism to be independent of the cluster structure, indicating no strict dependence on orientation or LVM–LVM coupling. For the crystalline clusters, the

$\tau(\Delta\nu)$ analysis suggests that the VDOS influences the non-resonant V–V transfer in a different way than for the amorphous clusters, which requires more work to enable better understanding in the future.

Both non-resonant and resonant V–V energy transfer together with the absence of pronounced multi-phonon-assisted direct dissipation to low-frequency modes are the crucial ingredients for the vibrational energy pooling that has been observed for CO adsorbed on an NaCl(100). Considering that all of these ingredients seem to be captured by our classical simulations, future work with our computational setup could help to better understand if and if so how vibrational energy pooling could also occur in solid CO structures.

6.8 Data Availability Statement

All of the Julia code used for the simulations is publicly available on GitHub at https://github.com/Cavenfish/JMD. An HDF5 compliant dataset (Julia Data Format ".jld2") of all ensemble averages reported within the manuscript can be found on Zenodo at https://zenodo.org/records/14237514.

6.A Appendix

6.A.1 Size Convergence Tests

Since we do not employ periodic boundary conditions, we verified that the cluster size was large enough to capture all long-range interaction influencing the VER. Figure 6.A.12 shows the ensemble average energy decay for three different cluster sizes (100, 250 and 500 molecules), along with the cluster temperature below it.

There is very little difference between the three sizes, in agreement with VER theory which predicts a large radial decay for the vibrational energy transfer efficiency. Although there is little change in the VER lifetimes, the cluster temperature gain is largely affected by the size. Despite the temperature reported increasing due to excitation, the energy remains nearly entirely in vibrational energy which does not result in evaporation of the cluster. We opted to use clusters of 250 molecules since it provided an ideal compromise between temperature stability and computational efficiency.

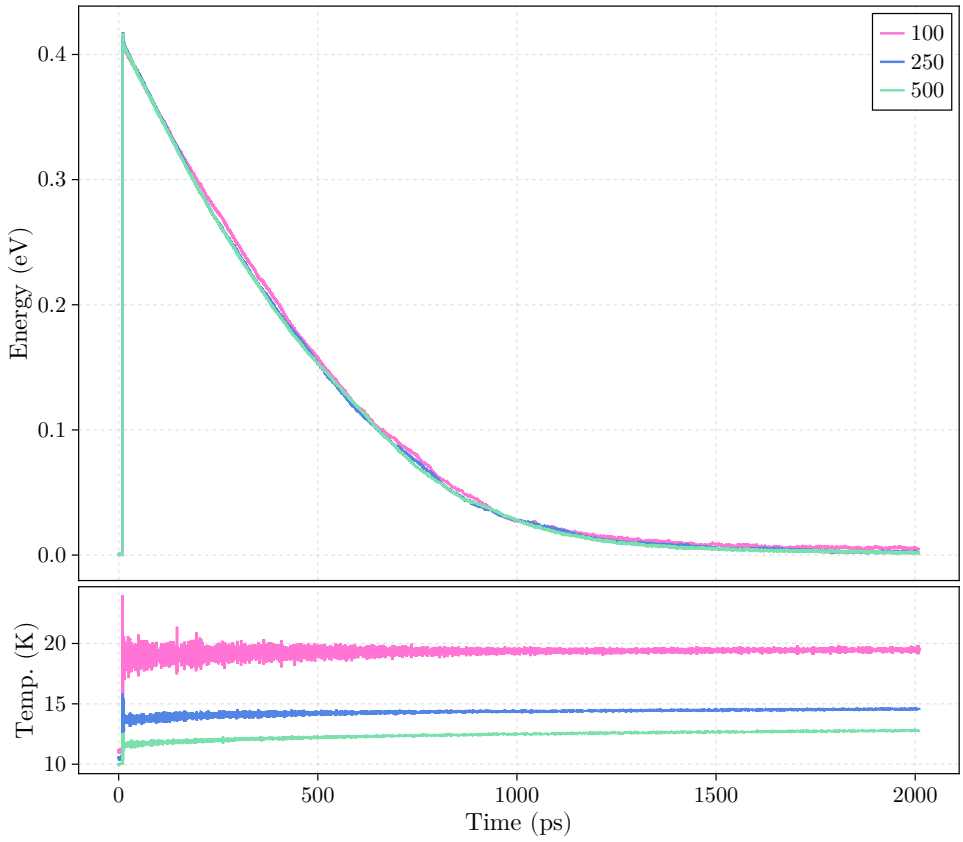

Figure 6.A.12: Upper panel: ensemble average of the vibrational energy of an excited CO molecule within an amorphous CO cluster. Lower panel: the cluster temperature during VER simulation. In both cases the 10 ps equilibration NVE simulation is included to illustrate the gain in temperature during excitation.

6.A.2 Geometric and Vibrational Properties for the PIP–NN Potential

Figure 6.A.13 compares the radial distribution (top left), angular distribution (top right) and the number of participating molecules per vibrational mode (bottom) of crystalline and amorphous CO using the PIP–NN potential.

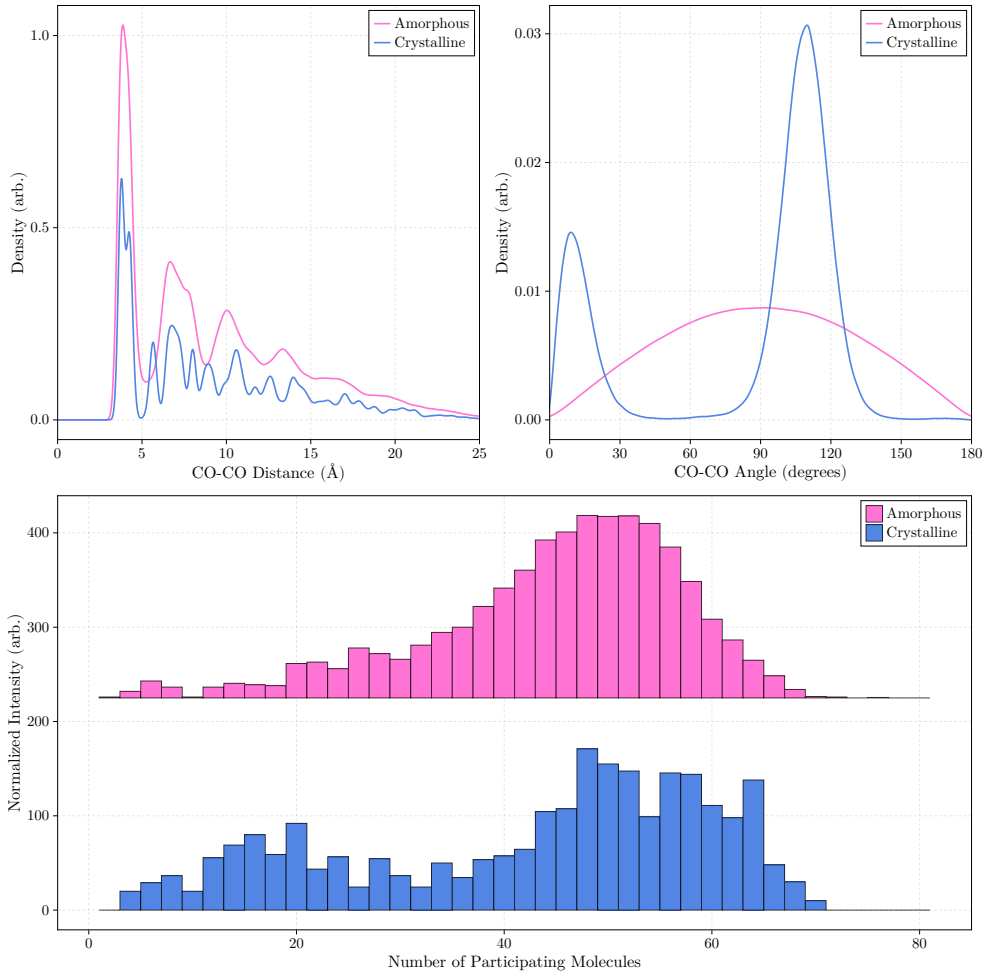

Figure 6.A.13: Same as Figure 1 in the main article but using the PIP–NN potential instead of the site–site potential.

6.A.3 Decomposition of Phonon DOS

Figure 6.A.14 shows the decomposition of the phonon DOS into surface and bulk contributions using the site–site potential.

Figure 6.A.15 shows the decomposition of the phonon DOS into surface and bulk contributions using the PIP–NN potential.

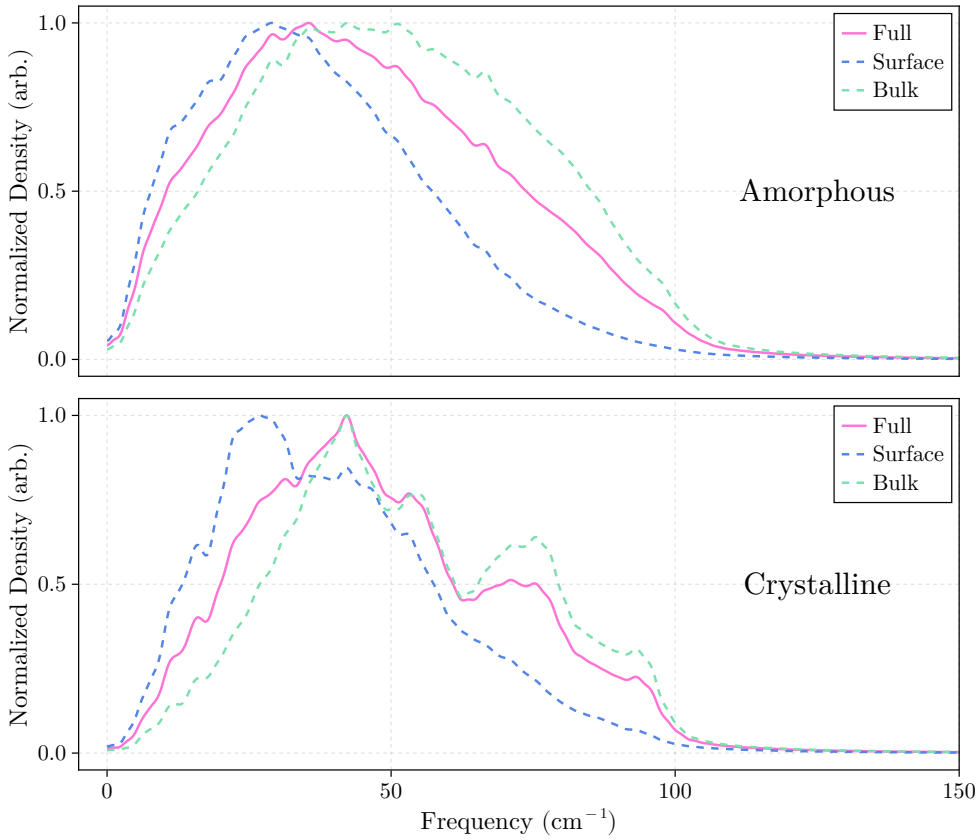

Figure 6.A.14: Decomposition of the phonon DOS shown in the upper panel of Figure 2 in the main article (using the site–site potential).

6.A.4 Trajectory Ensemble for Crystalline Clusters

Figure 6.A.16 shows the total energy of the excited molecule versus time (purple lines) for all simulaitons, and the average (gold) using the site–site potential for crystalline clusters.

6.A.5 Decomposition of Bi-Exponential Fits for Non-Resonant Energy Transfer

Figure 6.A.17 show the decomposition of the bi-exponential fit to the data shown in the top left panel of Figure 10.

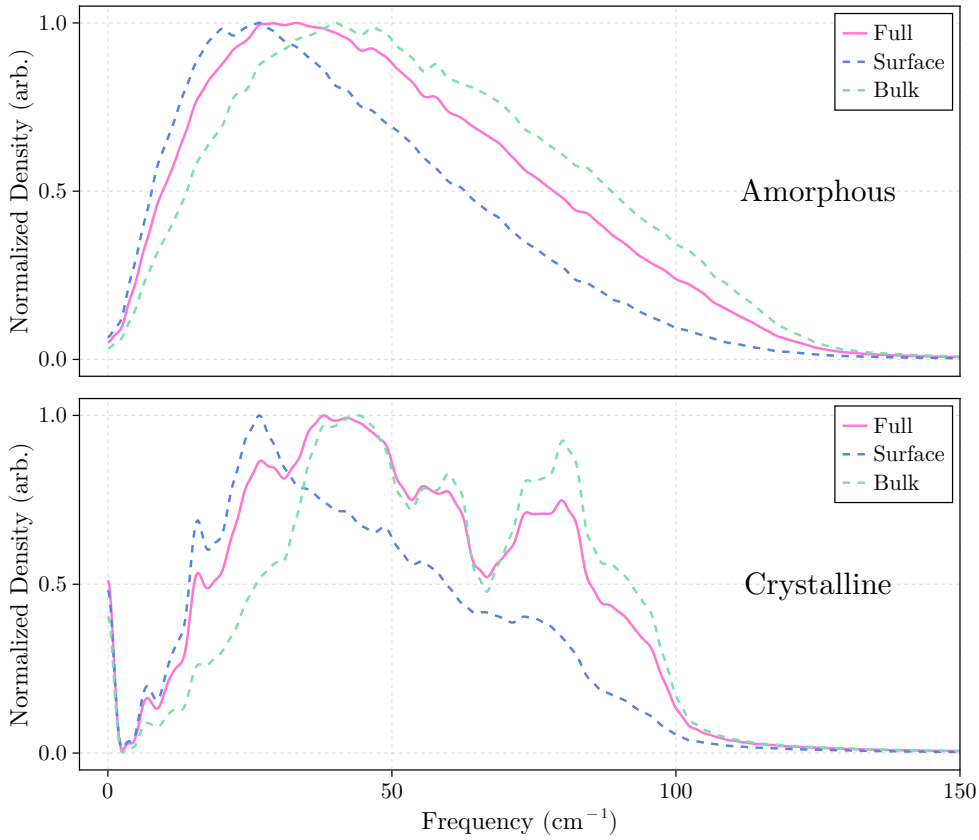

Figure 6.A.15: Decomposition of the phonon DOS shown in the lower panel of Figure 2 in the main article (using the PIP–NN potential).

Figure 6.A.18 show the decomposition of the bi-exponential fit to the data shown in the top right panel of Figure 10.

Figure 6.A.19 show the decomposition of the bi-exponential fit to the data shown in the bottom left panel of Figure 10.

Figure 6.A.20 show the decomposition of the bi-exponential fit to the data shown in the bottom right panel of Figure 10.

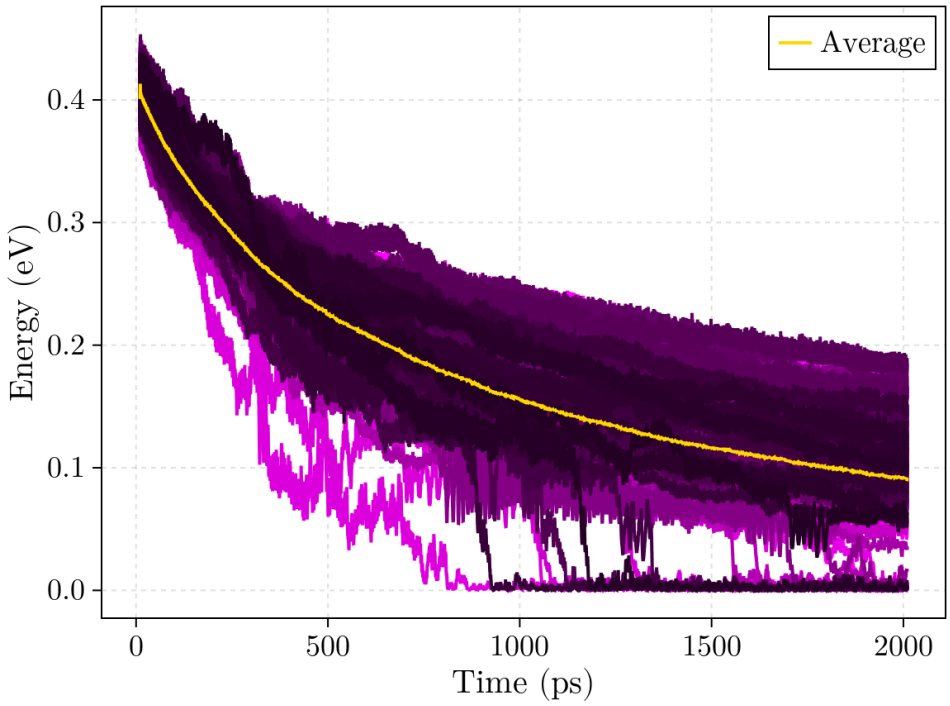

Figure 6.A.16: Same as Figure 3 in in the main article but for crystalline clusters.

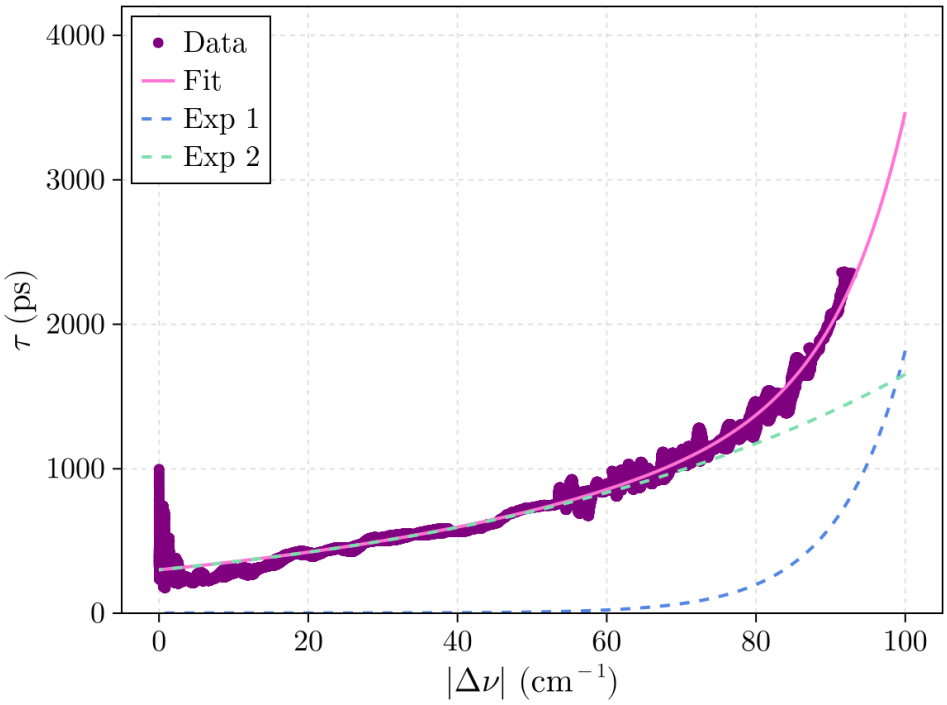

Figure 6.A.17: Decomposition of the bi-exponential fit to the τ data shown in the top left panel of Figure 10. Note that $|\Delta\nu|$ is plotted here and in the subsequent figures to enable a better comparison of the exponential fits.

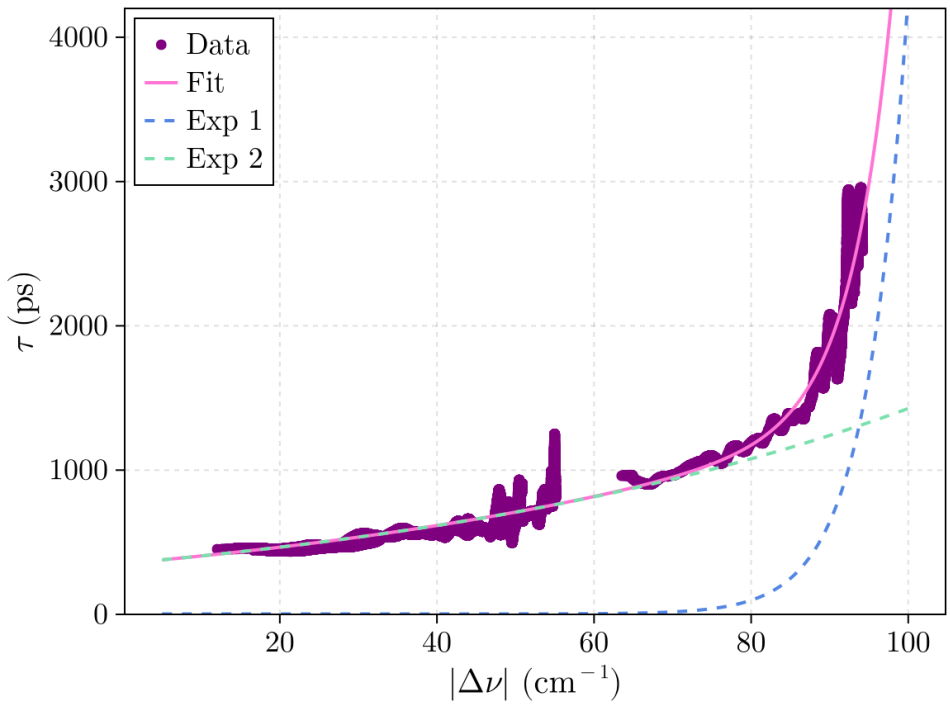

Figure 6.A.18: Same as Figure 6.A.17 but for the top right panel of Figure 10.

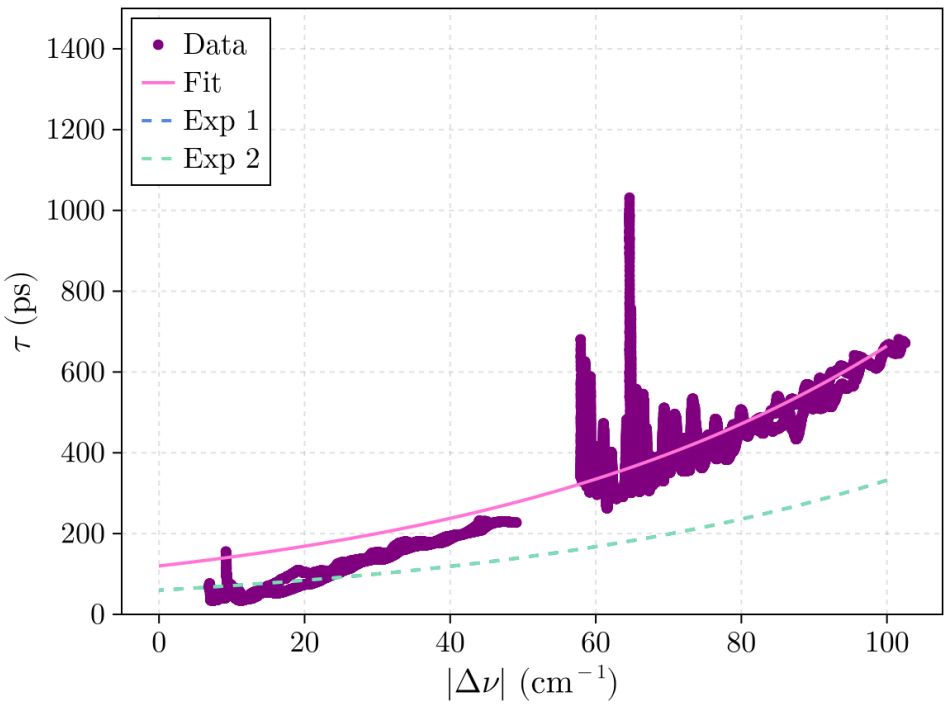

Figure 6.A.19: Same as Figure 6.A.17 but for the bottom left panel of Figure 10.

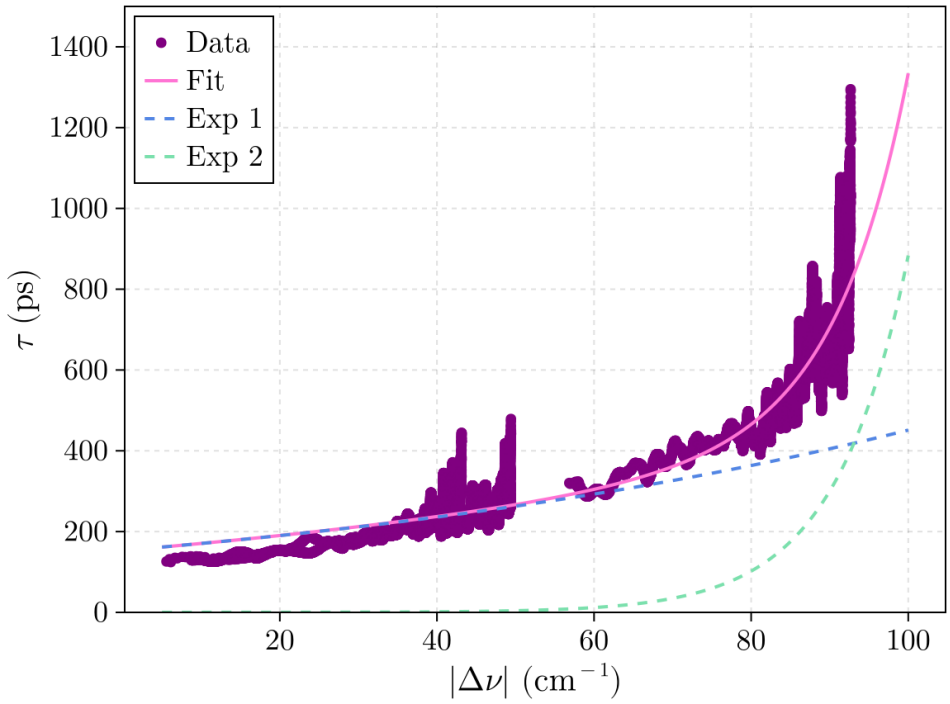

Figure 6.A.20: Same as Figure 6.A.17 but for the bottom right panel of Figure 10.

6.B Bibliography

[1] JC Owrutsky, D Raftery, and RM Hochstrasser. Vibrational relaxation dynamics in solutions. *Annual Review of Physical Chemistry*, 45(1):519–555, 1994.

[2] David R Glowacki, CH Liang, Stephen P Marsden, Jeremy N Harvey, and Michael J Pilling. Alkene hydroboration: hot intermediates that react while they are cooling. *Journal of the American Chemical Society*, 132(39):13621–13623, 2010.

[3] Barry K Carpenter, Jeremy N Harvey, and Andrew J Orr-Ewing. The study of reactive intermediates in condensed phases. *Journal of the American Chemical Society*, 138(14):4695–4705, 2016.

[4] Hiroshi Fujisaki and John E Straub. Vibrational energy relaxation in proteins. *Proceedings of the National Academy of Sciences*, 102(19):6726–6731, 2005.

[5] David M Leitner. Energy flow in proteins. *Annual Review of Physical Chemistry*, 59(1):233–259, 2008.

[6] Martin Gruebele and Peter Guy Wolynes. Vibrational energy flow and chemical reactions. *Accounts of Chemical Research*, 37(4):261–267, 2004.

[7] Qizhen Hong, Loriano Storchi, Quanhua Sun, Massimiliano Bartolomei, Fernando Pirani, and Cecilia Coletti. Improved quantum–classical treatment of n2–n2 inelastic collisions: Effect of the potentials and complete rate coefficient data sets. *Journal of Chemical Theory and Computation*, 19(23):8557–8571, 2023.

[8] Qizhen Hong, Loriano Storchi, Cecilia Coletti, Jia Li, Quanhua Sun, and Jun Li. Quantum-classical rate coefficient datasets of vibrational energy transfer in carbon monoxide based on highly accurate potential energy surface. *The Journal of Chemical Physics*, 160(8), 2024.

[9] Zhen Zhang, Lukasz Piatkowski, Huib J Bakker, and Mischa Bonn. Ultrafast vibrational energy transfer at the water/air interface revealed by two-dimensional surface vibrational spectroscopy. *Nature Chemistry*, 3(11):888–893, 2011.

[10] Prerna Sudera, Jenée D Cyran, Malte Deiseroth, Ellen HG Backus, and Mischa Bonn. Interfacial vibrational dynamics of ice ih and liquid water. *Journal of the American Chemical Society*, 142(28):12005–12009, 2020.

[11] Robert Englman and Joshua Jortner. The energy gap law for radiationless transitions in large molecules. *Molecular Physics*, 18(2):145–164, 1970.

[12] Abraham Nitzan, Shaul Mukamel, and Joshua Jortner. Energy gap law for vibrational relaxation of a molecule in a dense medium. *The Journal of Chemical Physics*, 63(1):200–207, 1975.

[13] Baozhou Sun, GA Shi, SVS Nageswara Rao, Michael Stavola, NH Tolk, SK Dixit, LC Feldman, and G Lüpke. Vibrational lifetimes and frequency-gap law of hydrogen bending modes in semiconductors. *Physical Review Letters*, 96(3):035501, 2006.

[14] Alexander Kandratsenka, Jörg Schroeder, Dirk Schwarzer, and Vyacheslav S Vikhrenko. Nonequilibrium molecular dynamics simulations of vibrational energy relaxation of hod in D_2O. *The Journal of Chemical Physics*, 130(17), 2009.

[15] G Lüpke, X Zhang, Baozhou Sun, A Fraser, NH Tolk, and LC Feldman. Structure-dependent vibrational lifetimes of hydrogen in silicon. *Physical Review Letters*, 88(13):135501, 2002.

[16] D West and SK Estreicher. Isotope dependence of the vibrational lifetimes of light impurities in si from first principles. *Physical Review B*, 75(7):075206, 2007.

[17] KK Kohli, Gordon Davies, NQ Vinh, D West, SK Estreicher, I Izeddin, and KM Itoh. Isotope dependence of the lifetime of the 1136-cm-1 vibration of oxygen in silicon. *Physical Review Letters*, 96(22):225503, 2006.

[18] Huan-Cheng Chang and George E Ewing. Infrared fluorescence from a monolayer of co on nacl (100). *Physical Review Letters*, 65(17):2125, 1990.

[19] SA Corcelli and JC Tully. Vibrational energy pooling in co on nacl (100): Methods. *The Journal of Chemical Physics*, 116(18):8079–8092, 2002.

[20] Li Chen, Jascha A Lau, Dirk Schwarzer, Jörg Meyer, Varun B Verma, and Alec M Wodtke. The sommerfeld ground-wave limit for a molecule adsorbed at a surface. *Science*, 363(6423):158–161, 2019.

[21] SA Corcelli and JC Tully. Vibrational energy pooling in co on nacl (100): Simulation and isotope effects. *The Journal of Physical Chemistry A*, 106(45):10849–10860, 2002.

[22] Jeff Bezanson, Alan Edelman, Stefan Karpinski, and Viral B Shah. Julia: A fresh approach to numerical computing. *SIAM Review*, 59(1):65–98, 2017.

[23] P Mogensen and A Riseth. Optim: A mathematical optimization package for julia. *Journal of Open Source Software*, 3(24):615, 2018.

[24] Christopher Rackauckas and Qing Nie. Differentialequations.jl–a performant and feature-rich ecosystem for solving differential equations in julia. *Journal of Open Research Software*, 5(1):151, 2017.

[25] Simon Danisch and Julius Krumbiegel. Makie.jl: Flexible high-performance data visualization for julia. *Journal of Open Source Software*, 6(65):3349, 2021.

[26] Matteo Frigo and Steven G Johnson. Fftw: An adaptive software architecture for the fft. In *Proceedings of the 1998 IEEE International Conference on Acoustics, Speech and Signal Processing, ICASSP'98 (Cat. No. 98CH36181)*, volume 3, pages 1381–1384. IEEE, 1998.

[27] C Bradford Barber, David P Dobkin, and Hannu Huhdanpaa. The quickhull algorithm for convex hulls. *ACM Transactions on Mathematical Software (TOMS)*, 22(4):469–483, 1996.

[28] Marc C van Hemert, Junko Takahashi, and Ewine F van Dishoeck. Molecular dynamics study of the photodesorption of co ice. *The Journal of Physical Chemistry A*, 119(24):6354–6369, 2015.

[29] Jun Chen, Jun Li, Joel M Bowman, and Hua Guo. Energy transfer between vibrationally excited carbon monoxide based on a highly accurate six-dimensional potential energy surface. *The Journal of Chemical Physics*, 153(5):054310, 2020.

[30] Brian C. Ferrari, Germán Molpeceres, Johannes Kästner, Yuri Aikawa, Marc van Hemert, Jörg Meyer, and Thanja Lamberts. Floating in space: How to treat the weak interaction between co molecules in interstellar ices. *ACS Earth and Space Chemistry*, 7(7):1423–1432, 2023. doi: 10.1021/acsearthspacechem.3c00086.

[31] Samuel Del Fré, Alejandro Rivero Santamaría, Denis Duflot, Romain Basalgète, Géraldine Féraud, Mathieu Bertin, Jean-Hugues Fillion, and Maurice Monnerville. Mechanism of ultraviolet-induced co desorption from co ice: Role of vibrational relaxation highlighted. *Physical Review Letters*, 131(23):238001, 2023.

[32] Giovanni Bussi, Davide Donadio, and Michele Parrinello. Canonical sampling through velocity rescaling. *The Journal of Chemical Physics*, 126(1):014101, 2007.

[33] Loup Verlet. Computer “experiments" on classical fluids. i. thermodynamical properties of lennard-jones molecules. *Physical Review*, 159(1):98, 1967.

[34] William C Swope, Hans C Andersen, Peter H Berens, and Kent R Wilson. A computer simulation method for the calculation of equilibrium constants for the formation of physical clusters of molecules: Application to small water clusters. *The Journal of Chemical Physics*, 76(1):637–649, 1982.

[35] Barbara Okray Hall and Hubert M James. Lattice dynamics of α carbon monoxide. *Physical Review B*, 13(8):3590, 1976.

[36] Yanqiang Han, Jinyun Liu, and Jinjin Li. Ab initio investigation of solid carbon monoxide phase diagram at low temperature. *Materials Today Communications*, 28:102571, 2021.

[37] MC Van Hemert. Potential energy surface for the study of inelastic collisions between nonrigid co and h_2. *The Journal of Chemical Physics*, 78(5):2345–2354, 1983.

[38] Franco A Gianturco. *The transfer of molecular energies by collision: recent quantum treatments*, volume 11. Springer Science & Business Media, 2012.

[39] Peter Kahlig. Some aspects of julius von hann's contribution to modern climatology. *Interactions Between Global Climate Subsystems: The Legacy of Hann*, 75: 1–7, 1993.

[40] G Guelachvili. Absolute wavenumbers and molecular constants of the fundamental bands of $^{12}c^{16}o$, $^{12}c^{17}o$, $^{12}c^{18}o$, $^{13}c^{16}o$, $^{13}c^{17}o$, $^{13}c^{18}o$ and of the 2-1 bands of $^{12}c^{16}o$ and $^{13}c^{16}o$, around 5μm, by fourier spectroscopy under vacuum. *Journal of Molecular Spectroscopy*, 75(2):251–269, 1979.

[41] LJ Karssemeijer, S Ioppolo, MC Van Hemert, A Van Der Avoird, MA Allodi, GA Blake, and HM Cuppen. Dynamics of co in amorphous water-ice environments. *The Astrophysical Journal*, 781(1):16, 2013.

[42] BM Giuliano, AA Gavdush, B Müller, KI Zaytsev, T Grassi, AV Ivlev, Maria Elisabetta Palumbo, GA Baratta, C Scire, GA Komandin, *et al.* Broadband spectroscopy of astrophysical ice analogues-i. direct measurement of the complex re-

fractive index of co ice using terahertz time-domain spectroscopy. *Astronomy & Astrophysics*, 629:A112, 2019.

[43] Wei Lee and Thomas J Wdowiak. Laboratory fourier-transform terahertz spectroscopy for molecular ices of astrophysical interest: Solid co as an example. *Japanese Journal of Applied Physics*, 43(10R):7303, 2004.

[44] NB Slater. Classical motion under a morse potential. *Nature*, 180(4598):1352–1353, 1957.

[45] Robert F Goldstein and William Bialek. Vibronically coupled two-level systems: Radiationless transitions in the slow regime. *Physical Review B*, 27(12):7431, 1983.

[46] Xiaoyong Zhang, Saulo A Vazquez, and Jeremy N Harvey. Vibrational energy relaxation of deuterium fluoride in d-dichloromethane: insights from different potentials. *Journal of Chemical Theory and Computation*, 17(3):1277–1289, 2021.

[47] Abraham Savitzky and Marcel JE Golay. Smoothing and differentiation of data by simplified least squares procedures. *Analytical Chemistry*, 36(8):1627–1639, 1964.

[48] Jascha A Lau, Li Chen, Arnab Choudhury, Dirk Schwarzer, Varun B Verma, and Alec M Wodtke. Transporting and concentrating vibrational energy to promote isomerization. *Nature*, 589(7842):391–395, 2021.

[49] Huan-Cheng Chang and George E Ewing. The quantum efficiency of vibrationally induced desorption for a monolayer of co on nacl (100). *Chemical Physics*, 139 (1):55–65, 1989.

.0 Bibliography

Summary

Microscopic interactions are characterized through atomistic simulations using either first principals quantum chemistry techniques or empirical interatomic potentials. Understanding these microscopic interactions helps us understand large scale phenomena such as catalysis, crystal growth, and phase transitions. In particular, the processes of adsorption and vibrational energy relaxation (VER) are intrinsically related to catalysis. Adsorption is the first step in a catalytic process, and VER is often the rate limiting step in a catalytic cycle. Thus, understanding the microscopic interactions that govern adsorption and VER is crucial to understanding catalysis.

Adsorption

Adsorption is the process by which molecules or atoms adhere to a surface, over time forming a thin film or layer. Experiments offer the most realistic value for the binding energy, however, they can only measure the statistical average binding energy. Similarly, experimental measurements of adsorption are often unable to provide realiable data on certain unique cases. This is due to the fact that measurements of binding energies tend to rely on the desorption of the adsorbed molecules at a certain termperature. Hence, the unique case of a molecule adsorbing on a solid of the same species (*ie.* H_2O on H_2O) with a binding energy larger than the cohesive energy is nearly impossible to measure. Simulations can fill in the gaps by providing a complete distribution of the binding energies, including the unique case mentioned above.

Vibrational Energy Relaxation

Vibrational energy relaxation (VER) is the process by which a vibrationally excited molecule returns to its ground state by transferring its excess energy to its surroundings. This process is crucial in many chemical and physical phenomena, including energy transfer in biological systems, catalysis, and in the selectivity of chemical reactions. VER can occur through various mechanisms, including vibrational-vibrational (V-V) energy transfer, vibrational-translational (V-T) energy transfer, vibrational-rotational (V-R) energy transfer, and vibrational-electronic (V-E) energy transfer. The efficiency of VER depends on several factors, including the nature of the molecule, the surrounding environment, and the energy gap between the excited and ground states.

The most common way to study VER in simulations is to use non-equilibrium molecular dynamics (NEMD) simulations. In these simulations the molecule of interest is excited to a higher vibrational state, and the subsequent relaxation process is monitored over time. A general trend for VER lifetimes is that they decrease with increasing temperature, a result of an increased coupling between the excited molecule and the surrounding bath modes. This increased coupling is due to the fact that higher temperatures lead to higher occupancy of vibrational modes within the bath, effectively reducing the energy gap.

This Thesis

Chapter 3: A Julia package for atomic simulations, *YetAnotherSimulationSuite.jl* (YASS), that was developed during the PhD is described. Benchmarks comparing the performance of this package to the most popular Python-based package (ASE) are shown. The Julia package is up to 6 times faster, with initial compilation time overhead making it slower for very short calculations. As the calculation times grows the speedup offered by the Julia package also grows.

Chapter 4: The binding energy of H_2O on the ice Ih (0001) surface is studied. The physiochemical properties governing the adorption are broken down and carfeully scrutinized. We find an abundance of binding sites with binding energy larger than the cohesive energy of the crystal. This has significant implications for crystal growth, where the standard model is no longer applicable. Furthermore, we explore how the local environment on the surface influences the binding energy. From this we produce a descriptor for the local surface environment that can be used to predict the binding energy at sites on the surface.

Chapter 5: The binding energy of CO on amorphous and crystalline CO is studied. The most important contributions to the binding energy are investigated, and the importance of long-range interactions is analyzed. Furthermore, a benchmark of DFT functionals is carried out, where the best performing functional is presented. We find that CO binding is dominated by dispersion, with negligible contributions from many-body effects in solid CO. The distribution of binding energies for CO on amorphous CO is broad (200 – 1600 K), and depends on the size of the cluster. The dependence on the size of the cluster reveals that long-range interactions are relevant to the adsorption of CO on amorphous CO. Zero point energy corrections within the harmonic approximation lowers the average binding energy by 20-30%. CO binding on crystalline α-CO has a narrower distribution (650 – 800 K), and is orientation

dependent. The median value of the binding energy distribution for amorphous and crystalline CO are very similar, corroborating previous studies which assumed them to be equal. Lastly, a benchmark revealed that the ωB97M-V functional performs the best when treating the CO–CO dimer interaction energy.

Chapter 6: Utilizing NEMD simulations the VER process for CO in amorphous and crystalline CO is studied. A novel analysis techinique for studying the frequency-gap dependence of the decay time constant was developed. Anharmonic coupling between an excited CO molecule and a different CO isotopologue results in vibrational energy relaxation (VER) that is faster when the excited molecule has a lower frequency than the accepting molecule. Whereas, in crystalline clusters the frequency-gap dependence exhibited no significant trends other than being most efficient at gaps of 50 cm^{-1}. Vibrationally excited CO molecules in solid CO redistribute their energy primarily through vibrational–vibrational energy transfer. This is due to the large frequency-gap between the vibrational mode of CO and the rotational and phonon modes of CO clusters. The CO VER exhibits a two-channel decay dependence on the frequency-gap, analogous to the quantum mechanical prediction of CO VER switching from one-phonon to two-phonon assisted decay. The necessary physiochemical properties for VER are well captured by the classical pair potentials used to simulate the VER of CO.

Outlook

The collection of works within this thesis not only presents novel results, but also opportunities for furture works to continue advancing our understanding of the topics studied. In the works published much earlier, some of these new opportunities have already been taken and subsequent papers have been published by others. In particular, the results found in Chapter 5 & Chapter 6 have been used to explain experimental results that offer some understanding of observed gas-phase CO abundances in the ISM. Furthermore, *YetAnotherSimulationSuite.jl* can continue to grow and mature as an open-source package. As it attracts more user and developer attention it can grow to be of significant importance to the computational chemistry community.

Samenvatting

Van adsorptie tot dissipatie: Inzichten uit computersimulaties van vast H_2O en CO

In dit proefschrift worden de effecten van wisselwerkingen op microscopische schaal kenbaar gemaakt in simulaties. De simulaties maken gebruik van potentialen die gevonden zijn met behulp van kwantumchemie op basis van "first principles" of van empirische potentialen.

Inzicht in deze microscopische wisselwerkingen helpt bij het verklaren van macroscopische verschijnselen zoals katalyse, kristalgroei en faseovergangen. Met name adsorptie en vibratierelaxatie van energie (VER) staan in direct verband met katalyse. Adsorptie is vaak de initiële stap in een katalytisch proces, terwijl VER veelal de snelheidsbepalende stap is in een katalytische cyclus. Daarom is begrip van de microscopische mechanismen die adsorptie en VER sturen essentieel voor het begrip van katalytische processen.

Adsorptie

Adsorptie is het proces waarbij moleculen of atomen zich aan een oppervlak hechten en in de loop van de tijd een dunne film of laag vormen. Experimenten leveren doorgaans de meest realistische waarden voor bindingsenergieën, maar meten meestal alleen het statistische gemiddelde. Daardoor kunnen experimentele technieken moeite hebben met het identificeren van bijzondere gevallen. Metingen van bindingsenergieën zijn vaak gebaseerd op desorptie bij een bepaalde temperatuur. Hierdoor zijn gevallen zoals H_2O dat op H_2O adsorbeert met een bindingsenergie groter dan de cohesie energie van de vaste stof bijna niet experimenteel te karakteriseren. Simulaties kunnen deze lacunes opvullen door volledige verdelingen van bindingsenergieën te leveren, inclusief zeldzame of lokaal maximaal bindende configuraties.

Vibratierelaxatie van Energie (VER)

Vibratierelaxatie (VER) is het proces waarbij een vibrationeel aangeslagen molecuul terugkeert naar de grondtoestand door overtollige energie over te dragen aan de omgev-

ing. Dit proces is belangrijk in vele chemische en fysische contexten, zoals energieoverdracht in biologische systemen, katalyse en de selectiviteit van reacties. VER kan verlopen via verschillende mechanismen: vibratie–vibratie (V–V), vibratie–translatie (V–T), vibratie–rotatie (V–R) en vibratie–elektronische (V–E) energieoverdracht. De efficiëntie van VER hangt af van de eigenschappen van het molecuul, de omgeving van het molecuul en het energieverschil tussen aangeslagen toestand en grondtoestand va hetm molecuul.

In simulaties wordt vibratie energie relaxatie veelal bestudeerd met niet-evenwichts moleculaire dynamica (NEMD). Hierbij wordt het onderzochte molecuul in een hogere vibratietoestand gebracht en het relaxatieproces in de tijd gevolgd. Algemene trends tonen dat VER levensduren meestal afnemen met toenemende temperatuur. Een hogere temperatuur verhoogt de bezetting van de niveaus van de vibraties in het bad gevormd door de omringende moleculen en vergroot daardoor de koppeling tussen het aangeslagen moledcuul en zijn omgeving. Hierdoor wordt het effectieve energie verschil kleiner.

Dit proefschrift

Hoofdstuk 3: Een in Julia ontwikkeld pakket voor atomistische simulaties, *YetAnotherSimulationSuite.jl* (YASS), wordt beschreven. Benchmarkvergelijkingen met het veelgebruikte Python-pakket ASE laten zien dat het Julia-pakket in veel gevallen tot ongeveer zes keer sneller is. De initiële overhead door compilatie maakt korte berekeningen trager, naarmate de rekentijd toeneemt neemt de relatieve snelheidswinst toe.

Hoofdstuk 4: De bindingsenergie van een water (H_2O) molecuul aan het oppervlak van ijs met de Ih(0001) structuur wordt onderzocht. De verschillende fysischchemische bijdragen aan de adsorptie energie worden opgesplitst en zorgvuldig geanalyseerd. We vinden een overvloed aan bindingsplaatsen met een bindingsenergie groter dan de cohesie energie van het kristal. Dit heeft belangrijke consequenties voor kristalgroeimodellen: het standaardmodel is in dergelijke gevallen niet meer toepasbaar. Daarnaast onderzoeken we hoe de lokale omgeving in het oppervlak de bindingsenergie beïnvloedt en ontwikkelen we een grootheid die de lokale omgeving karakteriseert en gebruikt kan worden om bindingsenergieën te voorspellen.

Hoofdstuk 5: De bindingsenergie van CO op amorf en kristallijn CO wordt bestudeerd. De belangrijkste bijdragen aan de bindingsenergie worden geïdentificeerd en het belang van interacties met lange dracht wordt geanalyseerd. Verder wordt een

benchmark van DFT-functionalen uitgevoerd, waarbij het best presterende functional wordt gepresenteerd. We vinden dat de CO-binding hoofdzakelijk door dispersie wordt bepaald, met verwaarloosbare bijdragen van veeldeeltjes-effecten in vast CO.

De verdeling van bindingsenergieën voor CO op amorf CO is breed (200–1600 K) en hangt af van de grootte van het bestudeerde cluster, wat erop wijst dat de interacties met lange dracht relevant zijn. Correcties voor nulpuntsenergie binnen de harmonische benadering verlagen de gemiddelde bindingsenergie met ongeveer 20–30%. De bindings energie van CO op kristallijn CO in de α-phase heeft een smallere verdeling (circa 650–800 K) en is oriëntatie-afhankelijk. De gemiddelde waarden voor amorf en kristallijn CO zijn vergelijkbaar, wat eerdere aannames ondersteunt. Ten slotte blijkt de ωB97M-V functionaal het beste te presteren voor de CO–CO dimeer wisselwerking.

Hoofdstuk 6: Met NEMD-simulaties wordt het VER-proces voor CO in amorf en kristallijn CO onderzocht. Er is een nieuwe analysetechniek geïntroduceerd om te bestuderen hoe de tijdsconstante voor het proces van verval van de vibratieenergie afhangt van het frequentie verschil. De resultaten tonen aan dat anharmonische koppeling tussen een aangeslagen CO-molecuul en een ander CO molecuul met een andere isotoop samenstelling leidt tot snellere VER wanneer het aangeslagen molecuul een lagere frequentie heeft dan het accepterende molecuul. In kristallijne clusters vertoont de afhankelijkheid van het frequentieverschil geen sterke trends, behalve een maximale efficiëntie bij een verschil rond 50 cm^{-1}. Vibratieaangeslagen CO-moleculen in vast CO herverdelen hun energie voornamelijk via vibratie–vibratie overdracht. Dit is het gevolg van het grote verschil in frequenties van de CO-vibraties en die van de rotatie en roostertrillingen van het cluster. De VER volgt een tweekanaals afhankelijkheid van het frequentie verschil. Dit is analoog aan de kwantummechanische verwachting dat VER overschakelt van een eén-foton mechanisme naar een mechanisme gebasserd op twee foton–overgangen. De gebruikte klassieke paarpotentialen beschrijven de benodigde fysisch-chemische eigenschappen voor VER adequaat.

Vooruitblik

De vier artikelen in dit proefschrift presenteren niet alleen nieuwe resultaten, maar ook kansen voor toekomstige studies om ons begrip van de bestudeerde onderwerpen verder te vergroten. In eerder gepubliceerde artikelen zijn sommige vandeze nieuwe mogelijkheden al benut en zijn er vervolgpublicaties door anderen verschenen.

In het bijzonder zijn de resultaten uit Hoofdstuk 5 en Hoofdstuk 6 gebruikt om-

experimentele resultaten te verklaren. Resulatateen die inzicht geven in waargenomen gasvormige CO-concentraties in de interstellaire ruimte. Verder kan *YetAnotherSimulationSuite.jl* blijven groeien en zich ontwikkelen als open-source pakket. Naarmate het meer gebruikers en ontwikkelaars aantrekt, kan het uitgroeien tot een belangrijk hulpmiddel voor de computationele chemie gemeenschap.

Publications

1. **Ferrari, B. C.**, Sallermann, M., Jónsson, E. O., Jónsson, H., & Meyer, J. (2026). Abundance of Exceptionally Strong Binding Sites for H_2O Adsorption on the Ice Ih(0001) Surface, *in prep.*

2. **Ferrari, B. C.**, "YetAnotherSimulationSuite.jl: An Atomic Simulation Suite in Julia." Journal of Open Source Software 10.116 (2025): 9480.

3. **Ferrari, B. C.**, van Hemert, M., Meyer, J., & Lamberts, T. (2024). Vibrational Energy Relaxation in Solid Carbon Monoxide. The Journal of Physical Chemistry C, 128(49), 21060-21072.

4. **Ferrari, B. C.**, Molpeceres, G., Kästner, J., Aikawa, Y., van Hemert, M., Meyer, J., & Lamberts, T. (2023). Floating in Space: How to Treat the Weak Interaction between CO Molecules in Interstellar Ices. ACS Earth and Space Chemistry, 7(7), 1423-1432.

5. **Ferrari, B. C.**, and Bennett, C. J. "A computational investigation of the equilibrium geometries, energetics, vibrational frequencies, infrared intensities and Raman activities of C2O y (y= 3, 4) species." Molecular Physics 119.6 (2021): e1837404.

6. **Ferrari, B. C.**, Slavicinska, K. and Bennett, C. J. "Role of suprathermal chemistry on the evolution of carbon oxides and organics within interstellar and cometary ices." Accounts of Chemical Research 54.5 (2021): 1067-1079.

7. Fortenberry, R. C., Peters, D., Bennett, C. J., **Ferrari, B. C.**, "Rovibrational Spectral Analysis of CO3 and C2O3: Potential Sources for O2 Observed in Comet 67P/Churyumov–Gerasimenko." The Astrophysical Journal Letters 886.1 (2019): L10.

8. **Ferrari, B. C.**, and Bennett, C. J. "A comparison of medium-sized basis sets for the prediction of geometries, vibrational frequencies, infrared intensities and raman activities for water." Journal of Physics: Conference Series. Vol. 1290. No. 1. IOP Publishing, 2019.

9. **Ferrari, B. C.**, "AutoGAMESS: A Python package for automation of GAMESS (US) Raman calculations." Journal of Open Source Software 4.41 (2019): 1612.

Curriculum vitae

I was born in Orlando, Florida to Brazilian immigrant parents on March 6th, 1996. My father grew up in a very poor family which made him drop out of elementary school to get a job to support his family. My mother on the other hand was fortunate enough to complete her schooling and go on to receive a college degree prior to my birth. Currently, my father has returned to school and finished middle school and my mother has received multiple graduate degrees. The dichotomy of my parents' education levels meant I grew up hearing two perspectives on school and what an education means to a person. My father advocated that the only purpose of an education was to get a better job, whereas my mother believed it was a way to become more open-minded, feel fulfilled, and a source of passion.

My pre-university education was mixed, having gone to school in both Brazil and the USA. I went to a public elementary school in Florida, then a private middle school in São Paulo, and finally back to a public high school in Florida. In high school I couldn't care less about studying, and at the time I had no ambitions that pushed me to care. Despite that, I knew I was going to attend university for a bachelor's degree, mostly because it made job prospects better. When it came time to decide on a major I picked physics because it was the class in high school that I found the easiest. My only reason for picking it was that it came naturally to me (so the courses would be easy for me), and I found it interesting enough. I was accepted into the University of Central Florida (UCF) for a physics bachelor's degree.

During my undergraduate degree I met Dr. Costas Efthimiou, a mathematical physicist at UCF. He initially took interest in me because I, at the time, was coaching children's soccer, and he wanted me to coach his son. At that time, I was also growing more passionate about physics and considering pursuing a physics graduate degree. At UCF, Costas was known for having recently mentored a bachelor's student that went on to receive multiple prestigious fellowships for a PhD position at Harvard. We initially agreed that I would coach his son in exchange for him mentoring me; however, he eventually decided that I needed to solely focus on physics. He outlined a plan for me to make myself an ideal candidate for a PhD, but he also emphasized that my "low math grades" at university would likely exclude me from any PhD programs. Although I was not a bad student, he viewed anything less than perfect in an American school to be bad compared to European schools (a topic up for debate). The most significant part of his plan was writing a research proposal for a society of physics students (SPS)

chapter research grant. This was a small grant for students to carry out independent research style projects. I was awarded $ 2,000 to build an experimental setup for performing the Cavendish experiment to measure the gravitational constant. Upon completion of this project, it was incorporated into the undergraduate UCF physics laboratory course for physics majors.

As an undergraduate student I joined a research group, another recommendation from Costas, headed by Dr. Christopher J. Bennett at UCF. At this point I had worked for a year as a machinist apprentice, so I was able to construct an ultrahigh vacuum (UHV) in Chris's laboratory, as well as design and machine a custom-made sample holder and various subsequent variants for the chamber. Alongside the laboratory work, I began running computational calculations of astrophysically relevant molecules. Upon completing my bachelor's degree, I accepted a PhD position at UCF to continue working under Chris. It was during this time that I met my wife, Katie Slavicinska, who a semester after me also accepted a PhD position in the Bennett lab.

At the time, the American science funding was orders of magnitude ahead of the world, and so it was common for PhD students to apply for grants. Chris advised me to apply for various NASA grants and fellowships. I managed to secure a $ 165,000 NASA fellowship and an additional $ 4,000 research grant. The NASA fellowship was a joint NASA Ames and UCF research project where I was supposed to spend summers at NASA Ames. Unfortunately, COVID prevented me from going to NASA Ames my first year, and shortly after that, I left UCF.

In search of better PhD prospects, my wife and I applied for two positions in the Leiden Laboratory for Astrophysics. Unfortunately, only one position was available, but it was made clear to us that another faculty member at Leiden University was looking for a PhD student. The other faculty member, Thanja Lamberts, worked in theoretical chemistry, meaning only I was qualified for the position.

At Leiden I worked under Thanja for the first few years, then transitioned to working under Jörg Meyer for the remaining time. April 20^{th}, 2023 I completed a course on scientific conduct at the Graduate School of Science. My PhD work has culminated in a handful of publications. However, what I'm truly proud to have produced during my PhD is my Julia package *YetAnotherSimulationSuite.jl*.

Acknowledgments

The first, and most important, person I'd like to thank is Katie Slavicinska. I truly would not have been able to complete this PhD without her support and encouragement. During the darkest and lowest points of my PhD, she managed to pull me out of the darkness and guide me back on course.

The next (obvious) important person to thank is my mother. She raised me to always believe in myself, just as she always did, which is likely why I felt a PhD was possible for me. Naturally, I also want to thank my brother and sister, Bruno & Julia, for all the love and great times we have had.

I would also like to thank the *Friends Family* (both the *Tios & Tias* and the *kids*). Despite them all being so far away and me rarely being active in the WhatsApp chats, they have all helped me finish the PhD. The words of encouragement that I received from the *Tios & Tias* before I left for the Netherlands have stayed with me throughout the process. The love from the *Friends Family* has always helped to keep my mental health balanced, which has been instrumental in this PhD. Lastly, knowing I will be gifted one of Victor DeMarco's arms once I complete the PhD has been a key motivator.

Naturally I owe many thanks to my promoter and supervisor, Jörg Meyer, for all the guidance and feedback he gave me on my research.

Along the way there have been many people who gave me useful guidance and feedback on my research, all of which I am thankful to have received. These people are Hannes Jonsson, Elvar Jonsson, Marc van Hemert, German Molpeceres, and Moritz Sallermann.

I want to specifically thank Julia & Fabio and Marina & Folkert for their friendships. Having such close friends was really meaningful and made the PhD a more enjoyable experience.

A special thanks goes to Jerry & Nienke, not only for their friendship but also for the numerous times they cat-sat Tina for us.

Finally, I want to thank the many people who made my PhD experience more enjoyable: Bibiana, Carlos, Carson, Dario, Emma, Floris, Franciele, Jessalyn, Joan, Logan, Lukas, Lukasz, Marten, Milan, Nashanty, Neven, Pavi, Robert, Tobias.

Data Availability

Chapter 5

All of the Python code used for the simulations is publicly available on GitHub at https://github.com/Cavenfish/CO_Project. XYZ files for all clusters used in this work can be found on Zenodo at https://zenodo.org/records/8068393.

Chapter 6

All of the Julia code used for the simulations is publicly available on GitHub at https://github.com/Cavenfish/YetAnotherSimulationSuite.jl. An HDF5 compliant dataset (Julia Data Format ".jld2") of all ensemble averages reported within the manuscript can be found on Zenodo at https://zenodo.org/records/14237514.